The Pennsylvania State University
The Graduate School
College of Engineering

MAGNETOELECTRIC AND OPTO-MECHANICAL MAGNETIC SENSING

A Dissertation in
Electrical Engineering
by
Eugene Freeman

Submitted in Partial Fulfillment
of the Requirements
for the Degree of

Doctor of Philosophy

December 2017

The dissertation of Eugene Freeman was reviewed and approved* by the following:

Srinivas Tadigadapa
Professor of Electrical Engineering and Biomedical Engineering
Dissertation Advisor, Chair of Committee

Steven J. Schiff
Brush Chair Professor of Engineering Science and Mechanics

Jerzy Ruzyllo
Distinguished Professor of Electrical Engineering

Susan Trolier-McKinstry
Steward S. Flaschen Professor of Materials Science and Engineering and Electrical Engineering

Kultegin Aydin
Professor of Electrical Engineering
Head of the Department of Electrical Engineering

*Signatures are on file in the Graduate School.

Abstract

Magnetic sensors are of ever increasing relevance to modern society. Magnetic sensors have found practical applications in smartphones, aerospace, automotive, industrial and biomagnetic sensing. Most applications are navigational owing the earth's relatively stable magnetic field, although rotational and speed sensors are found in automotive and industrial settings. Availability of low-cost and reliable magnetometer technologies have contributed their ubiquitous nature. However, the most sensitive magnetic fields emitted from the brain can only be detected by superconducting quantum interference devices (SQUIDs), which require cryogenic cooling to maintain a superconducting state and require magnetic shielding. An inexpensive room temperature magnetometer technology capable of magnetoencephalography (MEG) and other biomagnetic signals is an active area of research.

This dissertation provides three significant contributions to this problem. First, a detailed and comprehensive set of methods are explored and demonstrated in an effort to optimize the magnetoelectric magnetometer, a promising magnetometer technology that may replace SQUIDs in some applications. Second, a novel chip-scale whispering gallery mode magnetometer is proposed, modeled using a finite element simulator and experimentally demonstrated with a 6×10^{-8} T/$\sqrt{\text{Hz}}$ limit of detection (LOD) and the potential for much lower LOD is demonstrated. Third, a novel passively-powered micromachined quartz magnetoflexoelastic magnetometer is experimentally demonstrated and the effect of separation distance from a coupling antenna is quantified and modeled using a modified Butterworth-van Dyke model. This device has the potential to be a wireless implantable sensor that is much closer to the biomagnetic signal source.

Via optimization of the mechanical coupling, flux concentration, alignment of Metglas magnetic domains, and a (1-x)[Pb($Mg_{1/3}Nb_{2/3}$)O_3]-x[$PbTiO_3$] (PMN-PT) d_{33} macro fiber composite to improve piezoelectric response; resulting in a magnetic field sensitivity of 50 pT at 20 Hz for a d_{33} Metglas/PMN-PT laminate. Mechanical coupling is improved by reducing the thickness and porosity of the epoxy. The Metglas residual stress reduction

and easy axis alignment is accomplished by a 30 minute 400 °C anneal under a 160 mT magnetic field in an oxygen free environment. Resulting in the highest reported magnetostriction coefficient of 79.3 $\frac{\mu m}{m \cdot mT}$. Finally, different piezoelectric materials and configurations such as single crystal PMN-PT and macro fiber composite PMN-PT are explored.

A novel magnetometer consisting of chip-scale whispering gallery mode resonators with high-Q factors (>10^7) are realized using MEMs fabrication techniques. A permanent magnet is elastically coupled to a whispering gallery mode borosilicate microbubble. Magnetic forces from applied external magnetic fields induce deformation in the microbubble which can be sensitively monitored through changes in the optical resonance characteristics. The force is calculated and the the resultant deformation is simulated in the microbubble. The effect of different permanent magnet orientations and microbubble shell thickness is experimentally investigated and modeled. A sensitivity of 1.9 GHz/mT on a microbubble with 1.1 μm shell thickness is experimentally demonstrated along with a limit of detection of 6×10^{-8} T/$\sqrt{\text{Hz}}$ at 30 Hz, which was limited by a noisy laser system.

Finally, this dissertation demonstrates the passively-powered wireless operation of a magnetoflexoelastic magnetometer. The wireless coupling is achieved using coupled near-field resonant loop antennas, which excite the high Q-factor (∼6000) micromachined quartz resonator. Magnetostrictive curves are acquired both wired and wirelessly at distances up to 45 mm to confirm the phenomenon is magnetoflexoelastic in nature. A 49.1 Hz/Oe sensitivity was achieved in wireless operation and the ultimate detectable limit was 7 μT at 0.5 Hz. Highly sensitive, wirelessly powered, and maintenance-free sensors are of great interest to the biomedical, geological, hazardous environment, and traffic control communities.

Table of Contents

List of Figures

List of Tables

Acknowledgments

First and foremost I must acknowledge the direction, faith, freedom and guidance from my advisor, Professor Srinivas Tadigadapa. His unparalleled experience and creativity made this work possible. I would also like to thank Professor Susan Trolier-McKinstry for her insight in piezoelectrics and tireless commitment to her students. I am indebted to Ian Gilbert and John Unguris of NIST for their SEMPA contributions and insightful conversations. Thank you to Professor Steven J. Schiff for insight into biomagnetic sensing. Thank you to Professor Roman Engel-Herbert your guidance in magnetic materials. I would also like to thank Professor Jerzy Ruzyllo for serving on this committee.

Thank you to Nishit Goel and Joshua Harper for helping me assemble and test the many dozens of magnetoelectric devices. Thanks to Professor Christopher Rahn, Nishit Goel and Kentaro Miura for their help with the vibrometer measurements on thin films. Thank you to Gohkan Hotipoglu for contributions to the Quartz fabrication, Paul Nordeen and Professor Gregory Carman of UCLA for RF testing the wireless magnetometer. Cheng-Yu Wang, Alexander Cocking, and Professor Zhiwen Liu provided invaluable support in whispering gallery resonator testing. Thank you to Vedant Sumaria and Chenchen Zhang for assistance in microbubble fabrication development. I greatly appreciate Metglas Inc. for supplying all of our metglas foils at no cost. A big thank you to the staff of the nanofabrication facility at Penn State. Special thanks to all of the members of the Micro and Nanoscale Devices group at Penn State University.

Finally, I would like to thank Alex Bobrov, a family friend, who showed me how to build my first computer when I was just a child and sparked an interest in electronics in me.

This work was funded by the National Institute of Health (NIH) grant no. 1R21EY026438-01 and National Science Foundation (NSF) grant no. 1305663.

Dedication

This dissertation is dedicated to my lovely fiancée Annie Klodd, who has been with me from the beginning of this journey. Her love, patience, and support kept me focused and motivated in the tough times.

Chapter 1

Magnetometers

1.1 Introduction to Magnetometers

There are a plethora of ways to sense magnetic fields. Many methods are based on the intimate relation between magnetic and electronic phenomenon, others are based on force transduction, and the most sensitive methods exploit quantum phenomenon to measure fields as low as a quanta of magnetic flux. No single sensor technology has the dynamic range to measure the entire range of magnetic fields that may be of interest. Magnetic fields from biological processes such as brain function can be as low as 1×10^{-14} T [1] and ultra high field magnetic research has been done on fields on the order of 45 T [2]. A sensor with 1×10^{16} T dynamic range does not exist and furthermore some sensors have limited frequency responses and others fundamentally rely on time varying magnetic fields and have limited DC and low frequency responses. Low field 1×10^{-14} T to 1×10^{-10} T sensing is of particular interest to the biomedical community, however only superconducting quantum interference devices (SQUID) are approved for use for magnetoencephalography (MEG), sensing of the magnetic field from the brain, and magnetocardiography (MCG), sensing of the magnetic field from the heart. Unfortunately, SQUIDs require a superconducting state to work and must operate in liquid helium and the cost of a machine and facilities is 1 to 3 million USD [3], making these tests inaccessible to many people. As a result there has been a strong push to develop a low cost, room temperature magnetometer capable of probing MEG and MCG. Only in the last few years, spin exchange relaxation free atomic magnetometers have proven to exceed the resolution of a SQUID sensors at room temperature in some

situations. However, it requires a near zero magnetic field environment, the device must be heated to >100 °C and it requires optical probing and excitation.

1.1.1 Biomagnetic Applications

Magnetic signals emanating from the body have been characterized and collected from several organs as seen in figure 1.1(a). This diagnostic technique is of particular interest due to the non-contact remote monitoring capability as opposed to wired electrical methods. These signals range from sub 1 Hz to the low 100's of Hz range and can be as low as 10's of fT for cortical activity and up to approximately 80 pT for cardiograms. Magnetoencephalography is being utilized in clinical applications to help diagnose epileptic patients [4] and magnetocardiography is being used to diagnose coronary artery disease and cardiac arrhythmias [5].

Figure 1.1(b) shows the sensitivity and dynamic range of select magnetometer technologies. From the figure it is clear that SQUID magnetometers are the most sensitive, yet several new technologies like magnetoelectric, atomic magnetometers and diamond nitrogen-vacancy magnetometers are strong competitors to replace SQUIDs. Search coils, also known as induction loops, are simply coils of wire wrapped around a ferromagnetic core. These are among the simplest magnetic sensors and function based off of Faraday's law of induction $V = -n\frac{d\Phi}{dt}$, where the induced voltage V is equal to to the change in magnetic flux over time $\frac{d\Phi}{dt}$ times the number of turns in the coil, n. This also means the sensor will not be as sensitive to low frequency magnetic fields. Despite this limitation, Baule and McFee use two large search coils to perform the first magnetocardiogram. However, the coils were large and could not map the heart [6].

The rest of this section is devoted the introducing various contemporary magnetometer technologies. The technologies are separated into non-force sensitive and force-sensitive technologies. Non-force sensitive technologies discussed in this chapter are SQUIDs, magnetoresistance (anisotropic magnetoresistance, giant magnetoresistance, magnetic tunnel junction), Hall sensors, fluxgate, diamond nitrogen-vacancy magnetometers, and atomic magnetometers. Some of these magnetometers take advantage of the Lorentz force, which is ofcourse a force, however if the sensor has no moving parts this dissertation labels it non-force sensitive. Next, force sensitive technologies are discussed: magnetoflexoelastic, magnetoelectric and Lorentz force magnetometers.

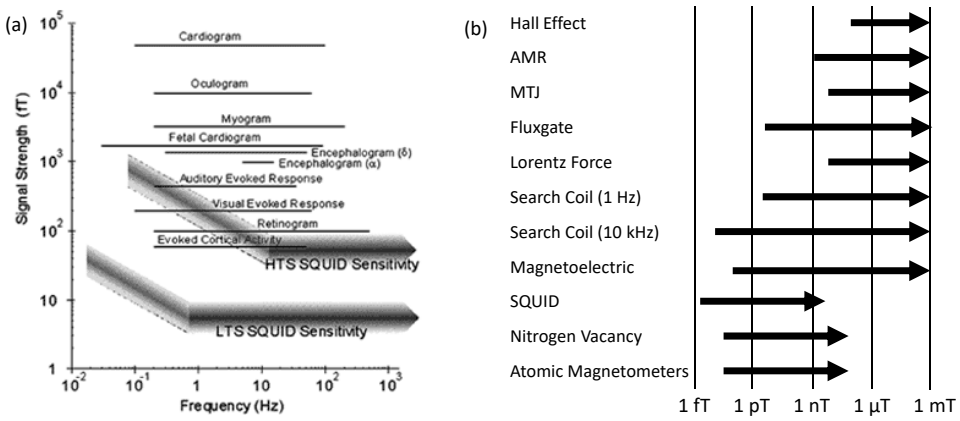

Figure 1.1. (a) Approximate magnetic field strength and frequency range of common biomagnetic signals with low temperature superconducting (LTS) and high temperature superconducting (HTS) SQUID sensitivity limits. Adapted from [7, 1](b) Shows the sensitivity and dynamic range of a select set of magnetometer technologies, including anisotropic magnetic resistance (AMR) magnetometers, and magnetic tunnel junction (MTJ) magnetometers. Adapted from [8, 9]

1.2 Non-force Sensitive Magnetometers

1.2.1 SQUID Magnetometer

The superconducting quantum interference device (SQUID) is an extremely sensitive magnetometer which is capable of sensing single digit fT/$\sqrt{\text{Hz}}$ magnetic fields [10]. The noise is low on these sensors, in part because the entire device and accessory electronics are cooled to cryogenic temperatures (liquid helium for the most sensitive applications) because the sensor requires superconductors to operate and the low temperatures produce minimal Johnson noise in the electronics. The DC SQUID device was first experimentally demonstrated by Robert Jaklevic, et al. in 1964 [11]. The fundamental operating principle is based on the Josephson effect, which was conceived by Brian David Josephson in 1962 [12] and was later awarded the Nobel prize for this discovery.

To understand SQUID magnetometers the Josephson junction must first be explained. The Josephson junction is a device with two superconductors separated by a weak link, like a thin tunneling insulator, through which Cooper pairs can tunnel through. Normally, in a superconducting medium many Cooper pairs "condense" into an electron gas whose wavefunctions are in phase. However, the weak link imposed by the tunneling insulator allows separate out-of-phase wavefunctions to exist. Cooper pairs are a function of electron-phonon interactions at low temperatures and are responsible for some of the

unique properties exhibited by superconductors. The interactions of many Cooper pairs forms an energy gap in the continuous spectrum of the allowed energy states of electrons. This means any excitation must have a minimum energy and small perturbations such as those from phonon scattering is not permitted, hence enabling superconductivity.

Since the current inside of a superconducting ring is described as a wavefunction and it can be shown that the phase (φ) of the wavefunction is described by (1.1) where *n* is an integer, $\hbar$ is the reduced Plancks constant, *e* is the elementary charge of an electron (1.6×10^{-19} C).

$$\varphi = \pm\frac{2\pi n\hbar}{2e} = n\left(\frac{h}{2e}\right) \approx n\left(2.07 \times 10^{-15}\right)\mathrm{Tm}^2 \tag{1.1}$$

This means the phase of a superconducting condensate will go through a full rotation at one flux quanta Φ_0 or $\Phi_0 = \left(\frac{h}{2e}\right) \approx (2.07 \times 10^{-15})\,\mathrm{Tm}^2$. Evaluating the wavefunctions at the insulating barrier yields an equation for the current through a Josephson junction to be (1.2), where *V* is the applied voltage, *t* is time and φ is a starting phase offset. It should be noted that this is an excellent DC voltage to frequency transducer, which is only dependent on the universal constants *h* and *e* and is therefore used as the standardized definition of the Volt.

$$I = I_c \sin\left(\frac{2\pi}{\Phi_0}Vt + \varphi(0)\right) \tag{1.2}$$

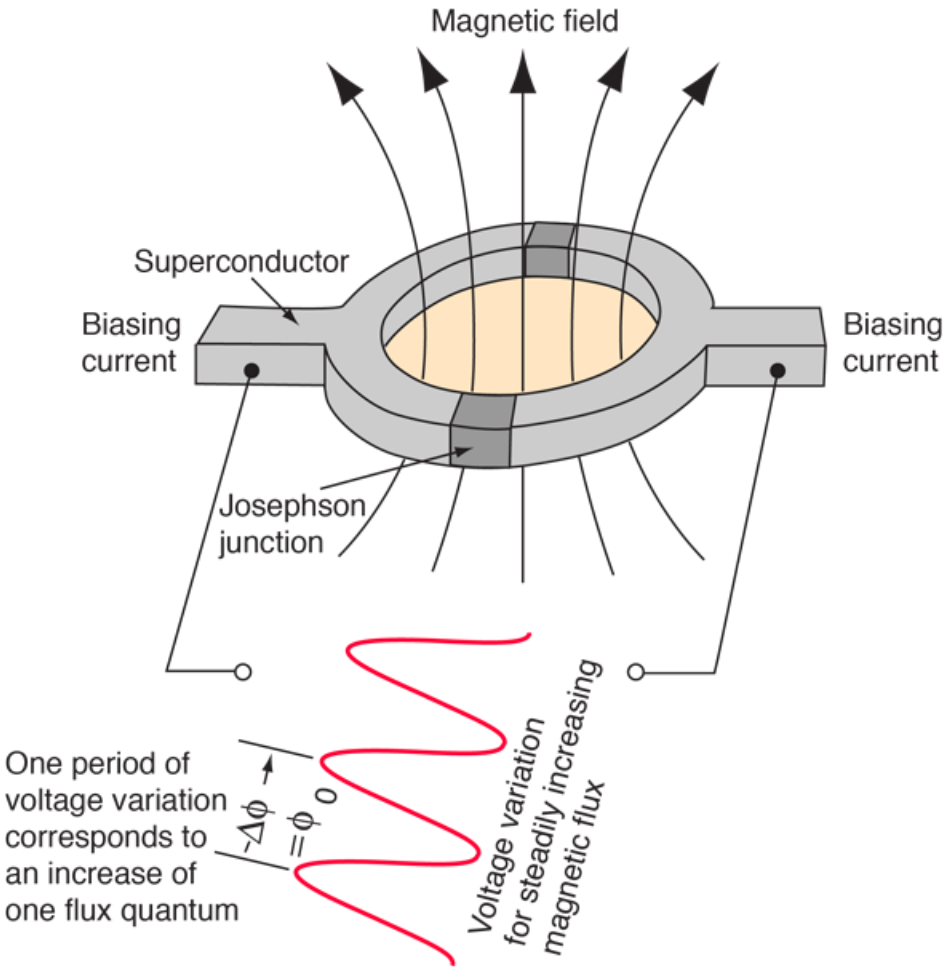

Figure 1.2. Illustration of a DC SQUID device with two Josephson junctions. When biased near or above the critical current an external magnetic flux produces an oscillatory voltage, where each period of oscillation is one flux quanta. [13]

The DC SQUID magnetometer is constructed from two Josephson Junctions as seen in figure 1.2, where two tunneling insulators separate a superconductor. The device is operated just above the critical current (I_c), meaning any additional screening current produces a conventional resistive voltage. Therefore each external magnetic magnetic flux quanta of Φ_0 produces an oscillation of the voltage between the two tunneling insulators, as illustrated in figure 1.2. The current in the DC SQUID device is shown in (1.3) where φ_1 and φ_2 are the phases of the two supercurrents.

$$I = I_c \sin\varphi_1 + I_c \sin\varphi_2 \tag{1.3}$$

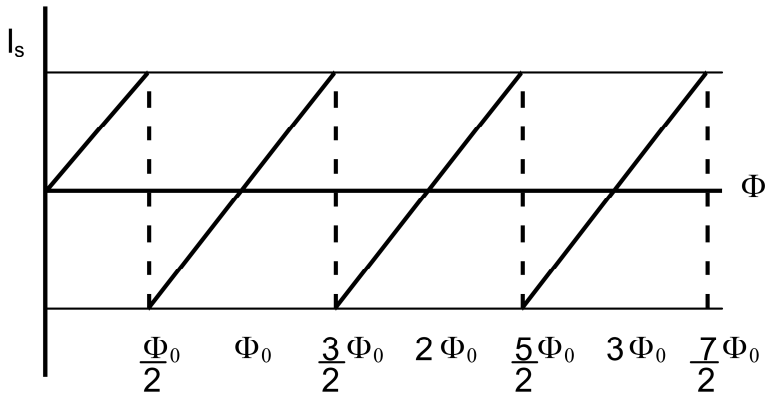

Figure 1.3. Screening current versus magnetic flux quanta relationship.

Using the relationship $\varphi_2 - \varphi_1 = 2\pi n + \frac{2\pi\Phi}{\Phi_0}$, (1.3) can be rewritten as (1.4), where Φ is the external magnetic flux.

$$I = 2I_c \cos\left(\frac{\pi\Phi}{\Phi_0}\right) + I_c \sin\left(\varphi_1 + \frac{\pi\Phi}{\Phi_0}\right) \tag{1.4}$$

The current in the SQUID device oscillation is illustrated in figure 1.3, where it is clear that the current changes direction at at $\frac{n\Phi_0}{2}$. By monitoring the number of voltage oscillations on the SQUID the magnetic flux can be determined with extremely high accuracy. As a result of this sensing method the SQUID magnetometer is fundamentally a differential sensor as it naturally measures a change in the magnetic field as a new biomagnetic signal is generated or decays away.

1.2.2 Magnetoresistance Magnetometer

There are many types of magnetoresistive sensors including anisotropic magnetoresistance (AMR), giant magnetoresistance (GMR), spin valve, magnetic tunnel junctions (MTJ), and colossal magnetoresistance (CMR). This chapter will focus on the more popular technologies, AMR, GMR and MTJs.

1.2.2.1 Anisotropic Magnetoresistance

Anisotropic magnetoresistance sensors were first demonstrated by Lord Kelvin (Michael Thompson). He measured an electrical resistance change $\frac{\Delta R}{R}$ in iron and nickel, where *R* is the resistance with no applied magnetic field and ΔR is the maximum resistance change. The value is usually expressed as a unit-less percent change of resistivity per

Oe. In addition, it has been observed that the resistance is dependent on the angle of the applied magnetic field relative to the current flow.

The magnetization direction in 2-D is given by (1.5):

$$\sin\varphi = \frac{\mathrm{H}_x}{H_k + H_y} \tag{1.5}$$

where φ is the angle of magnetization relative to the anisotropy axis of the ferromagnetic material (H_k). H_x and H_y are the x and y components of the external magnetic field respectively. The change in resistance is given by (1.6) for current flow directed along the anisotropy axis ($\varphi = \vartheta$), where $\frac{\Delta\rho}{\rho}$ is the magnetoresistivity coefficient. [14].

$$\begin{aligned} \frac{\Delta R_x}{R_{xm}} &= -\frac{\Delta\rho}{\rho}\sin^2\vartheta \\ \frac{\Delta R_x}{R_{xm}} &= -\frac{\Delta\rho}{\rho}\frac{\mathrm{H}_x^2}{(H_k + H_y)^2} \end{aligned} \tag{1.6}$$

Anisotropic magnetoresistance requires that a material be ferromagnetic and have magnetic anisotropy. This can result in mobile electrons seeing a different scattering cross-sections depending on the direction of current flow relative to the magnetization of the ferromagnetic material. Permalloy ($\mathrm{Ni}_x\mathrm{Fe}_{1-x}$) and $\mathrm{Ni}_{.80}\mathrm{Co}_{.20}$ are popular choices for anisotropic magnetoresistance devices because of their high resistivity ratios of 3.8 $\%\frac{\Delta\rho}{\rho}$ (for $\mathrm{Ni}_{.76}\mathrm{Fe}_{.24}$) and 6.5 $\%\frac{\Delta\rho}{\rho}$, respectively. A select set of other materials is shown in table 1.1. More comprehensive anisotropic magnetoresistance material overviews may be found in [15, 16]

Material	$\%\frac{\Delta\rho}{\rho}$
$\mathrm{Ni}_{.80}\mathrm{Co}_{.20}$ [16]	6.5
$\mathrm{Ni}_{.76}\mathrm{Fe}_{.24}$ [16]	3.8
$\mathrm{Ni}_{.98}\mathrm{Mn}_{.02}$ [16]	2.9
Fe [17]	0.2
Co [15]	1.9
Ni [18]	2.0

Table 1.1. Room temperature anisotropic magnetoresistance of a select set of alloys and single element ferromagnetic materials.

The $\frac{\Delta R_x}{R_{xm}}$ characteristics for an AMR sensor is shown in figure 1.4 for current oriented parallel, perpendicular or $\pm$ 45° to the anisotropic magnetization. As seen from figure 1.4 the response is approximately linear for small changes in magnetization angle if the current travels 45° to the magnetization axis. Assuming a 45° to the magnetization axis, (1.6) can be approximated as (1.7). Kuijk et al. [19] were able to demonstrate a device where the current almost always travels 45° by using a set of angled "barber pole" like conductors to force the current at an angle as illustrated in figure 1.5.

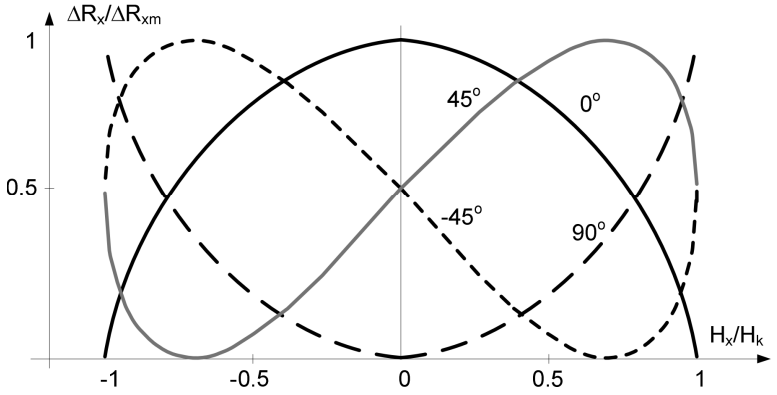

Figure 1.4. $\frac{\Delta R_x}{R_{xm}}$ characteristics for an AMR sensor were current flowing parallel and perpendicular to the magnetization axis (0° and 90°) and with current flowing at $\pm$ 45° to the magnetization axis. The $\pm$ 45° is preferred because it has the better sensitivity at low magnetic field and has a more linear response as compared to the 0° and 90° case. [14].

$$\frac{\Delta R_x}{R_{xm}} \cong -\frac{\Delta \rho}{\rho}\left(\frac{1}{2} \pm \frac{\mathrm{H}_x}{H_k + H_y}\right) \tag{1.7}$$

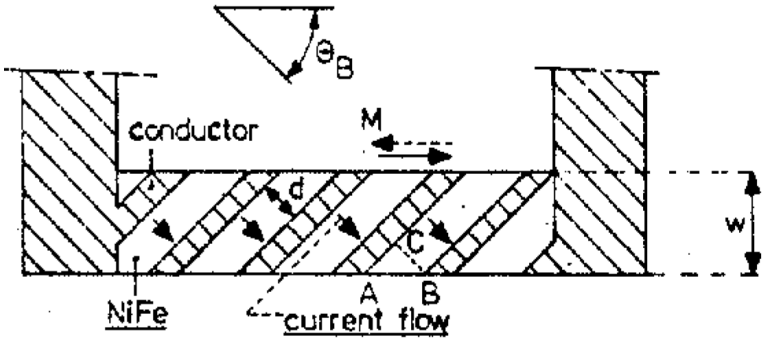

Figure 1.5. Barber Pole AMR sensor, which results in $\pm$ 45° current flow relative to the magnetization direction. The striped areas are low resistance conductors and the background is NiFe. The current will prefer the shortest path "d" in the NiFe. [19]

It is common to have AMR sensors connected into a bridge circuit, resulting a direct conversion of differential resistance to a voltage. As for sensitivity, the Honeywell HMC1001 sensor for example has a specified resolution of 27 nT and is commonly used for compasses [20].

1.2.2.2 Giant Magnetoresistance

Giant magnetoresistance (GMR) was discovered by Albert Ferts and Peter Grünbergs [21, 22]. Similar to other magnetoresistive phenomenon there is a change in electrical resistance in response to a magnetic field. The $\Delta R/R$ in GMR is much larger than in AMR (hence the term giant). The phenomenon is a result of two phenomenon in ferromagnetic metals. First, electrical resistance in metal occurs largely through two independent conducting channels, via spin-up and spin-down electrons and the probability of scattering causing those spins to flip is relatively small compared to other scattering processes, where the spin is conserved. Essentially this means that the two channels do not mix and their conduction occurs in two parallel spin channels [23, 24]. Second, in ferromagnetic metals the scattering probability of the two spins is not equal. This occurs because the density of states between the two spins is not equal and the mobility is inversely proportional to the density of states. Based off these principles, it is evident that conducting electrons with spins perpendicular to the to the magnetization direction will have less scattering and electrons with spins parallel will have more scattering. If a thin conductor is formed from two ferromagnetic materials, one with a pinned magnetization and one with a relatively free axis the electrons thin conductor can experience a state

scattering from either a state where both ferromagnetic materials are aligned and only one spin is strongly scattered (low resistance state, R_P) or a state where the ferromagnetic materials are misaligned and both spins directions strongly scatter (high resistance state, R_{AP}) as illustrated in figure 1.6(a) [25]. Also, this phenomenon can be observed with a thin non-ferromagnetic conductor sandwiched between two ferromagnetic materials. The main problem with GMR sensors is that the anti-parallel state was obtained by strong coupling of the two ferromagnetic layers and the sensitivity was poor. To address this issue a third layer, an anti-ferromagnetic material, is used to pin one of the layers [23]. This is known as a spin-valve sensor. The GMR sensor can operate in fields as low as 10 nT and as large as 0.1 T [8]. The upper limit is because high fields can de-magnetize the pinned layer.

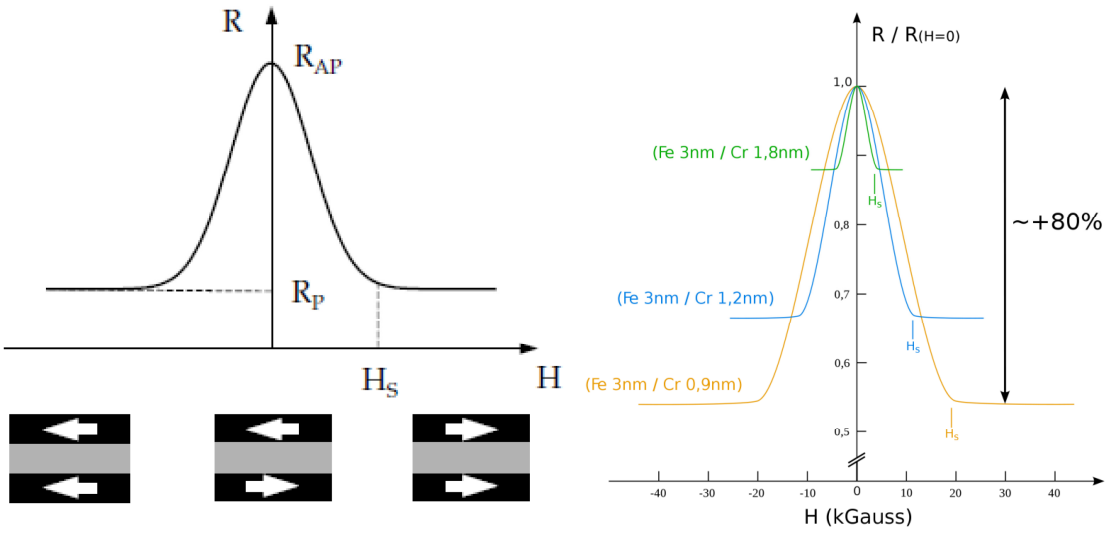

Figure 1.6. (a) Illustration of $\Delta R/R$ in response to the free ferromagnetic layer rotation relative to the pinned layer. In the parallel state the resistance, R_P, is minimum and in the anti-parallel state the resistance, R_{AP}, is maximum. (b) Experimental results of $\Delta R/R$ for thin layers of Fe and Cr superlattices at 4.2 K. Adapted from [25, 21]

1.2.2.3 Magnetic Tunnel Junctions

Magnetic tunnel junction (MTJ) magnetometers have demonstrated even higher $\Delta R/R$ than GMR devices. In conventional tunneling of carriers, through a thin barrier straddled by non-ferromagnetic metals, there are approximately equal density of states available for both spin up and spin down states for carriers to tunnel into. Similarly, there are

approximately equal amounts of both spins available for tunneling on the source side. In direct tunneling, electrons must preserve their spin and can only tunnel into a subband with the same spin orientation. Ferromagnetic metals have an imbalance in their spins with a higher density of states available for the majority spin. This means a condition of density of states mismatch may be produced where there are not enough states for the majority carrier of the source electrode to tunnel into the drain electrode and there are not enough minority spins on the source side to fill the available majority density of states on the drain side. A MTJ is fabricated from two ferromagnetic materials straddling a thin insulator. Figure 1.7(a) illustrates a device with parallel aligned magnetization resulting in matched density of states on both sides and maximum tunneling current. Figure 1.7(b) illustrates an anti-parallel magnetization with minimum tunneling current.

Significant advances in this field came when a series of theoretical papers which predicted that coherently matching the MTJ electrodes crystal structures would result in better spin-dependent matching of the tunneling states [26, 27]. Using MgO as the tunnel barrier the MTJ electrodes can be crystallographically coherent. MgO readily orients into an (001) texture and can used to coherently crystallize the MTJ electrodes during post-deposition anneals, as has been demonstrated for $(CoFe)_{80}B_{20}$/MgO/$(CoFe)_{80}B_{20}$ multilayers [28]. Building on that work, Co/MgO/Co multilater MTJs with tunneling ratios of 400% were achieved [29]. Commercial MTJ sensors can achieve approximately 1 nT/$\sqrt{\text{Hz}}$ [30].

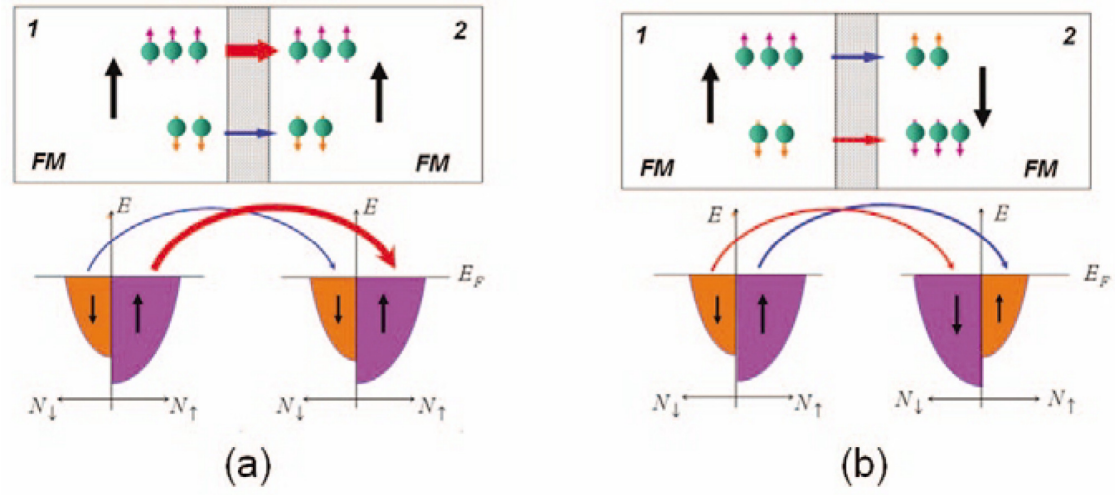

Figure 1.7. (a) Illustration with both ferromagnetic elements aligned parallel to each other producing the maximum availability of density of states where tunneling can occur. (b) Illustration of ferromagnetic elements with anti-parallel alignment where the majority spin on side 1 is lacking states on side 2 to tunnel into. Similarly, the minority spins on side 1 do not have enough carriers to satisfy all the of the majority spin states available to tunnel into on side 2. [31]

1.2.3 Hall Magnetometers

The Hall effect, discovered by Edwin Hall in 1879, is a common technique used for determining free carrier concentration (N_s), carrier type (*n* or *p*), and mobility (μ) with the application of a known magnetic field. Conversely, if the material parameters are known, an unknown magnetic field can be measured. The fundamental operating principle relies on the Lorentz force, given by (1.8), where $\overrightarrow{F}$ is the resultant force, $\overrightarrow{E}$ is the electric field, $\overrightarrow{v}$ is the particle velocity, q_o is the magnitude of the charge of the particle, and $\overrightarrow{B}$ is the magnetic field. The first term is not dependent on the magnetic field but the second term is a cross product of the velocity vector and magnetic field vector, implying that maximum force occurs when the particle velocity is perpendicular to the magnetic field. A typical Hall bar structure is illustrated Fig. 1.8 with the electrodes labeled 1-4. Other Hall structures which use from 4 to 8 electrodes are also commonly used [32].

$$\overrightarrow{F} = q_o\overrightarrow{E} + q_o\overrightarrow{v} \times \overrightarrow{B} \tag{1.8}$$

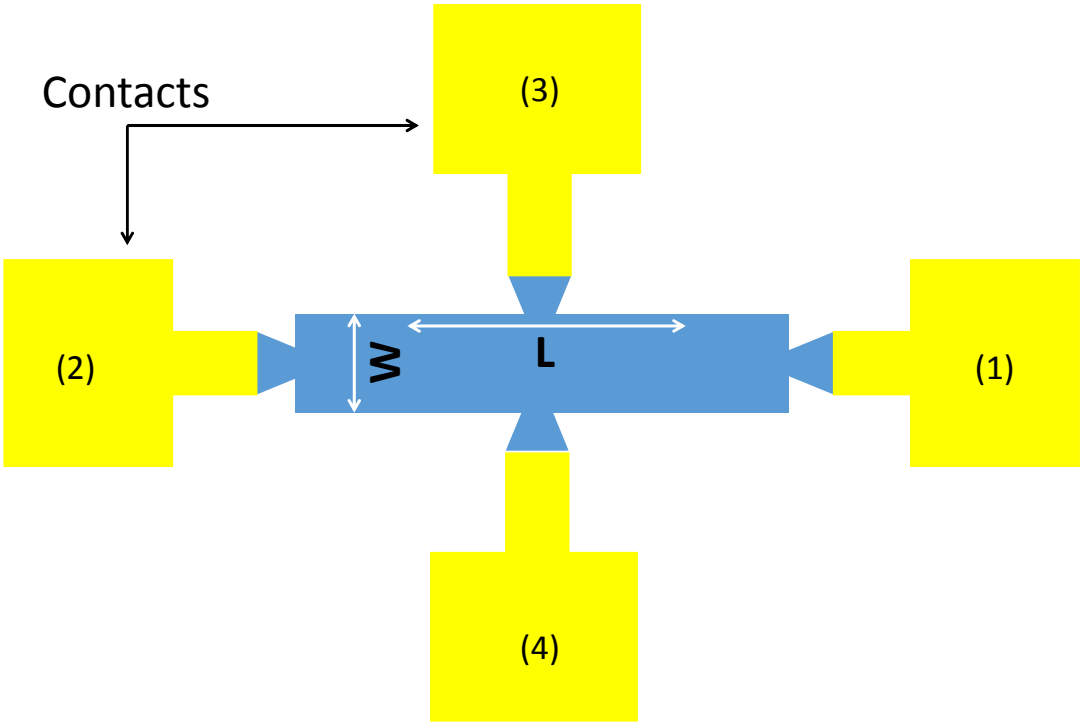

Figure 1.8. Schematic of a typical Hall bar. A DC voltage is applied between electrodes 1 and 2. The resultant Hall effect voltage is sensed on electrodes 3 and 4.

The induced Hall electric field along the length w can be expressed as E=V_H/w, therefore for a magnetic field perpendicular to the Hall bar the Hall voltage V_H is given by (1.9). The negative sign is a result of electrons, which are negatively charged, being the fundamental charge carrier. Based on the right hand rule and assuming an *n*-type material, a *B* field directed out of the page and with a current flowing from electrode 2 to 1 (electrons flowing 1 to 2), the voltage on electrode 3 relative to electrode 4 would be positive as electrons accumulate on the side of the 4 electrode.

$$V_H = -vBw \tag{1.9}$$

The drift velocity, v can be expressed as (1.10) where I is the current between contacts 1 and 2, q is the elementary charge constant (1.6 x 10^{-19} C), N is the number of carriers per volume, A is the cross section ($w \times t$), with t being the thickness of the hall bar. Some popular Hall magnetometer materials are InSb and InAs, which have very high carrier mobilities of 80,000 cm^2/Vs [33, 34] and 33,000 cm^2/Vs [34] respectively.

$$v = \frac{I}{qNA} \tag{1.10}$$

Finally, (1.10) is substituted into (1.9) to get (1.11).

$$V_H = -\frac{IB}{qNt} \tag{1.11}$$

The Hall magnetometers must be powered and the signal of the sensor is proportional to the current. Typical sensors consume 100-200 mW of power and have a magnetic limit of detection in the range of 100 nT and can sense AC and DC magnetic fields. Some specially designed hall probes with large active areas can sense down to 2 nT [35].

1.2.4 Fluxgate Magnetometers

Fluxgate magnetometers consist of a ferromagnetic material wound by 2 coils, as illustrated in figure 1.9. One coil, the drive coil, induces a sinusoidal magnetic field that pushes the ferromagnetic material into saturation every half cycle as illustrated in the B-H hysteresis ferromagnetic loops in figure 1.9. As illustrated in the B-H curves, the reluctance of the ferromagnet decreases and less external magnetic field enters the ferromagnet. Thus the sense coil voltage is proportional to the external magnetic field, which due to the symmetric nature of the B-H curves oscillates at twice the drive frequency and the amplitude of this 2^{nd} harmonic is proportional to the external magnetic field.

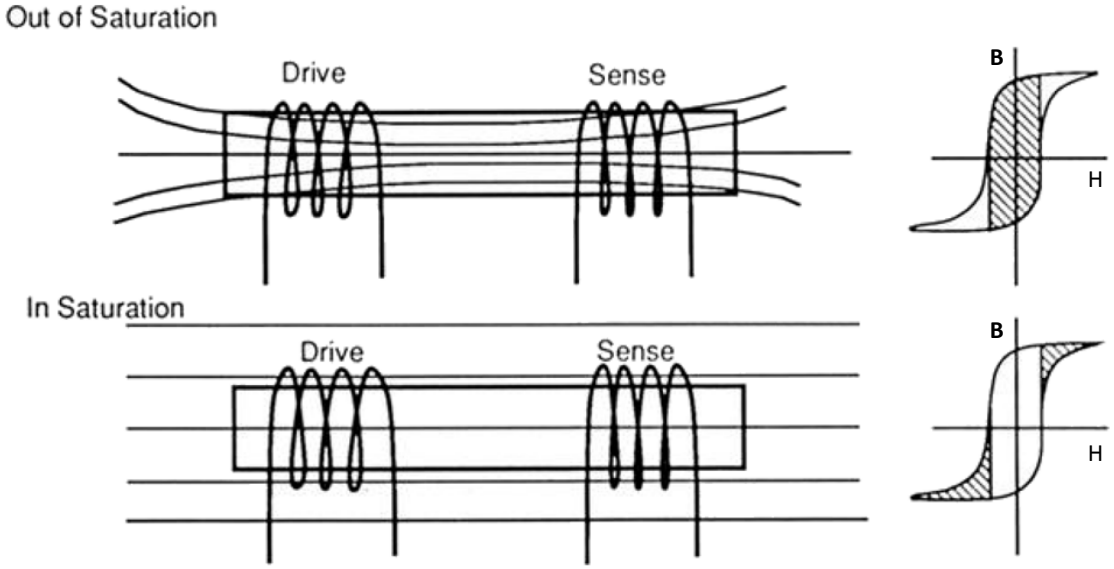

Figure 1.9. Illustration of a fluxgate magnetometer composed of a ferromagnetic material defining the core with a drive and sense coil. Out of saturation the external magnetic field is easily absorbed in the high μ_r material. As the drive coil pushes the ferromagnetic core into saturation the external magnetic field is not concentrated into the saturated ferromagnetic core. B-H loops on the right illustrate the two situations in the core. Adapted from [8]

It is common to find fluxgate devices connected in series as seen in figure 1.10(a) in a bar configuration and figure 1.10(b) in a circular configuration, to cancel out the drive and odd harmonics of the device. Assuming a frequency selective amplifier is used to lock in to the second harmonic, the magnitude of the output signal can be estimated as (1.12) as adapted from [36].

$$V \approx NA\mu_r\mu_0 H_m f \frac{1-D}{\left[1+D(\mu_r-1)\right]^2} \tag{1.12}$$

where *N* is the number of turns on the secondary coil, f is the frequency, μ_r is the relative permeability of the ferromagnetic core, μ_0 is the permeability of freespace and H_m is the external magnetic field. It is typical to find fluxgate devices with limits of detection of approximately 10 pT, owing to the fact that noise can be significantly reduced using a lock-in amplifier due to the high frequency nature of the output signal.

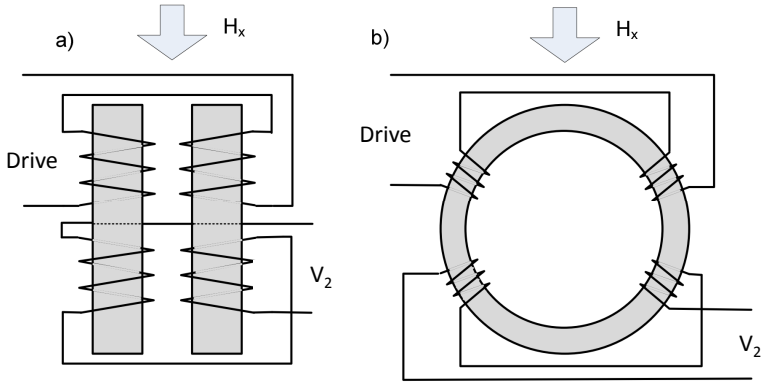

Figure 1.10. Illustration of dual fluxgate magnetometers in a (a) bar configuration or (b) circular configuration where two ferromagnetic cores produce out of phase magnetic signals to cancel out the drive and odd harmonics [36].

1.2.5 Diamond Nitrogen-Vacancy Magnetometers

The nitrogen-vacancy (NV) center is a defect formed in diamond by one substitutional nitrogen and a neighboring vacancy. This can be achieved by implanting diamond with nitrogen ions and subsequently annealing to recombine the nitrogen with vacancies [37]. The spins and energy levels resulting from this defect are illustrated in figure 1.11(a). The defect forms a ground state ^3A spin triplet ($m_s = \pm 1$ and m_s = 0) that can be adjusted at room temperature using electromagnetic fields (in the microwave region). Furthermore, there is a triplet excited state ^3E and an upper singlet state $^1A_1$ which decays through a 1042 nm transition into a metastable ^1E singlet state with a relatively long 200 ns lifetime, which then further decays back to the ground state [38]. The $^1A_1$ state is populated by a spin-nonconserving transition which occurs at a higher probability from the $m_s = \pm 1$ than the m_s = 0 from the ^3E excited state [39]. The ^3E excited state is populated via spin-dependent transitions from $^1A_1$, where $m_s = 0$ ground states are forbidden from populating $m_s = \pm 1$ excited states [40].

In the presence of an electromagnetic field at the resonance of the $m_s = 0 \rightarrow m_s = \pm 1$ transition (approximately 2.8 GHz) the $m_s = -1$ and the $m_s = 0$ energies in the ground state will overlap and have spin-polarization, which strongly effects the optical absorption and luminescence between those states enabling more $m_s = \pm 1$ excited states. The $m_s = \pm 1$ excited states in turn decay into more $^1A_1$ and subsequently more filled ^1E states, resulting in increased absorption at 1042 nm as seen in figure 1.11(b), which shows two dips, one for the $m_s = -1$ and the other for the $m_s = +1$ spin in response to

splitting from a 2.99 mT magnetic field.

In the presence of a magnetic field, Zeeman splitting occurs in the $m_s = \pm 1$ states resulting a shift of the resonance frequency [41] $f_{res} = D \pm \gamma B \cos\theta/(2\pi)$, where D is the zero-field splitting of the NV ground state (2.87 GHz), γ is the gyromagnetic ratio for the NV center $\gamma = 2 \times 28.0$ GHz/T and θ is the angle between the NV axis and the applied field. Fields as small as 2.4 nT/$\sqrt{\text{Hz}}$ have been demonstrated, but theoretical predictions for larger ensembles of NV diamond defects predict resolutions as small as 240 fT/$\sqrt{\text{Hz}}$ [40].

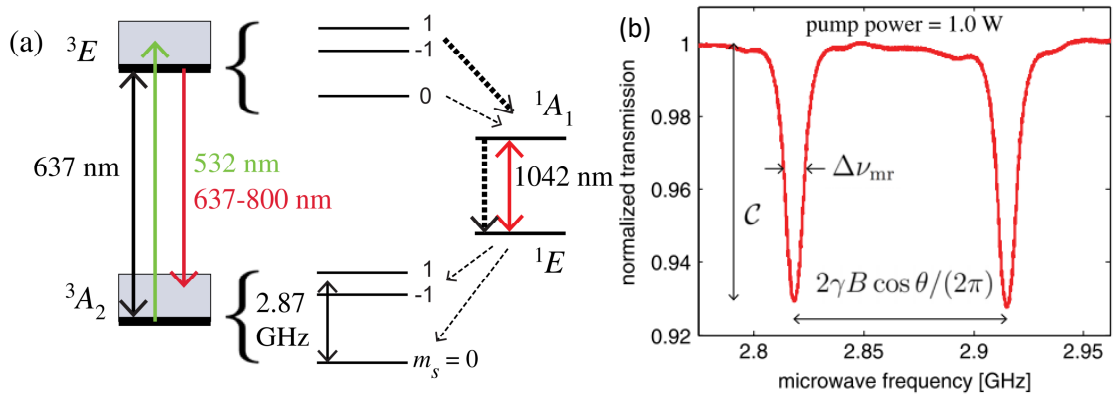

Figure 1.11. (a) Transition levels of the NV defect center in diamond. Solid lines are radiative transmissions, which are spin dependent. Dashed lines are spin-nonconserving transitions. (b) Normalized transmission showing the microwave resonance of the ground state transitions one for the $m_s = -1$ and the other for the $m_s = +1$ spin in response to splitting from a 2.99 mT magnetic field [40].

1.2.6 Atomic Magnetometers

Atomic magnetometers do not require cryogenic cooling and have been demonstrated with sensitivities that rival and even exceed SQUID magnetometers in some situations [42]. However, they do not scale well and require various optical components to operate. Atomic magnetometers function by probing the allowable optical absorption frequencies, which are magnetically coupled by Zeeman splitting. Alkali metals atoms are chosen because of their lone valence electron which dominates the spin properties of the material. The energy levels of an alkali metal is illustrated in figure 1.12(a) which has 2 possible transitions *D1*, and *D2* from the one *s* to two *p* levels. Each of the levels has two Zeeman spin states $m_j = -1/2$ and $m_j = +1/2$. The the alkali metal is optically pumped with

a circularly polarized laser imparting an angular momentum σ^+ which only allows the $^2S_{1/2}$ $m_j = -1/2$ to the $^2P_{1/2}$ $m_j = +1/2$ transition to occur. The excited Zeeman levels mix due to collisions with the buffer gas and quickly decay to the ground state via radiative quenching into either ground state. Eventually, the $^2S_{1/2}$ $m_j = +1/2$ becomes saturated since those electrons can not be excited into the excited state and the $^2S_{1/2}$ $m_j = -1/2$ is emptied, resulting in nearly perfect $m_j = +1/2$ polarization of the gas [43] as illustrated in figure 1.12(b). This condition only occurs when the circularly polarized light is resonant with with $D1{+}m_{j=-1/2}$ transition. In this way the exact Zeeman shift due to a magnetic field can be probed by carefully sweeping the circularly polarized laser frequency and checking for an induced polarization in the alkali gas, which may be probed by linearly polarized laser (off-resonance from the alkali gas) [44]. It should be noted that σ^- would result in a similar phenomenon by populating the $^2S_{1/2}$ $m_j = -1/2$ state. Spin relaxation from the polarized state to the un-polarized state reduces the response of the effect.

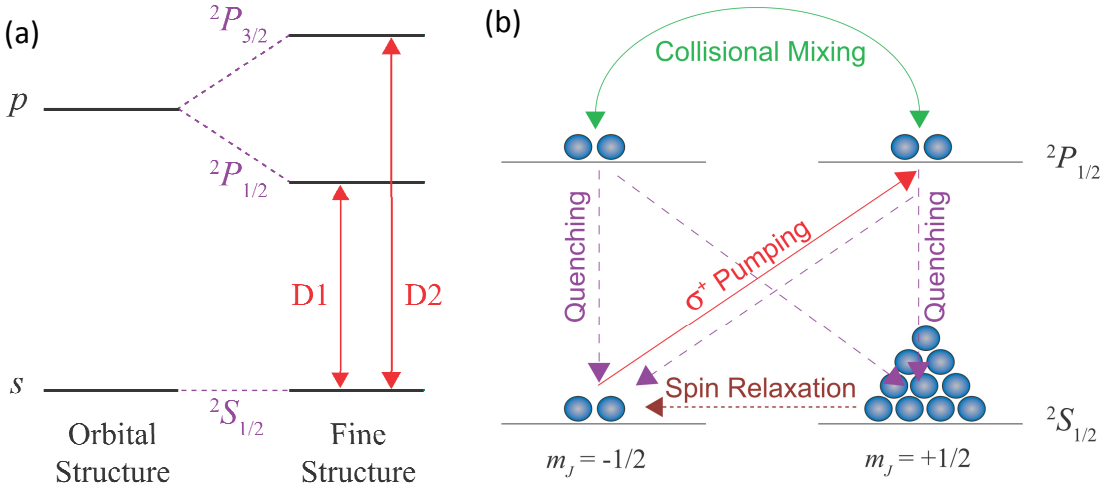

Figure 1.12. (a) Transition levels of an alkali metal. Where the ground $^2S_{1/2}$ level and 2 excited $^2P_{1/2}$ levels each have two spin states $m_j = -1/2$ and $m_j = +1/2$. (b) Under σ^+ circularly polarized light excitation only the $^2S_{1/2}$ $m_j = -1/2$ to $^2P_{1/2}$ $m_j = +1/2$ transition is allowed. Collision mixing results in excitation in both $^2P_{1/2}$ spin levels, which quickly radiatively quench into both $^2S_{1/2}$ levels. Eventually the $^2S_{1/2}$ $m_j = -1/2$ is depleted and the $m_j = +1/2$ is full, resulting in near perfect polarization which may be probed by linearly polarized laser. Adapted from [44].

The Zeeman splitting in the alkali gas is similar in principle to the Zeeman splitting

that occurs in the nitrogen vacancy center in diamond discussed earlier in section 1.2.5. The Larmor precession frequency is given by $\omega = \gamma |B|$, where *B* is the magnetic field. The gyromagnetic ratio (γ) is (1.13)

$$\gamma = g\mu_B/\hbar(2I+1) \tag{1.13}$$

where *I* is the nuclear spin of the alkali metal (approximately zero), g is the dimensionless magnetic moment and is approximately 2, and μ_B is the Bohr magneton.

The shot noise limited sensitivity of the atomic magnetometer is given by (1.14) [45]

$$\delta B = \frac{1}{\gamma\sqrt{nT_2VT}} \tag{1.14}$$

where *n* is the number density of atoms, T_2 is the transverse spin relaxation time, *V* is the measurement volume and *t* is the measurement time.

The great breakthrough in enabling sub-fT sensing of magnetic fields using atomic magnetometers was the demonstration of spin-exchange relaxation-free (SERF) magnetometers which enabled theoretical shot noise sensitivity to be reduced to 0.01 fT/Hz$^{-1/2}$ in a 1 cm^3 cell [46, 47]. In a high density alkaline vapor in a near zero magnetic field the rate of spin-exchange is much quicker than the Larmor frequency. When two polarized atoms collide, the electrons can transition into the other hyperfine state and precess in the opposite direction from the bulk of the ensemble, thereby causing de-coherence and loss of signal. Spin-exchange relaxation is suppressed if the spin-exchange collisions happen fast enough in a sufficiently low magnetic field. In such a regime, the spins do not have enough time to precess and decohere between collisions. Therefor the T_2 is significantly increased and the magnetometer limit of detection is lower.

1.3 Force Sensitive Magnetometers

1.3.1 Magnetoelectric Magnetometers

Magnetoelectric magnetometers have recently become a bio-magnetic relevant technology with authors reporting sub 100 pT sensitivity [48]. While not yet sensitive enough to resolve MEG signals, the magnetoelectric magnetometer can potentially resolve MCG and other biomagnetic sensing is possible [49]. Magnetoelectric magnetometers have been researched heavily owing to the fact that they are inexpensive and relatively simple

to fabricate. The $PbZr_xTi_{1-x}O_3$ (PZT) based devices described in this dissertation cost approximately $10 USD each to manufacture and the (1-x)[$Pb(Mg_{1/3}Nb_{2/3})O_3$]-x[$PbTiO_3$] (PMN-PT) devices were on the order of $150 USD, offering a tantalizing possibility of a highly accessible magnetometer technology with bio-magnetic sensing capability at room temperature.

Magnetoelectric magnetometers utilize the magnetostrictive phenomenon of ferromagnetic materials and couple it to the piezoelectric phenomenon in ferroelectric materials. Magnetostriction is defined as a change in dimension of a material in response to an applied magnetic field. Or conversely, a change in magnetic field resulting from a change in material dimensions. Magnetostriction has been observed in single elements materials such as Ni and Co, amorphous compounds such as Metglas (FeSiB) and single crystal materials like Terfenol-D ($Tb_{0.3}Dy_{0.7}Fe_2$). Magnetostrictive strain (λ), measured in unit-less quantity part per million (ppm) has been reported to be up to 2400 ppm for Terfenol-D. Piezoelectric materials such as PZT and PMN-PT exhibit an induced polarization due to an applied stress. Or conversely, a change in dimension resulting from an applied voltage or electric field.

Typical magnetostrictive behavior is non-linear as illustrated on the left half in figure 1.13 showing a strain vs. magnetic field (B_{dc}). Applying a DC magnetic field to bias the magnetostriction film into the linear region allows for the sensing of weak AC magnetic fields. This oscillating magnetic field translates into an oscillating mechanical strain. That strain is then transduced into a charge or voltage by the piezoelectric material as illustrated on the right half of figure 1.13. It is also clear from figure 1.13 that the largest magnetostriction, does not necessarily mean the best magnetoelectric performance, but rather the largest magnetostriction coefficient ($\partial\lambda/\partial$B) is the critical figure of merit for the magnetostrictive material for magnetoelectric applications. Most importantly, the operation of this device depends critically on good elastic coupling between the piezoelectric and magnetostrictive materials.

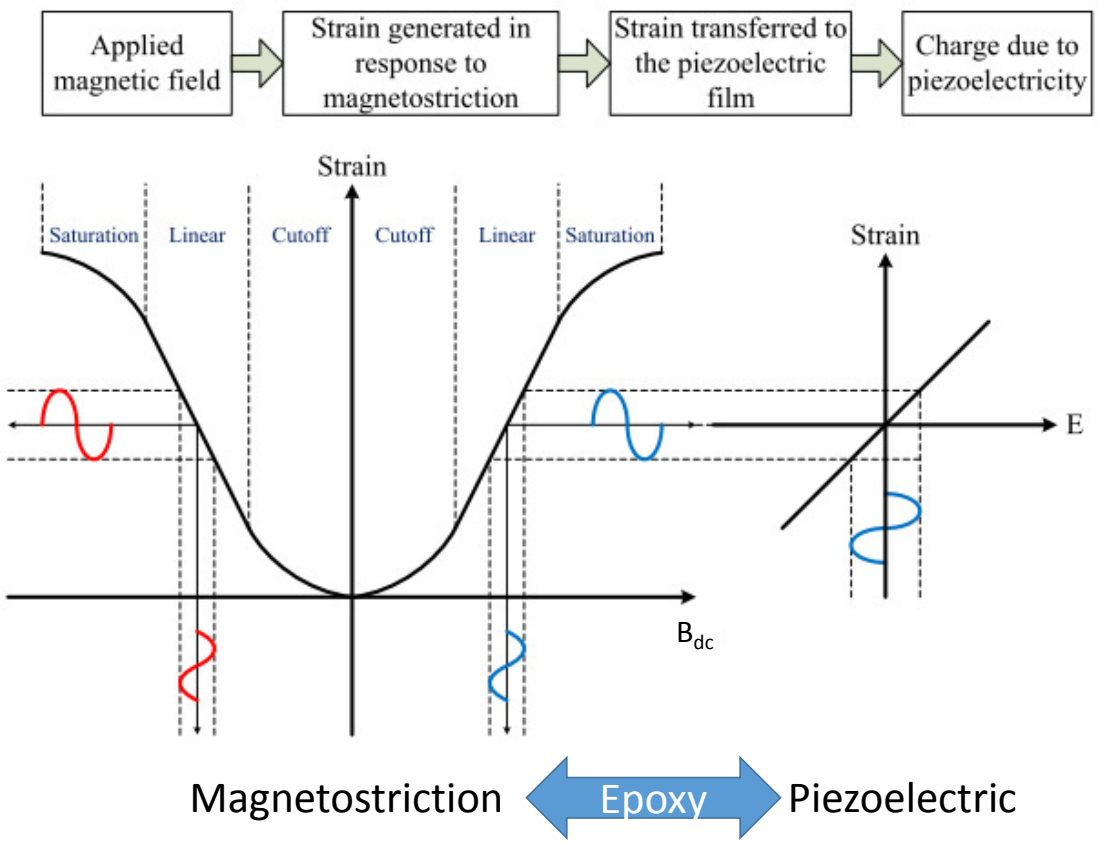

Figure 1.13. Illustration of magnetoelectric phenomenon transferring mechanical energy from magnetostriction to piezoelectric phases [50].

.

The magnetostriction phenomenon is discussed in more detail in section 2.1.1 of chapter 2 where the optimization of the magnetostriction coefficient is in Metglas 2605SA1 is investigated. The piezoelectric phenomenon is discussed in more detail in section 3.2.1. The magnetoelectric effect is discussed in more detail in section 3.2.2.

1.3.2 Magnetoflexoelastic Quartz Magnetometers

A magnetoflexoelastic quartz magnetometer is similar to the magnetoelectric magnetometer in the sense that it couples a magnetostrictive component with a piezoelectric one. The magnetoelectric device directly transduces the strain of the magnetostrictive material to the piezoelectric one, however the magnetoflexoelastic quartz device uses the magnetostrictive material to change the resonance behavior of the high Q-factor quartz

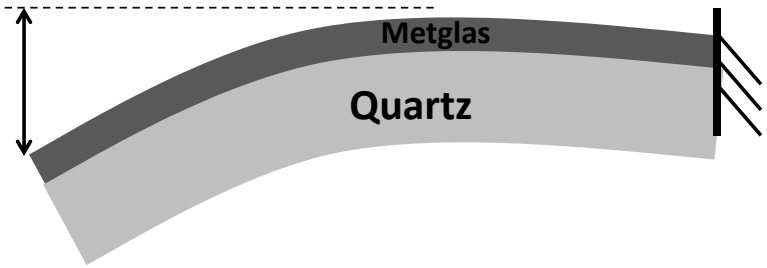

Figure 1.14. Illustration of Metglas material straining a quartz cantilever, causing a shift in the quartz spring constant.

resonance by straining the quartz and shifting the spring constant [51]. Furthermore, the microscale magnetoflexoelastic quartz Magnetometer performance improves as the device is thinned down. A PZT/Metglas device can also potentially be operated in this manner, however the low Q-factor of the Metglas and PZT resonance may limit it's sensitivity.

The thickness shear-mode resonance frequency in quartz is determined by (1.15)

$$f_n = \frac{n}{2t}\sqrt{\frac{c_{66}}{\rho}} \tag{1.15}$$

where n is the mode number (1 for the fundamental mode), t is the quartz thickness, c_{66} is the shear mode elastic constant and ρ is the density of the quartz. The bending induced by the magnetostrictive material is illustrated in figure 1.14 where a quartz cantilever is deflected and the strain causes a shift in the elastic constants, via the second and third order elastic stiffnesses [51], resulting in a shift of resonance frequency. The Magnetoflexoelastic quartz magnetometer is discussed in more detail in section 5.2.

Hotipaglu and Tadigadapa demonstrated 79 nT LOD at 0.2 mHz and predicted sub nT LOD is possible with thinner quartz [52, 51]. It should also be noted that the force-frequency effect has not been evaluated for many piezoelectric materials and much more responsive materials may exist.

1.3.3 Lorentz Force Magnetometers

The MEMS Lorentz force magnetometer is a relatively complex device to manufacture and it requires a vacuum seal to prevent squeeze film damping. Despite these drawbacks these devices are studied because they may be built along side other MEMS sensors

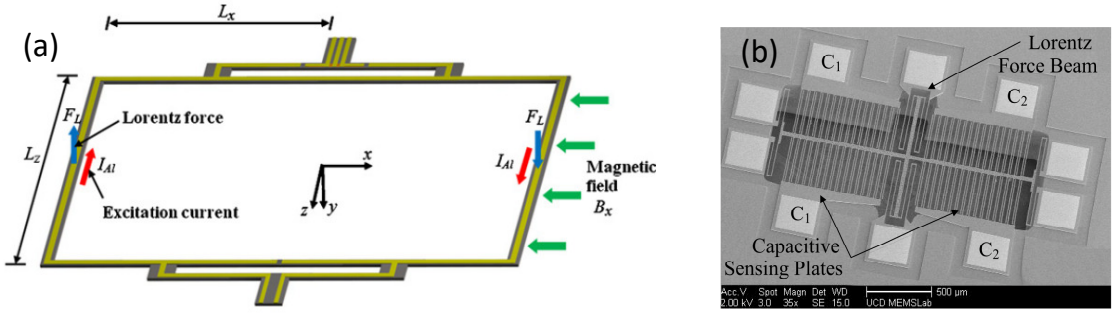

Figure 1.15. (a) Illustration of the operating principle of a Lorentz force magnetometer. The current I_{Al} flows in a loop and when in the presence of a a perpendicular magnetic field B_x produces a force of equal but opposite strengths F_L, on both beams causing the structure to twist [54]. (b) Scanning electron micrograph of a typical Lorentz force magnetometer with capacitive sensing combs. In this case, an out of plane magnetic field forces one set of combs to move in-plane resulting in a change in capacitance [55].

that exist on consumer electronic and mobile-phones like gyroscopes and accelerometers. More importantly, MEMS Lorentz force magnetometers have been demonstrated with lower power consumption than conventional Hall magnetometers. Lorentz force magnetometers have a LOD of 10's to 100's of nT which is sufficient to sense the earths magnetic field [53].

The Lorentz force magnetometer uses the same underlying physics as the Hall magnetometer described earlier in this chapter. Figure 1.15(a) shows the principle of operation of a MEMS Lorentz force magnetometer, where current I_{Al} flows along the beams of a torsional structure and a perpendicular magnetic field B_x produces a force of equal but opposite strengths F_L, on both beams causing the structure to twist. A typical Lorentz force magnetometer uses a comb structure as seen in figure 1.15(b) to increase capacitive cross section, which is driven at its mechanical resonance frequency. The force on the structure is proportional to the current and therefore also at mechanical resonance to improve sensitivity.

1.4 Thesis Objectives and Outline

This dissertation aims to progress the field of magnetic sensing. First an overview of the motivations for researching and developing magnetometers is presented, followed by an overview of contemporary and relevant magnetic sensing technologies.

A thorough understanding of magnetostriction is developed and how it relates to the

magnetoelectric phenomenon. The theory for magnetic domain alignment is discussed and an optimized annealing procedure is experimentally developed which produces the highest possible magnetostriction coefficient in Metglas 2605SA1 foils. Additionally these optimized films are used to demonstrate a substantial improvement in magnetoelectric magnetometers. Next, a comprehensive optimization process of the magnetoelectric sensors is realized by utilizing the optimized magnetostrictive component, optimizing the piezoelectric component, and investigating the elastic coupling between the two.

A novel chip-scale whispering gallery mode magnetometer is proposed and experimentally demonstrated. The concept of optical whispering gallery mode resonance in dielectric mediums is explained and a brief overview of sensors employing this phenomenon is presented. Next the chip-scale glassblowing process is explained and modeled, followed by a detailed process of micro-magnet integration. The magnetometer is modeled in COMSOL and experimentally demonstrated to explore the ideal magnet orientation. The limit of detection is evaluated and the dominating source of noise in the setup is identified.

Finally, a novel passively powered wireless magnetometer is demonstrated using quartz and the magnetoflexoelastic effect. The resonance in quartz is modeled and described using the Butterworth-van-Dyke circuit model and the force-frequency effect is explained and derived. An understanding of near-field antennas and how they interact with their environment is explained. The resonance characteristics and response are modeled using a modified Butterworth-van-Dyke model to include an energy loss component due to the separation distance. Finally, the magnetic limit of detection is measured and compared to a wired version of the device.

Chapter 2

Optimization of Magnetostriction Coefficient in Metglas 2605SA1

2.1 Introduction

The magnetoelectric (ME) effect is the coupling of the magnetostrictive and the piezoelectric phenomena. In multilayered laminate structures, magnetic sensing is achieved by transduction of the magnetostrictive effect, where a strain induced by a magnetic field is elastically coupled to the piezoelectric layer which in turn produces a charge. The electrically induced magnetoelectric effect was first demonstrated in Cr_2O_3 by Astrov [56] and shortly after the magnetically induced variety was observed by Rado and Folen [57]. Philips Laboratories demonstrated that composites can greatly enhance the magnetoelectric effect over single-phase material, achieving a magnetoelectric coefficient of 0.13 MV/(m·T) [58, 59, 60]. The magnetoelectric coefficient is commonly presented in CGS system of units of V/(cm·Oe). In this work the MKS system of units equivalent of MV/(m·T) is used, which results in the same numerical value as the conventional CGS units assuming the test is done in a medium of relative permeability, μ_r, very close to 1 (i.e., 1 V/(cm·Oe) $(\mu_0\mu_r)^{-1}$ = 1 MV/(m·T) for μ_r = 1, where μ_0 is the permeability of free space). The strongest ME effects occur in laminates composed of materials exhibiting strong magnetostriction without piezoelectricity elastically coupled to materials with strong piezoelectricity without magnetostriction; this allows the two crucial phenomena to be separately optimized [61, 62]. This chapter outlines efforts to optimize the magnetostrictive component through a comprehensive analysis of the magnetostriction coefficient,

domain imaging and magnetoelectric coefficient.

Understanding and optimizing the magnetoelectric coefficient is of great interest to the biomagnetic community as a magnetometer [49], remote actuator [63], and implantable pressure sensor [64]. Inexpensive room temperature magnetometers capable of biomagnetic measurements have the potential to replace costlier superconducting quantum interference devices (SQUIDs) and increase patient access to biomagnetic diagnostics. Extensive work is also being done on ME devices for energy harvesting [65, 66]. The soft magnetic properties of magnetostrictive amorphous alloys, like Fe-Si-B [67], have been used in the development of highly sensitive room temperature magnetic sensors. Magnetoelectric coefficients of up to 52 MV/(m·T) and 3 pT/$\sqrt{\text{Hz}}$ at 1 Hz sensitivity for laminates of Metglas and (1-x)[Pb($Mg_{1/3}Nb_{2/3}$)O_3]-x[$PbTiO_3$] (PMN-PT) have been reported [48, 68].

It has been generally established that annealing in the presence of a magnetic field induces an anisotropy and increases magnetostriction in amorphous metallic glasses. Several groups have explored the effect of annealing amorphous metallic glasses on the elastic modulus (ΔE effect) [69, 70, 71, 72, 73], magnetostriction [72, 74, 75, 73], and embrittlement [76]. Annealing optimization has been applied in a limited fashion for magnetoelectric devices [77]. This is because despite the plethora of work in this field, the effects of annealing on ME device performance from one material formulation of amorphous metal does not necessarily translate to other material formulations (some Metglas formulations have near-zero magnetostriction [78]) and, to complicate the matter, the manufacturing of the amorphous metal foils is critical to their performance and varies between suppliers. There is no comprehensive work on a single material that provides clear guidance on how to optimize a Metglas 2605SA1 magnetoelectric device. Furthermore, most work focuses on optimizing the saturation magnetostriction; however it is the magnetostriction coefficient (peak of the slope of the magnetostriction vs. applied magnetic field) which is the crucial figure of merit for a magnetostrictive ribbon for magnetoelectric device applications.

To address these deficiencies the magnetostriction coefficient is calculated from magnetostriction measurements under a variety of annealing conditions. In order to create a comprehensive guide for optimization of Metglas 2605SA1/PZT (Pb[Zr_xTi_{1-x}]O_3) ME sensors through field annealing 4 main factors are considered: 1) temperature 2) time 3) applied transverse magnetic field 4) oxygen in the annealing ambient. Also, these results are correlated with magnetoelectric coefficient measured on Metglas 2605SA1 and

PZT-5A laminates in d_{31} sensing mode. Furthermore, scanning electron microscopy with polarization analysis (SEMPA) is performed to observe the surface domain alignment.

2.1.1 Magnetostriction

The origin of magnetostriction is rooted in the fundamental nature of ferromagnetic materials. The cause of ferromagnetic properties in materials is quantum mechanical in nature. The question of why do individual atoms have magnetic moments and why the moments align must be addressed before the origin of magnetostriction can be explained. As electrons fill the orbitals of an atom, Hund's rule states that it is energetically favorable to fill an orbital shell with the same spin, inducing a dipole moment. Completely filled electron shells have no net dipole moment. However, the paired electrons will align in a magnetic field, giving rise to paramagnetism. Only a few materials experience spontaneous magnetization and can align without an external applied magnetic field.

Spontaneous magnetization occurs because of exchange interaction, which energetically favors electrons of parallel spin over anti-parallel spin. This stems from Pauli's exclusion principle which allows for anti-parallel spins to have overlapping wavefunctions, and forbids parallel spin electrons from existing in the same quantum state. The anti-parallel spins would exist closer together as compared to the parallel state and have a larger coulombic repulsion energy. If the exchange energy extends to neighboring atoms in a solid, and can overcome the magnetic dipole-dipole interaction, the atoms will align and the materials behaves like a ferromagnet.

The spin-orbit interaction of an electron results in magnetization preferences along a certain crystallographic axis. This is due to the electron orbital state being coupled to the crystal structure, resulting in magnetocrystalline anisotropy. For polycrystalline materials the effect may involve several crystallographic axes. Amorphous materials like Metglas can be treated like polycrystalline materials with very small local structural units (crystallites) with a random distribution of local symmetry axes [79]. This magnetization alignment along a crystallographic axis, manifests itself as magnetic anisotropy energy. This is the cause of magnetostriction, as the magnetization rotates so does the crystallographic axis, causing a change in shape.

Magnetostriction is the property of all ferromagnetic materials to change dimensions upon change in magnetization [80]. The magnetostriction effect was discovered by James Prescott Joule when he noticed his materials changed shape when magnetized. The direct

magnetostriction effect, where a material changes shape in response to a magnetic field is called Joule magnetostriction. The inverse, where a stress produces a magnetic field, is called the Villari effect after Emilio Villari. Volume conservation is a hallmark of Joule Magnetostriction, however recent discoveries suggest a Non-Joulian magnetostriction also exists [81].

Magnetostriction has been observed in single element materials such as polycrystalline Ni and Co, single crystals such as Terfenol-D ($Tb_{0.3}Dy_{0.7}Fe_2$) and amorphous compounds like Metglas 2605SA1 (FeSiB). Magnetostrictive strain (λ), measured in unit-less quantity part per million (μm/m) has been reported to be up to 2400 μm/m for Terfenol-D [82]. The non-linear magnetostrictive response shown for Metglas 2605SA1, seen in figure 2.1, has the typical response seen in many magnetostrictive materials. The linear region of λ has the largest slope and produces the largest change in strain per change in magnetic field ($\partial\lambda/\partial$B) and is therefore the region of highest sensitivity for magnetic sensing. To maintain linearity and high sensitivity it is important to have a DC magnetic field to bias a magnetoelectric device into its sensitive linear region.

Metglas 2605SA1 has a relatively small λ_s of 27 μm/m [83] when compared to Terfenol-D and Fe-Ga based alloys, which show a λ_s of 2400 μm/m [84] and 325 μm/m [85], respectively. While a large λ_s is preferable for actuation, sensing applications require a high magnetostrictive coefficient. Metglas 2605SA1 has among the highest reported with $\left(\frac{\partial\lambda}{\partial B}\right)$ = 36 $\frac{\mu m}{m \cdot mT}$ for thin films (magnetically poled in-situ during sputter deposition) [51], compared to 4.0 $\frac{\mu m}{m \cdot mT}$ for Terfenol-D [86]. An increased magnetostriction coefficient results in a larger $\Delta\lambda$ for a given ΔB, and thus the α_{me} will be improved. Further improvements are likely by removing internal stresses which can act as magnetic domain pinning centers preventing the domains from rotating in unison.The λ_s and $\partial\lambda/\partial$B for select magnetostriction materials is shown in table 2.1.

Material	λ_s (μm/m)	$(\partial\lambda/\partial B)$ $\frac{\mu m}{m \cdot mT}$
$Co_{0.8}Fe_{2.2}O_4$	-590 [87]	-1.5 [88]
$NiFe_2O_4$	-36 [87]	-0.5 [88]
Terfenol-D	2400 [89]	4.0 [82]
Galfenol	1500 [89]	3.5 [85]
Metglas 2605SA1 (unannealed)	27 [83]	12

Table 2.1. Saturation magnetostriction, λ_s and magnetostriction coefficient $\partial\lambda/\partial B$ values for a select set of materials. Metglas 2605SA1 has a very low λ_s but an exceptionally high $\partial\lambda/\partial B$.

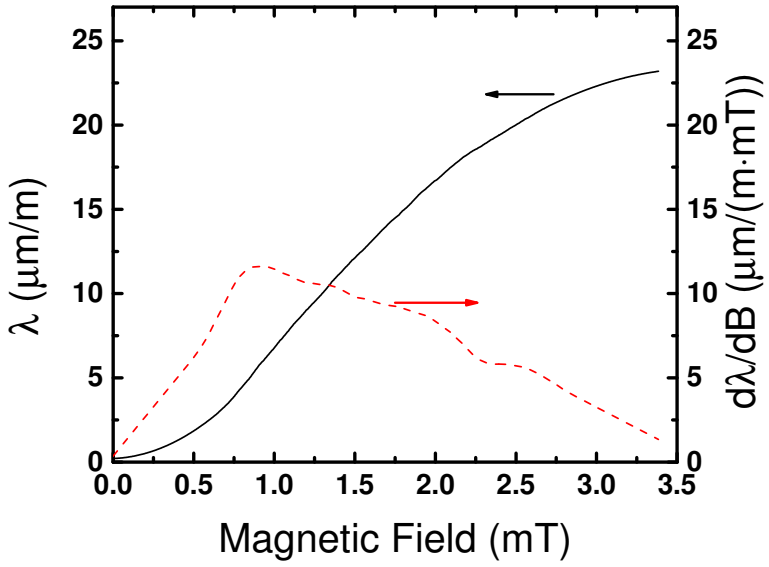

Figure 2.1. Typical non-linear magnetostriction response from Metglas 2605 SA1 measured from a 30 mm $\times$ 5 mm as-cast ribbon. λ saturates at approximately 23 μm/m. The right axis shows the magnetostriction coefficient $\partial\lambda/\partial B$ to be approximately 12 $\frac{\mu m}{m \cdot mT}$.

2.1.1.1 Magnetic Domain Alignment and Magnetostriction

Aligning the easy axis of a magnetostrictive film ensures that the domains produce the largest amount of magnetostriction (λ) in response to a magnetic field perpendicular to the easy axis. The illustration in Figure 2.2(a) shows randomly oriented magnetic domains in a magnetostrictive film after application of a saturation magnetic field to have a strain of λ_s. For a film where the domains are forced to rotate 90° in response to an applied saturation magnetic field, the maximum strain of λ_{max} is produced, as seen in Figure 2.2(b). The difference between the random and perpendicular alignment can be understood by (2.1), where θ_i and θ_f are the initial and final magnetization angles relative

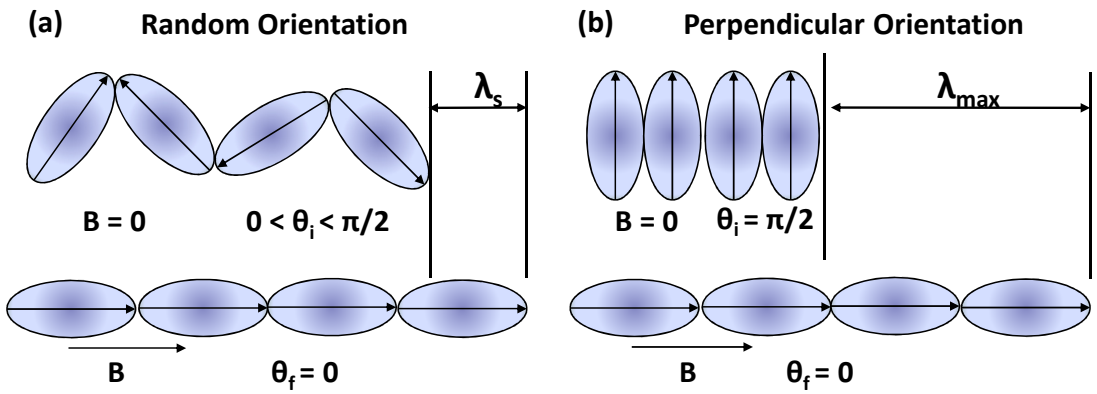

Figure 2.2. Illustration showing magnetic domains initially in (a) a random orientation and (b) perpendicular orientation before and after magnetic alignment, respectively. With random domain alignment, a strain of λ_s is possible. When the domains are aligned perpendicular to the applied magnetic field, B, a maximum amount of strain (λ_{max}) can be achieved.

to the applied magnetic field [90].

$$\lambda_{\max} = \frac{3}{2}\lambda_s \left(\cos^2\theta_f - \cos^2\theta_i\right) \tag{2.1}$$

λ_s is the saturation magnetostriction for isotropically (randomly) distributed magnetic domains. Assuming the easy axis is perfectly perpendicular to the applied field, (i.e., $\theta_i = \pi/2$ and $\theta_f = 0$), then $\lambda_{max} = \frac{3}{2}\lambda_s$; a maximum improvement of 50% in the magnetostriction is possible. The magnetoelectric coefficient (α_{me}) is defined in (2.2), where *V* is the measured voltage, *B* is the applied magnetic field and *t* is the electrode spacing on the piezoelectric. The magnetoelectric coefficient is equivalent to the product of the piezoelectric voltage coefficient $\left(\frac{\partial E}{\partial S}\right)$ and the magnetostrictive coefficient $\left(\frac{\partial \lambda}{\partial B}\right)$ as seen in (2.2), where *E* is the electric field and *S* is the strain.

$$\alpha_{me} = \frac{\Delta V}{t\ \Delta B} = \frac{\partial E}{\partial S}\frac{\partial \lambda}{\partial B} \tag{2.2}$$

2.2 Optimization of Magnetostriction in Metglas 2605SA1 Foils

2.2.1 Experimental Setup

2.2.1.1 Metglas Annealing

The 5 $\pm$ 0.5 mm $\times$ 30 $\pm$ 0.5 mm, 23 μm thick Metglas 2605SA1 ribbons are annealed on a custom built hotplate. The hotplate is built from non-ferromagnetic components to minimize unwanted magnetic fields during the anneals. The heater is an alumina metallic ceramic heating element held between two aluminum plates to ensure uniform heat distribution. Metglas 2605SA1 ribbons are cut and clamped onto the aluminum plates of the hotplate using a silicon piece and held down with aluminum clips. The cutting of the ribbons is done prior to annealing because Fe-Si-B amorphous alloys like Metglas 2605SA1 can undergo embrittlement from heat treatments, making it difficult to cut after annealing. A K-type thermocouple is also inserted between an aluminum clip and the silicon to monitor the temperature. A pair of SmCo high temperature magnets are placed approximately 25 mm apart, with the north-south poles facing each other on a glass fixture and secured with copper tape to provide a magnetization field along the short axis of the ribbons. The heater and magnets are placed on a thermally insulating ceramic slab. An air gap between the aluminum plates and the magnets ensures that the magnets do not exceed their maximum operating temperature of 300 °C. The Metglas placed in the center of the heater experiences approximately 160 $\pm$ 20 mT magnetic field, which was determined by a calibrated commercial magnetometer as seen in Figure 2.3 for annealing temperatures up to 400 °C after 30 minutes. The uncertainty in the magnetic field strength is due to the spatial variation of the magnetic field over the annealing area, again determined by a calibrated commercial magnetometer. The strength of the magnetic field was measured for anneals up to 400 °C and was found to be indistinguishable to its room temperature strength, within the uncertainty of the measurement. Thermocouples placed on the SmCo magnet show that the temperature of the magnet does not exceed, 230 °C during the 450 °C 30 minute anneal, well below it's 300 °C maximum operating temperature. The ribbons are allowed to cool until they reach 80 °C or lower before they are removed from the annealing setup and used in the fabrication of a magnetoelectric device, for SEMPA imaging, or for measuring magnetostriction.

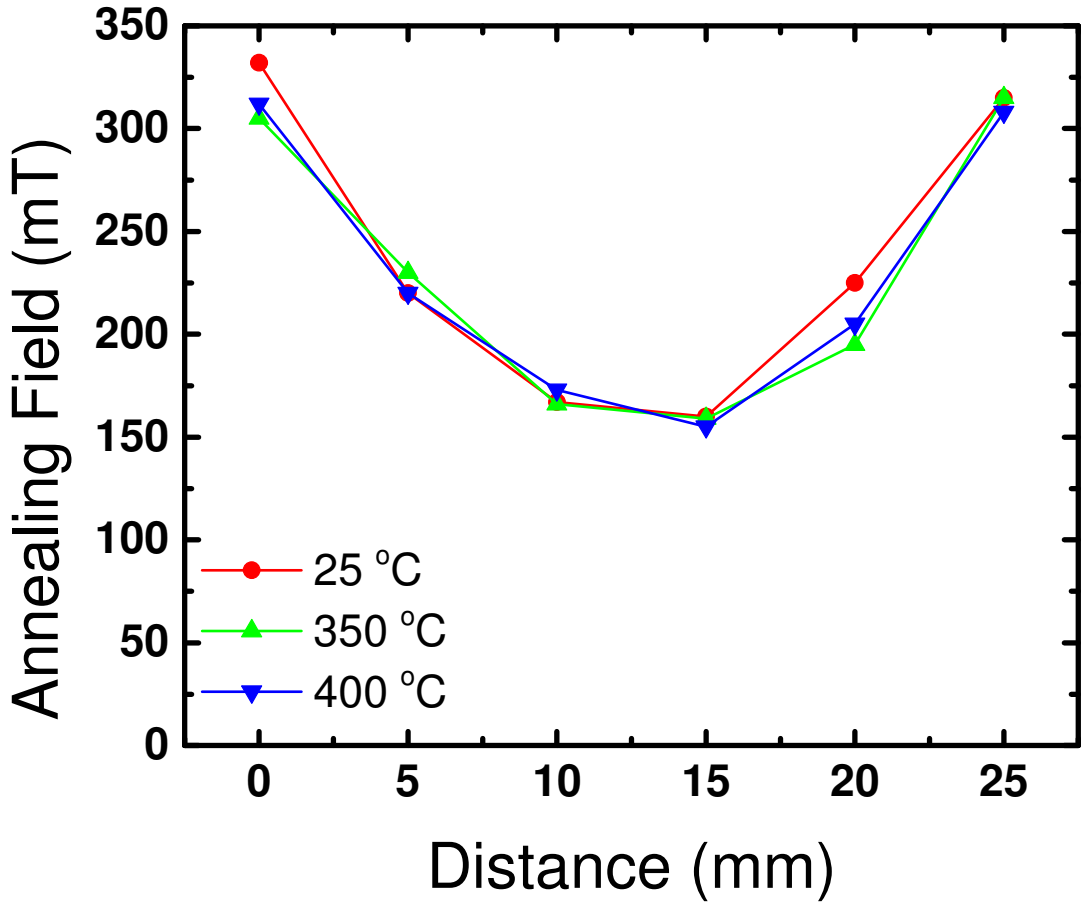

Figure 2.3. Distribution of the magnetic field across the width of the magnet holder. The annealing area is 17 mm and in the center, has an average magnetic field of approximately 160 $\pm$ 20 mT, with little variation observed up to 400 °C.

2.2.1.2 Magnetostriction

After annealing the Metglas ribbons are clamped at one end and the strain on the free edge is measured. The magnetostriction is measured using a 3-D laser Doppler vibrometer at the tip of the free end of the Metglas ribbon. A benefit of this method is that it eliminates the influence of a contact transducer like a strain gauge. Also, this system is capable of directly measuring in-plane motion so a unimorph structure is not required. A pair of Helmholtz coils, calibrated with a commercial magnetometer, are used to apply the magnetic field in a controlled manner. The measurement is repeated 4 times and smoothed to remove high frequency noise. The uncertainty of the saturation magnetostriction is reported as ± 1 σ (one standard deviation) determined from the repeats. A derivative with

respect to the applied magnetic field is performed to plot the magnetostrictive coefficient. The magnetostriction coefficients reported in this dissertation refer to the peak value. The uncertainty in magnetostriction coefficient is reported as $\pm 1\ \sigma$ (one standard deviation) from values calculated from the repeats.

2.2.1.3 SEMPA Imaging

SEMPA [91, 92] is used to image the magnetic domain structure of the Metglas ribbons at the surface and quantitatively assess the alignment of the domains induced by annealing. SEMPA is a scanning electron microscopy technique which images all three components of the magnetization vector of a ferromagnetic sample by determining the polarization direction of the secondary electrons for each pixel of a scan. Metglas samples measuring 5 ± 0.5 mm $\times$ 15 ± 0.5 mm are used for this experiment. After annealing, the ribbons are cleaned in situ with 1000 eV Ar ion etching immediately prior to SEMPA imaging. Five 254 μm $\times$ 254 μm SEMPA images of different regions are taken for each annealing condition in order to accurately determine the typical domain structure produced by each anneal. Only the shiny side (the rough side is the face in contact with the roller during the quenching process) of the Metglas ribbon is imaged.

2.2.1.4 Magnetoelectric Magnetic Sensing

To measure the magnetoelectric coefficient, laminate structures are fabricated using 3 mm $\times$ 13 mm $\times$ 200 μm thick PZT-5A and a pair of 5 ± 0.5 mm $\times$ 30 ± 0.5 mm, 23 μm thick Metglas 2605SA1 ribbons. The PZT has 15 μm thick silver on the top and bottom deposited by the manufacturer ("APC International" Pennsylvania, USA) and is electrically poled in the d_{31} orientation (also by the manufacturer), resulting in a d_{31} coefficient of -175 pm/V [93]. The final device structure is illustrated in figure 2.4(a). First, a pair of Metglas ribbons undergo various annealing treatments, then the ribbons are epoxied using EPO-TEK H20E conductive silver epoxy on the top and bottom of the PZT. The laminate is mechanically clamped to ensure a thin and uniform epoxy layer and is cured for at least 180 min at 90 °C. Simulations have shown that an epoxy with a modulus of 5-10 GPa applied as thinly as possible is crucial for optimal stress transfer between the laminates [94]. The exact reasoning and motivation for these fabrication decisions are discussed in detail later, in chapter 3. Next, a small 3 mm $\times$ 5 mm section of the bottom of the laminate is epoxied to a ceramic holder with a silver electrode trace,

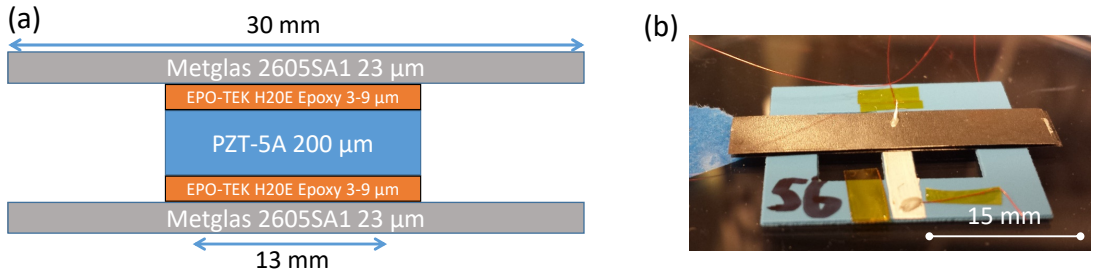

Figure 2.4. (a) Cross section of the device structure showing the 3 mm × 13 mm, 200 µm thick PZT-5A with 15 µm silver top and bottom electrodes. The 23 µm thick 5 mm × 30 mm Metglas ribbons are epoxied on the top and bottom by a conductive silver epoxy. (b) Camera image of the finished device.

and the trace is connected to a copper wire. The top of the laminate is also connected with a copper wire. Both wires are secured by H20E epoxy, and the assembly is cured again for at least 180 min at 90 °C. A camera image of the final device is shown in figure 2.4(b).

The devices are tested in a custom designed box with three layers of magnetic shielding. Two pairs of Helmholtz coils are used for DC and AC magnetic stimulation inside the shielded box (Figure 2.5). An AC current source is used to automatically adjust for impedance variations in the coil and provide a stable magnetic field strength across a range of frequencies. The voltage generated by the PZT is measured by a lock-in amplifier as seen in the illustration of the test setup in Figure 2.5. The peak magnetoelectric voltage coefficient is determined by applying a DC magnetic bias to the ME device in the steepest portion of the magnetostriction curve (peak magnetoelectric coefficient), which is typically 500 µT to 1500 µT, and consistent with observations from other groups [68, 77]. All magnetoelectric coefficient measurements are done with a 20 Hz sine signal at 5.6 µT.

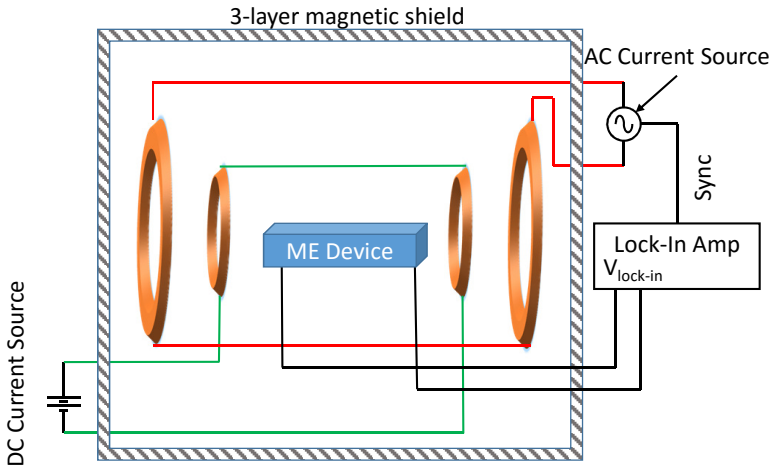

Figure 2.5. Diagram of the testing setup. A DC source and an AC current source are used for stimulation. The ME device is directly connected to a lock-in amplifier. For noise measurements, the lock-in is replaced with a digital spectrum analyzer.

2.3 Magnetic Alignment of Metglas 2605SA1 Foils by Annealing in a Magnetic Field

To study the impact of temperature on magnetostriction, the Metglas ribbons are annealed from 250 °C to 400 °C for 5 min in air without a magnetic field. The magnetostriction is measured by laser Doppler vibrometer, shown in Figure 2.6. The magnetostriction coefficient is calculated from the derivative of the magnetostriction, with respect to the magnetic field. Two grouping of curves are observed; Group 1 shows no trend with annealing temperature. Group 2 shows an increase in saturation magnetostriction and magnetostriction coefficient from $16.7 \pm 1.6 \frac{\mu m}{m \cdot mT}$ to $21.0 \pm 0.7 \frac{\mu m}{m \cdot mT}$. It is not clear why these two groups are observed. Some other variable, possibly as-quenched stress from the manufacturing process, is causing the samples to split into two groups of magnetostrictive curves.

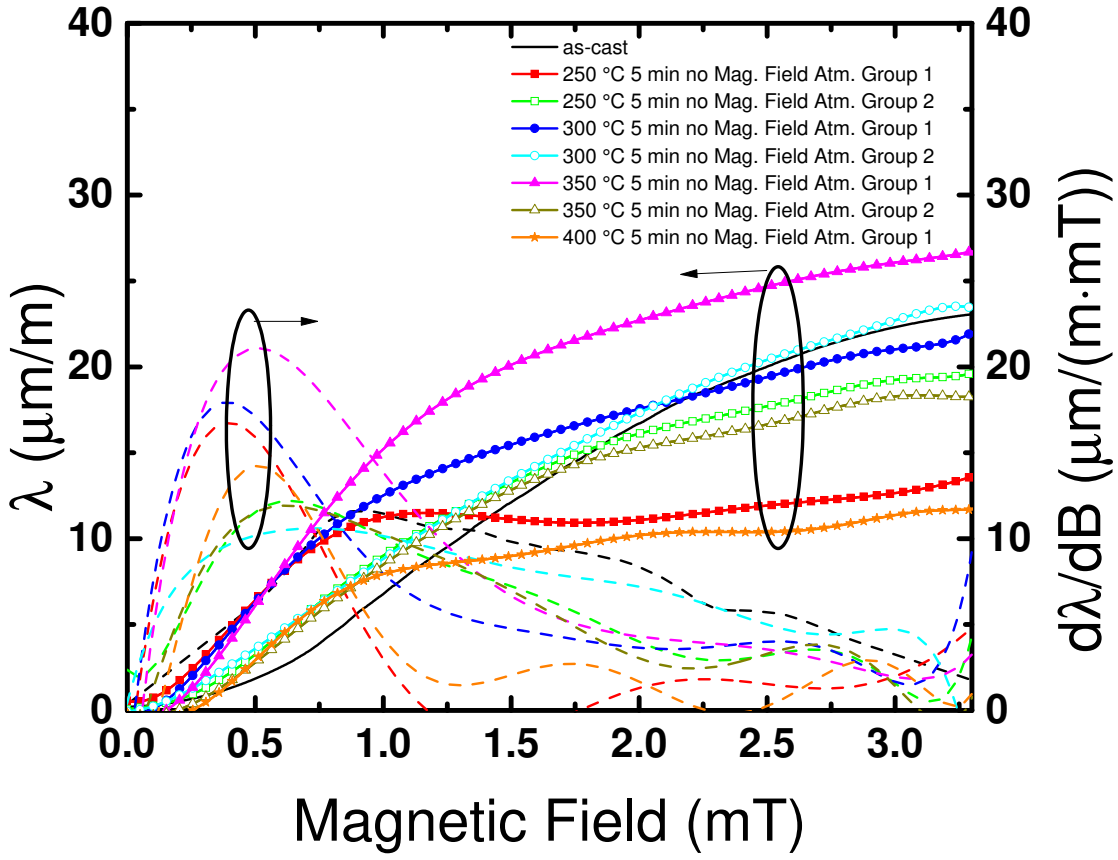

Figure 2.6. Magnetostriction and magnetostriction coefficient (dashed lines) for 5 min anneals without an applied magnetic field in air. Both λ and $\frac{d\lambda}{dB}$ are difficult to control without an external field present during annealing. Some other variable, possibly stress from the manufacturing process, is causing the samples to split into two groups of magnetostrictive curves.

Next the effect of annealing the samples in a 160 mT transverse (along the short axis of the ribbon) magnetic field is studied; The ribbons are again annealed from 250 °C to 400 °C in air. Figure 2.7 shows the knee of the magnetostriction curve increases with increasing annealing temperature. As a result, the magnetostriction coefficient increases with increasing annealing temperature from $11.6 \pm 0.4 \frac{\mu m}{m \cdot mT}$ for the as-cast sample to $77.5 \pm 2.2 \frac{\mu m}{m \cdot mT}$ for the 400 °C 5 min anneal in an applied magnetic field in air.

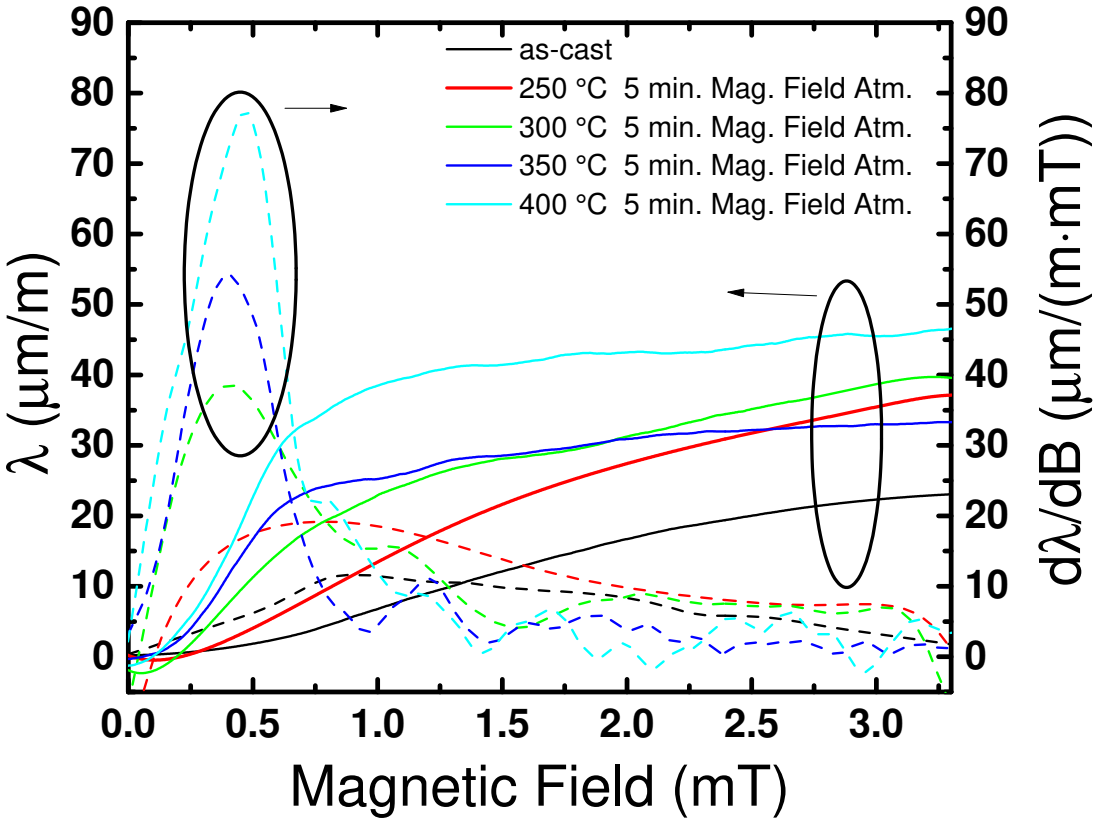

Figure 2.7. Magnetostriction and magnetostriction coefficient (dashed lines) for 5 min anneals with an applied magnetic field in air. The knee of the magnetostriction increases with increasing annealing temperature. The magnetostriction coefficient also increases with increasing annealing temperature.

To ensure that the dramatic magnetostriction coefficient increase observed in the Metglas annealed at 400 °C for 5 minutes in an applied magnetic field translates into a magnetoelectric coefficient improvement magnetoelectric devices are fabricate and tested. The average peak α_{me} measured for each annealing condition is shown in Figure 2.8. The average peak α_{me} is determined by sweeping positive and negative DC magnetic field where the uncertainty represents the entire range of measurements collected for each sample ($\pm$ half range). The worst case repeatability range is $\pm$ 0.05 MV/(m·T). The resulting error bars are too small to be seen in the plot.

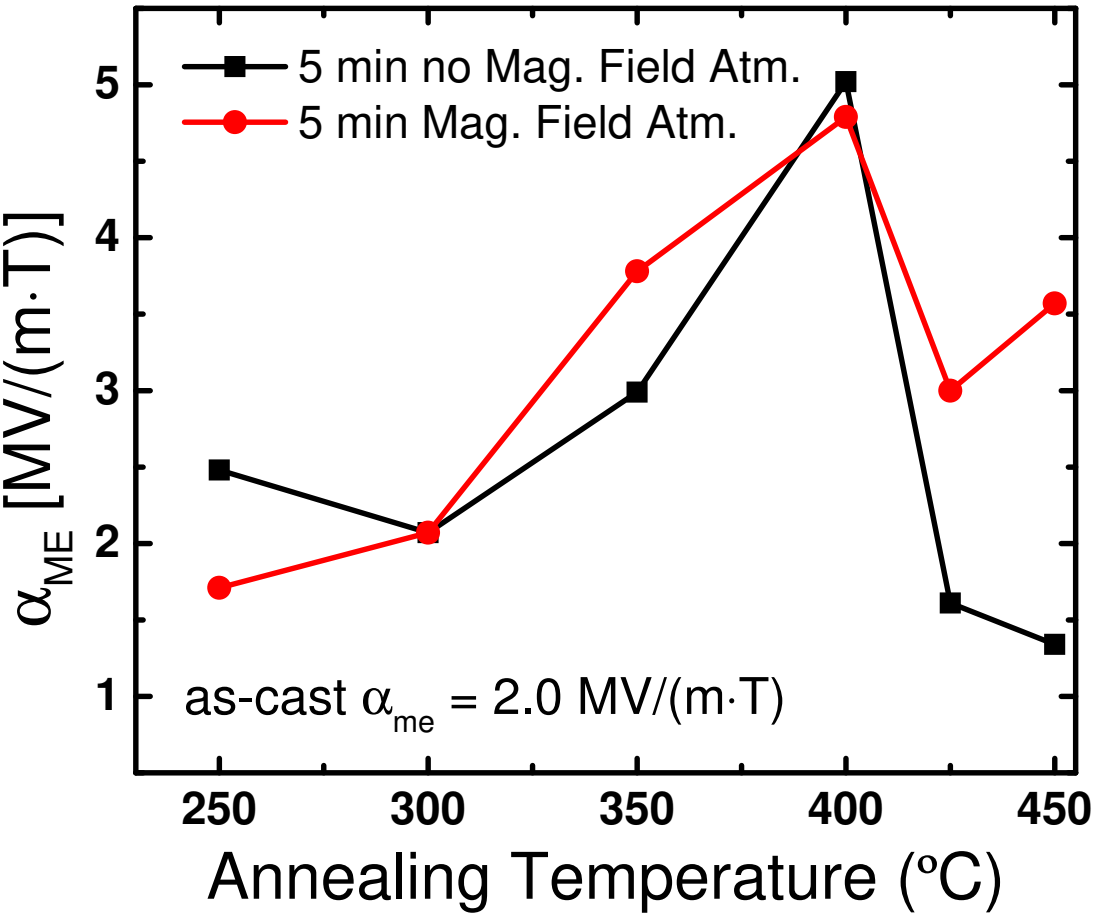

Figure 2.8. Magnetoelectric coefficient α_{me} vs. annealing temperature for samples annealed with and without an applied magnetic field. Up to 400 °C, the trends of the samples annealed with and without a magnetic field are similar. For both cases the magnetoelectric coefficient increases to approximately 5.0 ± 0.04 MV/(m·T). After 400 °C, the α_{me} decreases for both cases. Lines are added as a guide to the reader. The error bars described in the text are smaller than the point markers. Note that 1 V/(cm·Oe) $(\mu_0\mu_r)^{-1}$ = 1 MV/(m·T) for μ_r = 1.

The magnetoelectric coefficient increases with increasing annealing temperature up to 400 °C. However, the magnitude of improvement from as-cast to 400 °C is lower, 2.5-fold improvement in magnetoelectric coefficient versus 6.7-fold improvement the magnetostriction coefficient observed earlier in section 2.3. Surprisingly, the magnetoelectric devices fabricated using ribbons without an applied magnetic field during the anneal improved by approximately the same magnitude as samples made with ribbons that were annealed with a magnetic field. This suggests that annealing makes the domains

more susceptible to influence from the magnetoelectric fabrication process, possibly from compressive stress applied by the epoxy cure process.

To directly observe the domain alignment SEMPA imaging is done on Metglas ribbons annealed for 5 min from 250 °C to 400 °C in air with and without a magnetizing field. Figure 2.9 (a-e) shows the typical magnetic domains observed for Metglas strips in the as-cast state (a) and after 250 °C to 400 °C, 5 min annealing in a magnetic field along the x-axis (b-e). The histogram plot adjacent to each image shows the distribution of domain direction after mirroring about the y-axis. Figure 2.9 (a-c) shows that stress-induced striations are visible for the as-cast sample and for samples annealed up to 300 °C. These occur because out-of-plane magnetic domains induced by stress must rotate to in-plane domains at the surface and curl back into the sample [95]. At 350 °C and higher, the area of observed stress-induced striations is significantly reduced, which implies a reduction in out-of-plane domains, and correlates to an increase in the α_{me}.

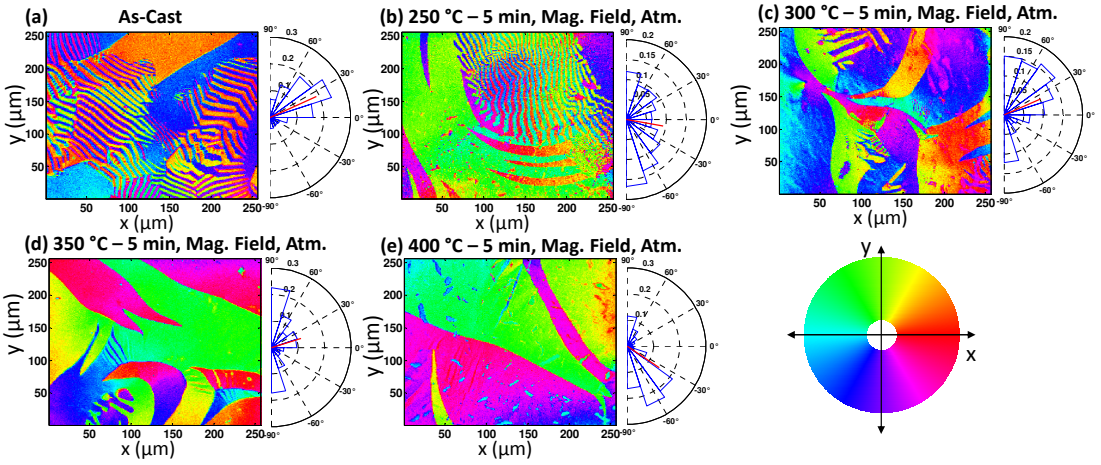

Figure 2.9. Typical 254 μm × 254 μm SEMPA images and angle histograms of as-cast samples (a), and samples annealed for 5 min in a 160 mT magnetic field. The magnetization direction is coded to the color wheel, with red indicating magnetization pointing in the +x direction, green indicating magnetization pointing in the +y direction, etc. Stress-induced striations are visible in as-cast, 250 °C and 300 °C annealed samples. For samples annealed at 350 °C and 400 °C the striations are rarely observed. The red bar in the polar histograms points to the average magnetization direction. There is no evidence of an induced easy-axis alignment. The angle distribution is not ideal for maximum magnetostriction.

Despite the dramatic improvement in saturation magnetostriction, and magnetostriction coefficient observed in Figure 2.7, the SEMPA images, seen in figures 2.9

(b-e), show the magnetic ordering did not align along the magnetizing field axis for any annealing condition. The magnetization of the Metglas ribbons annealed without the magnetizing field (not shown) had similar characteristics and did not show easy axis alignment. SEMPA is a surface imaging technique and can not capture alignment that is occurring in the bulk of the ribbon. The increase in saturation magnetostriction and magnetostriction coefficient when annealing in an applied magnetic field implies that the domains are aligning, and the lack of domain alignments observed by SEMPA suggests that further optimization may be possible.

To optimize the magnetostriction coefficient, by inducing further transverse magnetic alignment in the Metglas ribbons, the duration of anneals is increased. Magnetostriction data is collected for Metglas ribbons annealed between 350 °C and 450 °C for 30 minutes in various environments in an applied magnetic field. Oxygen is removed from the annealing environment to prevent oxidation of the Metglas by annealing in a vacuum chamber which is triple pump-purged with nitrogen and pumped to 1.33×10^4 Pa (100 Torr) or by annealing in a continuous N_2 purge. Figure 2.10 shows the that for every annealing temperature a higher saturation magnetostriction and magnetostriction coefficient are observed for anneals done in an oxygen-free environment. The highest saturation magnetostriction of 50.6 ± 0.2 $\mu m/m$ and magnetostriction coefficient of 79.3 ± 1.5 $\frac{\mu m}{m \cdot mT}$, respectively, were measured for the 400 °C 30 min anneal with an applied magnetic field in an N_2 environment. The saturation magnetostriction and magnetostriction coefficient decrease significantly for the 30 min 450 °C anneals and are exceptionally poor for the sample annealed in atmosphere.

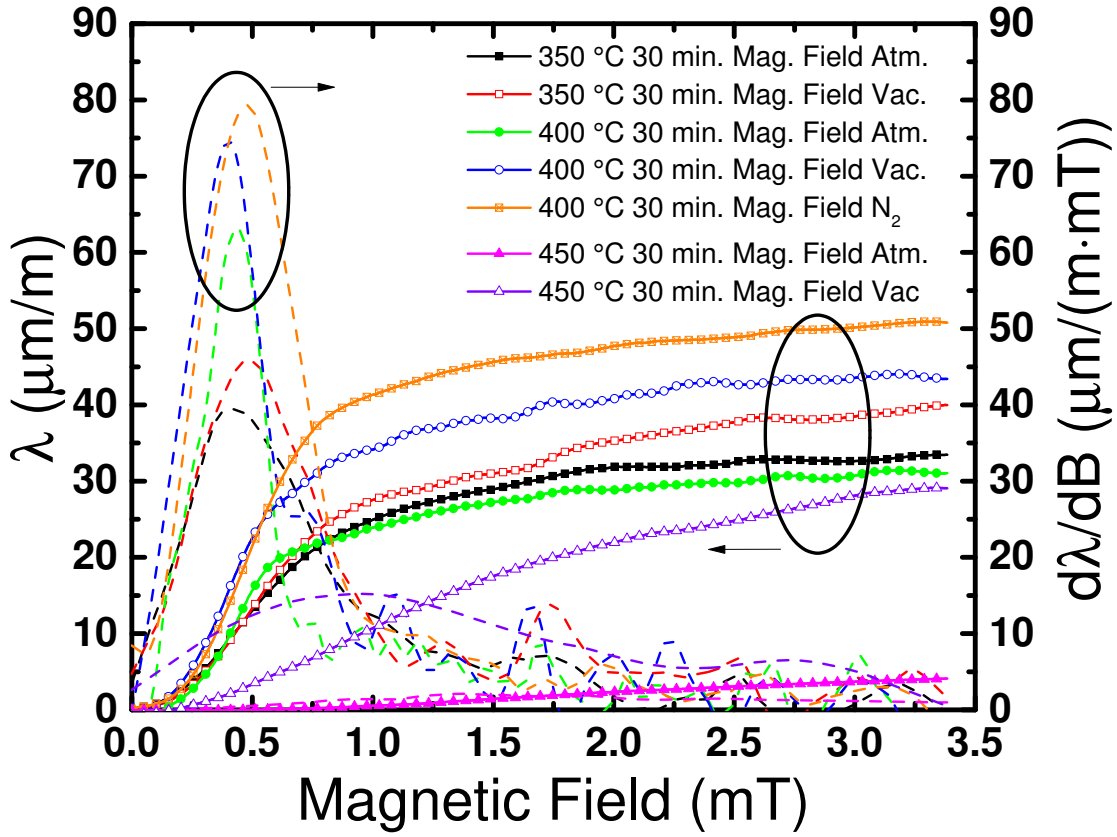

Figure 2.10. Magnetostriction and magnetostriction coefficient (dashed lines) for 30 min anneals with an applied magnetic field in varying environments. Both λ and $\frac{d\lambda}{dB}$ increase for anneals done in an oxygen-free environment for the same temperature. The optimized magnetostriction and magnetostriction coefficient are found to be 50.6 ± 0.2 $\mu m/m$ and 79.3 ± 1.5 $\frac{\mu m}{m \cdot mT}$, respectively, for the 400 °C 30 min anneal with an applied magnetic field in an N_2 environment.

Increasing the anneal time from 5 min to 30 min at 350 °C in air results in a linear decrease of the magnetoelectric coefficient from 3.8 ± 0.04 MV/(m·T) to 2.0 ± 0.03 MV/(m·T), as seen in Figure 2.11. Similarly, Figure 2.11 shows the α_{me} decreases from 5.0 ± 0.04 MV/(m·T) to 4.1 ± 0.05 MV/(m·T) when the anneal time is increased from 5 min to 30 min at 400 °C.

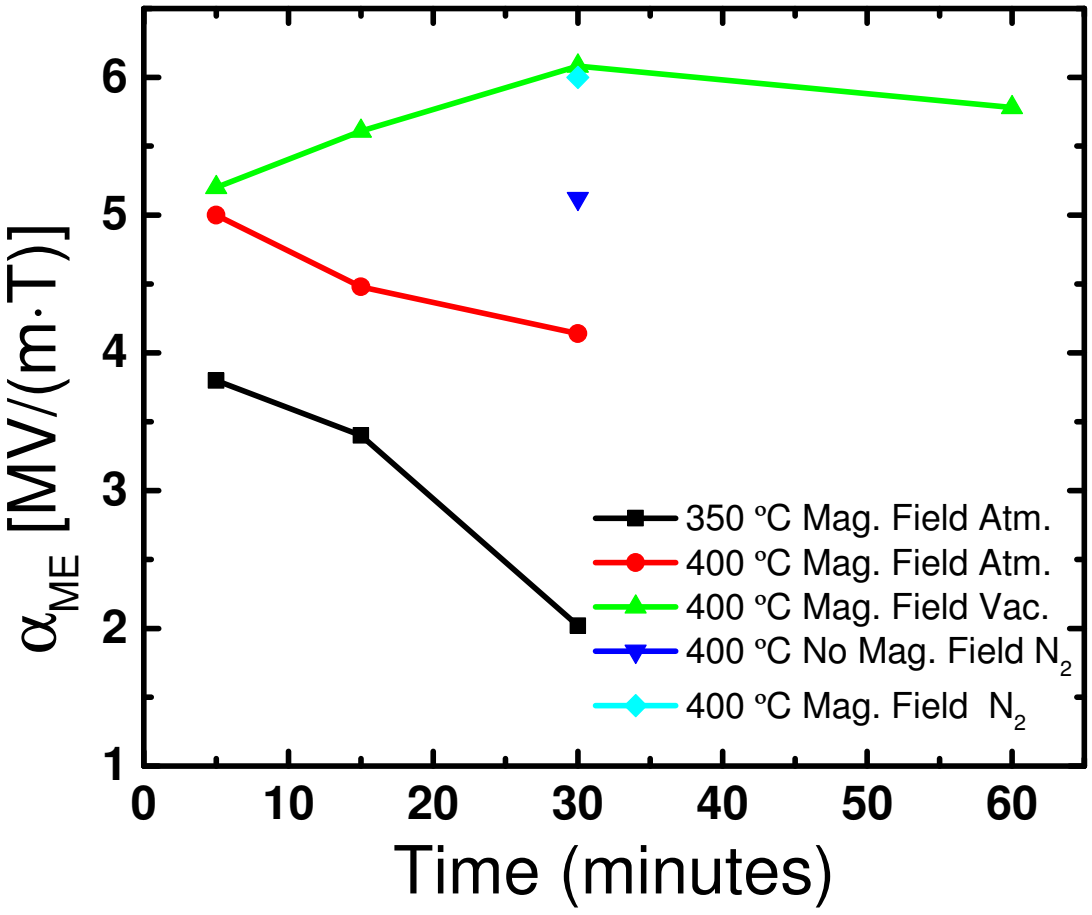

Figure 2.11. Increasing the anneal time from 5 min to 30 min decreases the magnetoelectric coefficient for 350 °C and 400 °C annealed samples in air with an applied magnetic field. However, annealing in vacuum resulted in a 1.2× improvement for a 400 °C 30 min anneal compared to a 5 min 400 °C anneal in atmosphere with an applied magnetic field. A 60 min 400 °C anneal in vacuum with an applied magnetic field did not result in further improvement, suggesting the magnetic domain alignment had saturated at 30 min. The α_{me} = 5.0 ± 0.04 MV/(m·T) for a sample annealed for 30 min at 400 °C in N_2 without an applied magnetic field is comparable to that measured for samples annealed for 5 min at 400 °C in atmosphere with and without an applied magnetic field. The α_{me} = 6.1 ± 0.03 MV/(m·T) measured for a 30 min 400 °C anneal in N_2 with an applied magnetic field is comparable to the 30 min 400 °C vacuum anneal with an applied magnetic field. This confirms oxygen plays a role in the α_{me} degradation for anneals longer than 5 min. The error bars are described in the text and are smaller than the point markers. Note that 1 V/(cm·Oe) $(\mu_0\mu_r)^{-1}$ = 1 MV/(m·T) for μ_r = 1.

The SEMPA image in Figure 2.12(a) shows that a 30 min 350 °C anneal in air does

not result in domain alignment on the surface. However, SEMPA images taken after a 30 min 400 °C anneal in air reveal a strong magnetic domain alignment in the x-axes, parallel to the magnetic field applied during the anneal as seen in Figure 2.12(b). SEMPA imaging of ribbons annealed for 30 min in vacuum in an applied magnetic field shows easy axis alignment along the magnetic field direction in Figure 2.12(c). To confirm that the domain alignment is in response to the applied magnetic field, SEMPA imaging is performed on a 30 min 400 °C vacuum sample annealed without a magnetic field. Figure 2.12(d) confirms that the domains do not align without magnetic field present during annealing. SEMPA imaging on 450 °C 30 min anneals in an applied magnetic field reveals a fine magnetic domain structure that is heavily influenced by crystallization on the surface. The 450 °C samples were clearly more polycrystalline when observed under traditional scanning electron microscopy imaging (not shown) compared to the all other samples. Visual inspection of Figure 2.12(e), the SEMPA image taken for the 450 °C 30 min anneal in an applied magnetic in vacuum, does show obvious signs of domain alignment however the histogram shows an alignment in the x-axis with a large Gaussian spread. The SEMPA image and histogram for the 450 °C 30 min anneal in an applied magnetic in air show no preferred alignment.

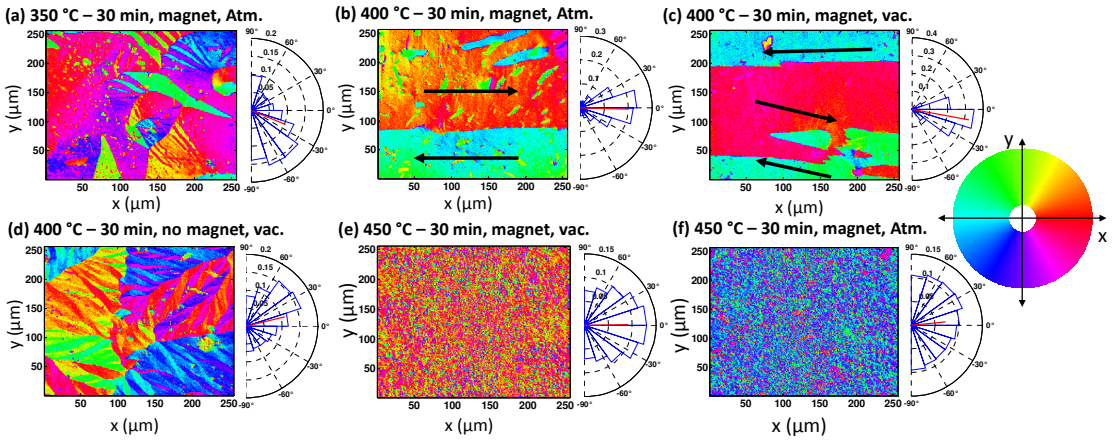

Figure 2.12. 254 μm × 254 μm typical SEMPA images and angle histograms. (a) Annealing at 350 °C with a magnetic field in atmosphere did not result in domain alignment on the surface. Samples annealed for 30 min at 400 °C in a magnetic field applied along the x-axis shows strong easy axis alignment for both the vacuum (b) and atmosphere (c) cases. Arrows are added to indicate to the approximate domain direction. As expected, annealing for 30 min at 400 °C in a vacuum without a magnetic field does not result in magnetic domain alignment (d). Annealing at 450 °C for 30 min in (e) vacuum results in fine magnetic domain structures with a weak alignment, but annealing in (f) air shows no preferred domain alignment axis.

To quantify the magnetic easy axis alignment, a figure of merit is developed. The average or standard deviation of the domain angle cannot be used as a useful figure of merit. The average cannot distinguish between a set of domains that are approximately mirrored about the x-axis and domains that are actually pointing in the x-axis. The standard deviation only describes the variation of the angles and not their direction. To capture both the variation and direction of the domain angle, the standard deviation equation is modified to be the standard deviation (σ_0) around 0 degrees (parallel to the magnetizing field), as shown in (2.3). N is the number of pixels in each image, ϕ_i is the magnetization direction of each pixel, and ϕ_m is the direction of the desired magnetization direction (0 degrees in this case). A smaller σ_0 value indicates a higher degree of alignment along the x-axis.

$$\sigma_0 = \sqrt{\frac{1}{N}\sum_{i=1}^{N}(\phi_i - \phi_m)^2} \tag{2.3}$$

Table 2.2 shows the average σ_0 for each annealing condition imaged by SEMPA. The

ribbons showing the best qualitative domain alignment in Figure 2.12 also showed the best quantitative alignment by having the lowest σ_0. The ribbons annealed in an applied magnetic field at 400 °C for 30 min in atmosphere and vacuum have a σ_0 = 37.9° and 42.2°, respectively. This is lower than the σ_0 determined for samples that did not show strong magnetic domain alignment, which were between 48.9° and 62.8°. Two notable exceptions were the as-cast, and 350 °C 5 min atmospheric zero-field-anneal samples. In the as-cast case, manufacturing induced stress may have contributed to a preferred domain direction. Also, it should be noted that SEMPA does not provide detailed information about the bulk domains magnetized out-of-plane, but there is observed evidence of closure domains in the as-cast sample. For the 350 °C, 5 min atmospheric zero-field-annealed case, one possible explanation is that the large domains that form at higher annealing temperatures make it more difficult to get a good representation of the domain variation in the sample within the field of view of the SEMPA images, resulting in a higher chance of observing outliers. It should also be noted that while the σ_0 appears to be high for aligned samples, it is not unexpected as significant moment canting has been observed in Fe-Si-B amorphous metallic glass with standard deviations of moment spread of 12° reported for an applied field of 0.5 T [96].

Table 2.2. σ_0 for every set of SEMPA images. The lowest σ_0 achieved from samples annealed for 30 min at 400 °C in an applied magnetic field in either vacuum or atmosphere. The as-cast sample σ_0 of 39.0° is low, possibly due to stress-induced alignment. The uncertainty is calculated as $\pm 1\sigma$ (one standard deviation) of the σ_0 calculated from the set of five images collected for each annealing condition.

Anneal Temp. (°C)	Time (min.)	Field (mT)	Environment	$\sigma_0(^\circ)$
as-cast	N/A	N/A	N/A	39.0 ± 15.7
250	5	0	Atm.	52.3 ± 5.6
300	5	0	Atm.	52.2 ± 7.5
350	5	0	Atm.	41.9 ± 4.3
400	5	0	Atm.	51.5 ± 7.0
250	5	160	Atm.	62.8 ± 5.7
300	5	160	Atm.	57.4 ± 7.4
350	5	160	Atm.	55.7 ± 9.0
400	5	160	Atm.	57.3 ± 12.3
350	30	160	Atm.	48.9 ± 8.4
400	30	160	Atm.	37.9 ± 5.7
400	30	160	Vac.	42.2 ± 4.8
400	30	0	Vac.	51.5 ± 3.1
450	30	160	Vac.	46.5 ± 1.0
450	30	160	Atm.	51.6 ± 0.3

The extent of oxidation in the Metglas is investigated. A thickness profile is conducted by X-ray photoelectron spectroscopy (XPS) on a series of samples annealed for 30 min and 60 min in N_2, vacuum, and atmosphere at 400 °C. No other elements besides Fe, Si, B, and O were observed. Figure 2.13 shows the atomic concentration of oxygen as a function of thickness. The oxide thickness, shown in Table 2.3, is taken to be the depth at which the O concentration falls to half its original value and has an uncertainty of $\pm$ 1 nm due to finite step size of the Ar etching. The samples annealed in atmosphere for 30 min and 60 min had the largest oxide layers of 6.7 nm and 7.6 nm, respectively. The 30 min and 60 min vacuum annealed samples had oxide thicknesses of 4.6 nm and 5.5 nm, respectively. In both cases, longer anneals resulted in a thicker oxide layer. The thinnest oxide (3.3 nm) resulted from a 60 min N_2 anneal and was comparable to the 3.9

nm oxide layer measured for the un-annealed as-cast sample. The oxide thicknesses are very thin compared to the Metglas foil thickness, and it is not clear if the oxide layer is impacting the magnetoelectric coefficient and by what mechanism. One possibility is that the formation of the oxide layer leads to stress and deformation-assisted crystallization which results in nanocrystallites forming, which has been observed in similar Fe-Si-B amorphous ribbons [97, 98]. Oxygen is known to significantly increase the rate of crystallization in this phenomenon [99].

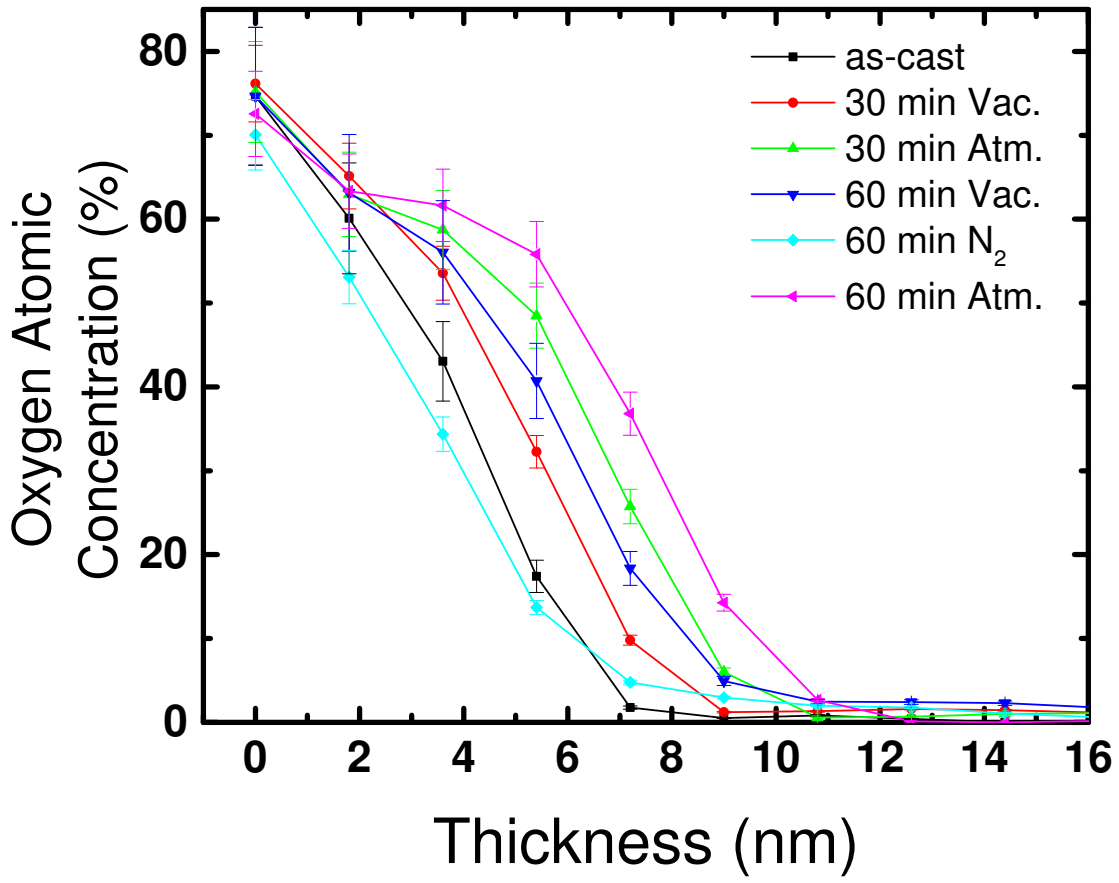

Figure 2.13. Thickness profile of oxygen atomic concentration for various 400 °C annealing conditions. Annealing in atmospheric conditions results in thicker oxides compared to vacuum or N_2 anneals. The uncertainty is determined by measuring the percent standard deviation of the boron atomic concentration below the oxide layer (which should be constant) for each sample and applying the percent standard deviation to each data point of oxygen concentration.

Table 2.3. Oxide thickness profile derived from XPS data. The oxide thickness has an uncertainty of $\pm$ 1 nm due to the finite step size of the Ar etching.

Anneal Time (min)	Environment	Oxide Thickness (nm)
0 (as-cast)	N/A	3.9
30	Atm.	6.7
60	Atm.	7.6
30	Vac.	4.6
60	Vac.	5.5
60	N_2	3.3

2.4 Optimization of Magnetostriction in Metglas Sputtered Thin Films

In this section the optimization of Metglas sputtered thin films is investigated. The optimized thin film is later used in a passively-powered wireless micromachined quartz magnetometer in chapter 5. Sputtered Metglas has been used for MEMS magnetoelectric magnetometers [100], micro-actuation [101] and biosensors [102]. In this section the effect of in-situ magnetization during deposition and the effect of thickness is investigated.

2.4.1 Experimental Setup

A semi-custom sputtering chamber is used to sputter Metglas 2605SA1 onto thin glass substrates. The Metglas target is prepared by cutting a 25 mm diameter disk of Metglas from the source ribbon and epoxying it to a target holder with thermally conductive epoxy, EPOTEK H20E epoxy. The epoxy is cured for 15 minutes at 150 °C, then allowed to slowly cool before being inserted into the sputter chamber, which is shown in the camera image in figure 2.14(a). Each target can sputter approximately 350 nm before a hole develops in the Metglas. To ensure this does not happen each target is only used to sputter 250 nm of film. The sputter chamber hold up to 4 targets, including Ti and Au meaning up to 500 nm of Metglas can be sputtered. Starting with a 70 μm thick borosilicate substrate 20 nm of Ti is first sputtered as a stiction later, next the Metglas is sputtered between 100 nm to 500 nm in thickness. Finally a thin 20 nm thick layer of Au is deposited to prevent corrosion. The final device cross section is illustrated in figure

2.14(b). The device dimensions are 5 mm x 20 mm as illustrated in 2.14(c). For some devices, a 50 mT magnetic field oriented along the short axis of the cantilever is applied using permanent magnets during deposition. The deposition parameters are detailed in table 2.4.

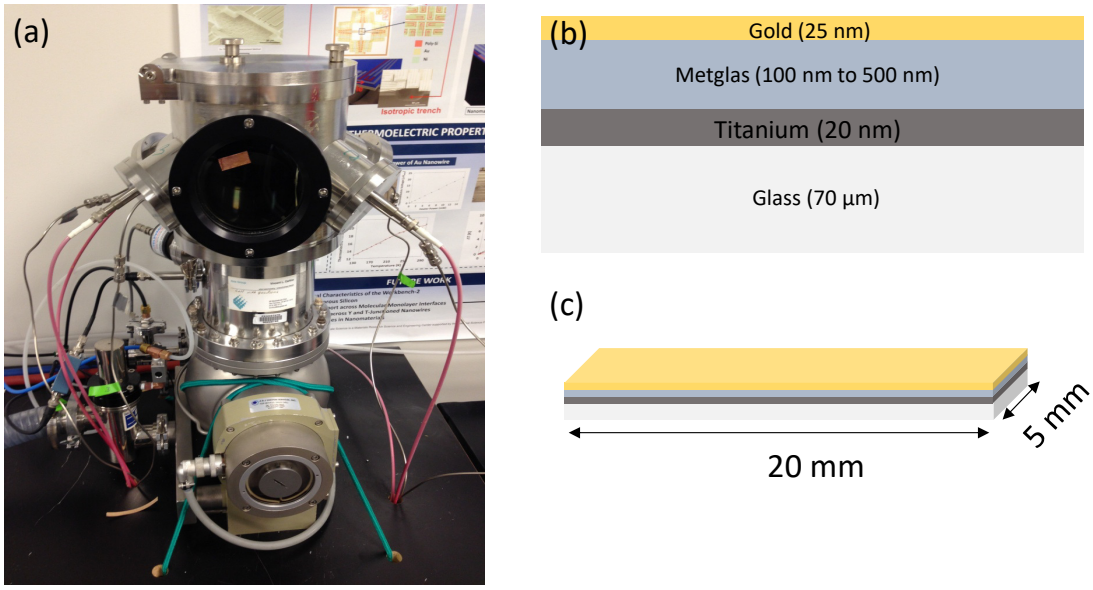

Figure 2.14. (a) Camera image of the semi-custom sputtering system used to sputter the Metglas 2605SA1. (b) Top-view schematic of the test devices with a 20 nm thick Ti stiction layer on 70 µ thick borosilicate glass, followed by 100 nm to 500 nm of magnetostrictive Metglas and finally a thin 20 nm thick layer of Au on top to prevent corrosion. (c) Isotropic schematic of the test devices which are 5 mm x 20 mm.

Table 2.4. Sputtering parameters for Metglas sputtering. Pressure, voltage, current and deposition are listed.

Parameter [units]	Value
Pressure [µTorr]	30-40
Gun Voltage [kV]	5.2
Gun Current [mA]	1.8
Deposition Rate [nm/min]	0.5

The sample is then carefully clamped between glass slides at one end and placed between two calibrated Helmholtz coils. The entire setup is surrounded by acoustic

absorbers and a polytec OFV-534 vibrometer sensor head measures the tip deflection of the cantilever in response to an applied field as seen in the camera images in figure 2.15(a-b).

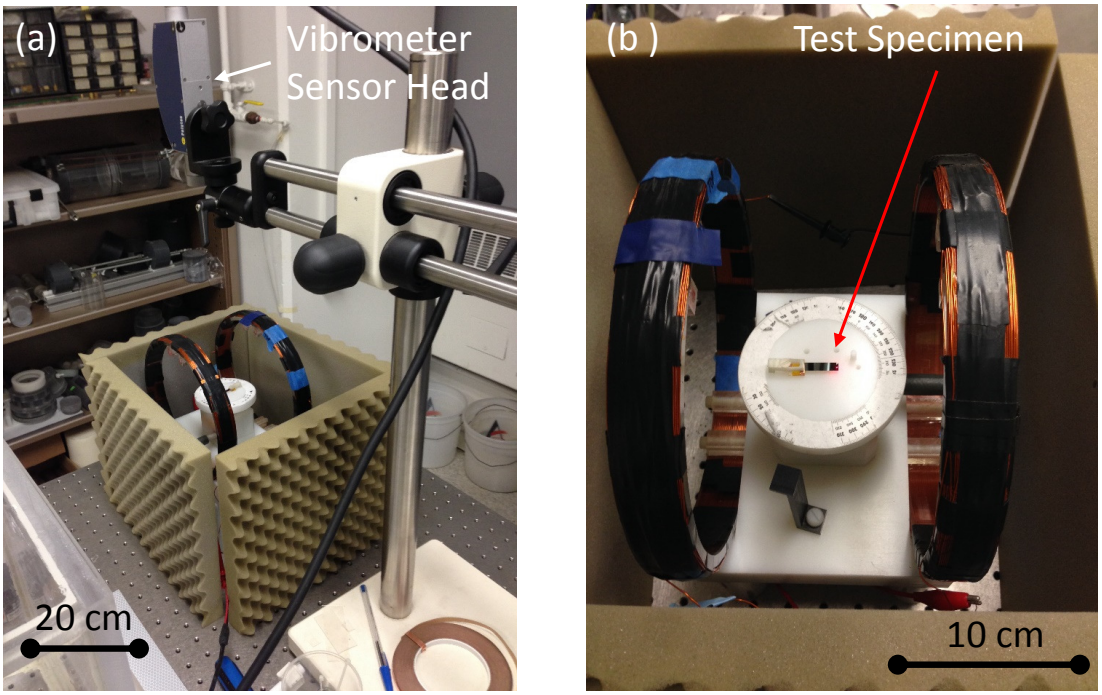

Figure 2.15. (a) Camera image of the test setup with a pair of Helmholtz coils to magnetize the Metglas using DC current source. Acoustic absorbers are placed around the setup to reduce noise. The vibrometer sensor head seen at the top of the image records the Z-deflection. (b) Another camera image showing the sample clamped at one end and a laser on the tip to measure the deflection.

2.4.2 Magnetostriction of Sputtered Metglas Thin films

The deflection (Z) measured by the vibrometer is related to the magnetostriction (λ) by Devoe's equation (2.4)[103],

$$Z = \frac{3\lambda E_m E_s t_m t_s (t_m + t_s) L^2}{E_m^2 t_m^4 + E_s^2 t_s^4 + 4E_m E_s t_m t_s (t_m^2 + t_s^2) + 6E_m E_s t_m^2 t_s^2} \tag{2.4}$$

where m and s subscripts refer to the magnetostrictive layer and the substrate, respectively. E is the elastic modulus, t is the thickness, L is the length of the cantilever.

To test the effect of magnetic poling a 500 nm thick Metglas layer is deposited with

and without a 50 mT magnetic field oriented along the short axis of the cantilever. The magnetostriction for the poled sample and the non-poled sample saturate at about the same value of 12.5 μm/m as seen in figure 2.16(a) but the poled sample has a steeper slope in the linear region and has a higher ($\partial\lambda/\partial$B) of 31.0 $\frac{\mu m}{m \cdot mT}$ versus 18.1 $\frac{\mu m}{m \cdot mT}$ for the not-poled 500 nm Metglas as shown in figure 2.16(b).

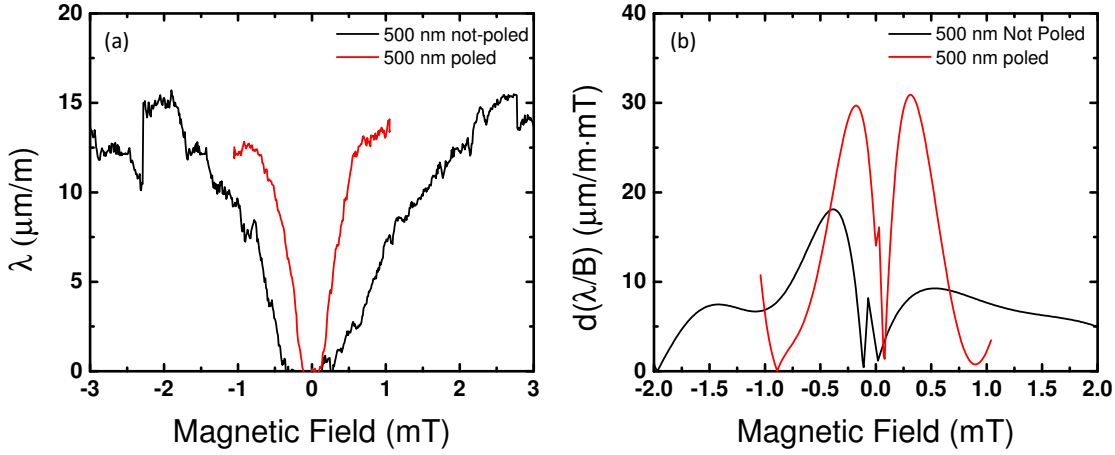

Figure 2.16. (a) Magnetostriction for a poled and unpoled 500 nm thick sputtered Metglas thin film. Both samples have similar saturation magnetostriction, but the poled sample has a steeper linear region. (b) The magnetostriction coefficient ($\partial\lambda/\partial$B) for the poled and non-poled 500 nm thick sputtered Metglas shows a 31.0 $\frac{\mu m}{m \cdot mT}$ for the poled sample versus 18.1 $\frac{\mu m}{m \cdot mT}$ for the not-poled sample.

The effect of thickness on the sputtered Metglas film is explored by varying the Metglas thickness 100 nm, 300 nm and 500 nm. Figure 2.17(a) shows the magnetostriction for the varying thicknesses and it is clear that the 500 nm film has a much sharper magnetostriction curve compared to the 100 nm and 300 nm films. This increased steepness of the 500 nm film results in a much larger magnetostriction coefficient of 31.0 $\frac{\mu m}{m \cdot mT}$ versus approximately 7.5 $\frac{\mu m}{m \cdot mT}$ for the 100 nm and 300 nm films as seen in Figure (b).

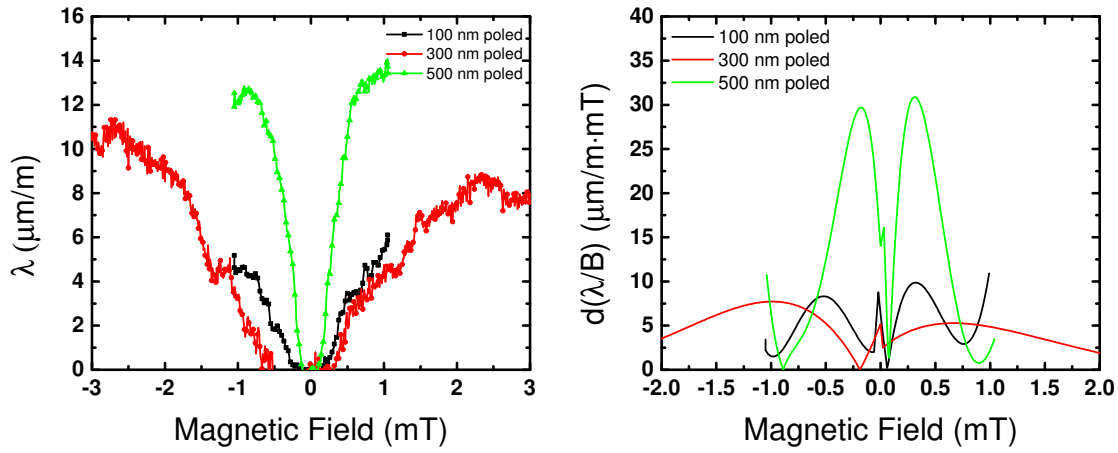

Figure 2.17. (a) Magnetostriction for 100 nm, 300 nm, and 500 nm Metglas films. The 100 nm and 300 nm films have a similar response but the 500 nm film is significantly steeper. (b) The magnetostriction coefficient reflects this steepness with a much larger coefficient of 31.0 $\frac{\mu m}{m \cdot mT}$ versus approximately 7.5 $\frac{\mu m}{m \cdot mT}$ for the 100 nm and 300 nm films.

The B-H loop of a 500 nm thick poled and not-poled sputtered Metglas is collected to see the impact in situ magnetic poling has on the permeability. The permeability directly influences the flux concentration and ultimately the sensing capability of the device. As seen in figure 2.18 the saturation magnetization is comparable for both conditions, but the poled sample has a much higher μ_r of 4300 v. 165 for the not-poled sample.

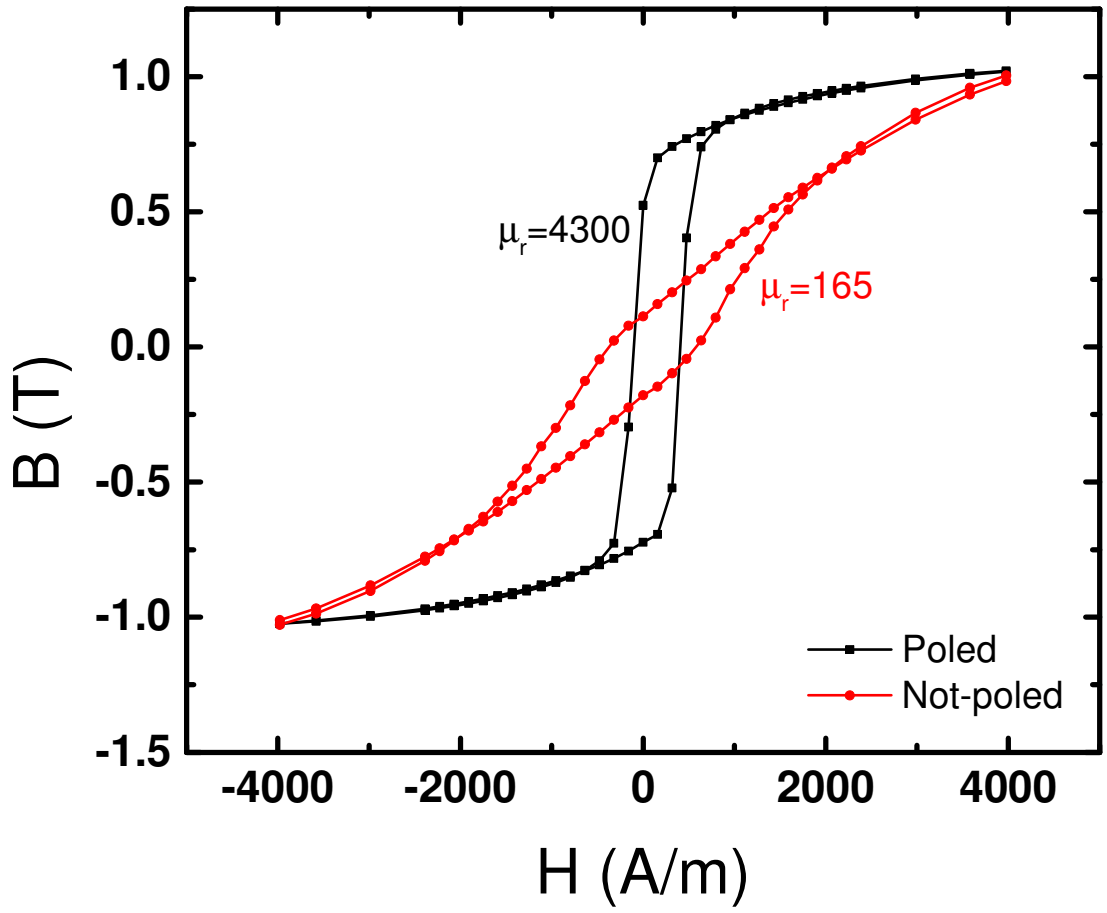

Figure 2.18. B-H loop of 500 nm poled and not-poled sample

2.5 Conclusion

As stated earlier, in the introduction, there have been many publications regarding annealing of magnetostrictive metallic glasses and how it impacts magnetostriction, ΔE effect, and embrittlement. However, there are virtually no reports on the effect of annealing on the magnetostriction coefficient. Some authors publish their magnetostrictive curves in response to annealing treatments, however there are usually not enough data points to accurately determine the slope and calculate the magnetostriction coefficient [104, 105].

To complicate matters, there are not only many compositions of metallic glasses, but several commercial entities that fabricate them. The process of making fabricating the metallic glasses is arguably as important as the composition because of the ultra-fast cooling process used to maintain an amorphous state is critical for good magnetostrictive

performance.

A select set of publications concerning magnetostrictive metallic glass is summarized in table 2.5. Early work in the 70's and 80's has shown that magnetostriction improves when annealing out as-cast stress and aligning the magnetic domains with a transverse magnetic field [106, 90, 75], however these works did not report on the magnetostriction coefficient. It should also be noted that ideal conditions for stress relief and magnetic domain alignment depend on the material composition, so any conclusion in regards to annealing treatments on one material does not necessarily carry over into to another material. Later work involving magnetoelectric devices [107, 48, 108], used commercially available films with no end-user annealing reported the magnetostriction coefficients of 22 $\left(\frac{\mu m}{m \cdot mT}\right)$ to 50 $\left(\frac{\mu m}{m \cdot mT}\right)$. Yang et al. annealed Metglas 2605SA1 at 350 °C with no magnetic field and showed an improvement in the magnetoelectric coefficient, but did not attempt transverse magnetic field annealing and did not explore other annealing ambients besides air [77]. Furthermore, they did not directly measure the magnetostriction and magnetostriction coefficient.

The major contribution of the work presented in this chapter is a comprehensive assessment of how to anneal and align magnetic domains in Metglas 2605SA1 to maximize the magnetostriction coefficient and in turn optimize the magnetoelectric coefficient and the sensitivity of magnetoelectric magnetometers. The resulting optimized magnetostriction coefficient of 79.3 $\frac{\mu m}{m \cdot mT}$ is, to the best knowledge of the author, the highest reported value for any material to date.

Table 2.5. Select works on magnetostriction and magnetostriction coefficient of amorphous metallic glasses. Several articles described improvements in magnetostriction due to annealing and aligning magnetic domains for maximum strain. Some of the highest magnetostriction coefficients reported to date have been from reports where authors used amorphous metallic glasses for magnetoelectric applications showing 22 $\frac{\mu m}{m \cdot mT}$ to 50 $\frac{\mu m}{m \cdot mT}$. The optimized annealing process in this chapter yielded an unprecedented 79.3 $\frac{\mu m}{m \cdot mT}$. N/R = not reported.

Year	Material	Dimensions	λ_{max} ($\mu m/m$)	$\partial\lambda/\partial B$ $\left(\frac{\mu m}{m \cdot mT}\right)$	Anneal Condition	Measurement Method	Ref.
1975	$Fe_{80}P_{13}C_7$	15 mm × 0.6 mm × 25 μm	62	N/R	N/R	3 capacitance method [109]	[105]
1979	$Fe_{80}B_{20}$	120 mm × 1 mm × 20 um	39	N/R	250 °C 1 hr, no mag field in vacuum	Small angle magnetization rotation	[106]
1984	Metglas 2605S2	7.5 mm × 25 mm × 25 μm	40	N/R	400 °C, 2 hr 0.1 mT transverse anneal	Piezoelectric Transducer	[90]
1986	Metglas 2605S2	25 mm × 13 mm × 25 μm	35	N/R	400 °C, 1 hr 120 mT transverse anneal	Bulk-optic Michelson interferometer	[75]
2006	FeBSiC (Metglas)	100 mm × 7 mm × 25 μm		40	none	Strain gauge	[107]
2011	Metglas	80 mm × 10 mm × 25 μm	34	22	none	Strain gauge	[48]
2013	Metglas	100 mm × 10 mm × 20 μm	N/R	50	none	N/R	[108]
2017	Metglas 2605SA1	30 mm × 5 mm × 25 μm	51	79	400 °C 30 min, 120 mT mag field in vacuum	Laser Doppler vibrometer	This work

Easy axis alignment and stress relief in Metglas 2605SA1 ribbons is produced

by annealing at 400 °C in an applied magnetic field of 160 mT, in a vacuum or N_2 environment. An improvement the magnetoelectric performance by more than a factor of 3 relative to untreated ribbons resulting in a magnetoelectric coefficient of 6.1 MV/(m·T) is shown. An optimal magnetostriction of 50.6 $\mu m/m$ and magnetoelectric coefficient of 79.3 $\frac{\mu m}{m \cdot mT}$ were measured. It is shown that the presence of oxygen degrades samples annealed in air, so an inert or vacuum annealing environment is necessary for achieving the optimal magnetoelectric performance in Metglas 2605SA1 based magnetoelectric sensors. Using a laser vibrometer the direct measurement of magnetostriction in Metglas films treated from 250 °C to 450 °C and in various environments with an without an applied magnetic field during annealing is shown. SEMPA imaging of domain alignments under various anneals and in various environments is used to confirm the domain rotation.

The magnetostriction coefficient is also investigated in sputtered Metglas thin films. In situ poling of the Metglas with a 50 mT magnetic field during deposition resulted in an improved permeability and magnetostriction coefficient. A 500 nm thick Metglas film in situ magnetized had a permeability of 4300 vs. 165 for a no-poled sample. The magnetostriction coefficient increased from 18.1 $\frac{\mu m}{m \cdot mT}$ for the not-poled sample to 31.0 $\frac{\mu m}{m \cdot mT}$ for the poled sample. The magnetostriction coefficient increased from 7.5 $\frac{\mu m}{m \cdot mT}$ for the 100 nm and 300 nm films to 31.0 $\frac{\mu m}{m \cdot mT}$ for the 500 nm film.

Chapter 3

PZT/Metglas 2605SA1 Transverse Magnetoelectric Magnetometer

3.1 Introduction

The three components of a magnetoelectric laminate are the piezoelectric, magnetostrictive, and epoxy phases. The magnetoelectric effect has been used extensively in the design of room temperature magnetic sensors [48, 110]. The effect is highest in laminate structures compared to composites [62, 61]. The magnetoelectric coefficient for laminates can be expressed as (3.1)

$$\alpha_{ME} = \frac{\Delta E}{\Delta B}k = \frac{\Delta E}{\Delta S}\frac{\Delta S}{\Delta B}k \tag{3.1}$$

where E is the electric field, S is the stress, and B is the magnetic field. The piezoelectric component $\Delta E/\Delta S$ is dependent on the piezoelectric coefficient and the elastic compliance of the piezoelectric phase. The magnetostrictive (sometimes called piezomagenetic) component $\Delta S/\Delta B$ is dependent on the magnetostrictive coefficient and the stiffness. K is the epoxy coupling coefficient which varies from 0 to 1.

The previous chapter optimized the magnetostriction coefficient due to magnetic domain alignment. The Metglas dimensions also play an important role. Zhao Fang showed that magnetic flux concentration is occurring in high permeability (μ_r) magnetoelectric laminates leading to improved magnetoelectric coefficients for long and narrow devices [50].

The force coupling between the magnetostrictive and piezoelectric phases is critical

in transferring the mechanical stress energy, Liu et al. [111] and others [112] showed that laminates with thinner epoxies and larger epoxy elastic stiffness increased the magnetoelectric coefficient. The findings are in agreement with Nan et al. who further showed that imperfections in the bonding layer reduce the coupling and the magnetoelectric coefficient [113].

Commercially available PZT is well optimized and shows a large d_{31} coefficient. However, the d_{31} coefficient can be temporarily increased by applying a DC electric field during the sensing operating. The next chapter explores using a PMN-PT piezoelectric to further improve the magnetoelectric response.

This chapter explores the consolidation and impact of optimized epoxy application, Metglas domain alignmnet, magnetic flux concentration and DC electric field biasing of the PZT to achieve an optimized magnetoelectric laminate. First a detailed introduction of the piezoelectric effect and it's atomic scale origins is introduced. A similar analysis was done earlier for magnetostriction in section 2.1.1. Next, analytical models coupling the magnetostriction and piezoelectric effect as a magnetoelectric phenomenon are derived. In the experimental section, a mechanical clamp method is studied to achieve a thin and non-porous bond layer between the magnetostrictive and piezoelectric laminate phases. Furthermore, COMSOL is used to determine the optimal thickness and Young's modulus of the epoxy layer. The flux concentration effects of the magnetoelectric width, length and thickness are investigated by 2D and 3D COMSOL models and experimentally verified. Metglas domain alignment, studied earlier, is also included in the final optimized device. Finally, a DC electric field is used to bias the piezoelectric and temporarily increase the d_{31} coefficient. Finally, the new limit of detection achievable from the addition of each optimization is compared.

3.2 Magnetoelectric Phenomenon

3.2.1 Piezoelectric Effect

The piezoelectric effect was first demonstrated in 1880 by the Curie brothers Jacques and Pierre. By studying crystal symmetry they were able to predict piezoelectric crystal classes and experimentally observed electric charge generation in a number of natural crystals including quartz, tourmaline, and topaz in response to stress [114, 115]. The brothers later demonstrated the converse piezoelectric effect, where an expansion and

contraction is produced due to an applied field, and showed that the direct and converse effect were equal in magnitude as predicted by Lippmann [116, 114].

Some piezoelectric materials belong to a class of materials called ferroelectrics, meaning the material can maintain a local charge separation (electric dipole). Piezoelectricity can only be observed in dielectric materials and in certain crystal structures. In polycrystalline piezoelectrics the effect is produced by aligning the ferroelectric domains. Piezoelectrics require a non-centrosymmentric crystal point group. Of the 32 possible crystal point groups 21 are non-centrosymmetric and 20 ((432) being exception) are piezoelectric. Centrosymmetric crystals can not produce an electric dipole in response to stress because their "charge centers of mass" move in unison. Figure 3.1(a) shows an illustration of cubic centrosymmetric crystal where both the negative and positive charge centers are in the center in the unstrained state. A uniaxial force is applied and the crystal compresses in figure 3.1(b), however the negative and positive charge centers have not separated and are both in the center so no polarization is developed. Figure 3.1(c) shows non-centrosymmetric example under no applied force and has both positive and negative charge centers overlapping, resulting in no polarization. However, with an applied force the center of charges will not overlap and a polarization will develop as seen in figure 3.1(d).

Piezoelectric materials are mathematically described by a set of equations relating the applied electric to an induced strain (3.2) and the converse effect relating an applied strain (3.3) to an induced electric field,

$$S = s^E T + d_t E \tag{3.2}$$

where *S* is the strain (unitless ratio), *s* is the elastic compliance (m^2/N), *E* is the electric field (V/m), *T* is the stress (N/m^2) and *d* is the piezoelectric strain constant (m/V).

$$E = \beta D - hS \tag{3.3}$$

where β is the dielectric impermeability (m/F), *D* is the electric displacement (C/m^2), *h* is the piezoelectric stress constant (V/m). $h = gc^D$, where c^D is the elastic stiffness (N/m^2) and g is the piezoelectric voltage constant (Vm/N). Quantities with superscripts means that the quantity is measured while the physical variable described by the superscript is held constant. The subscript *t* implies that the matrix is transposed (rows/columns interchanged). It should be noted that a number of other equations equivalent relationships

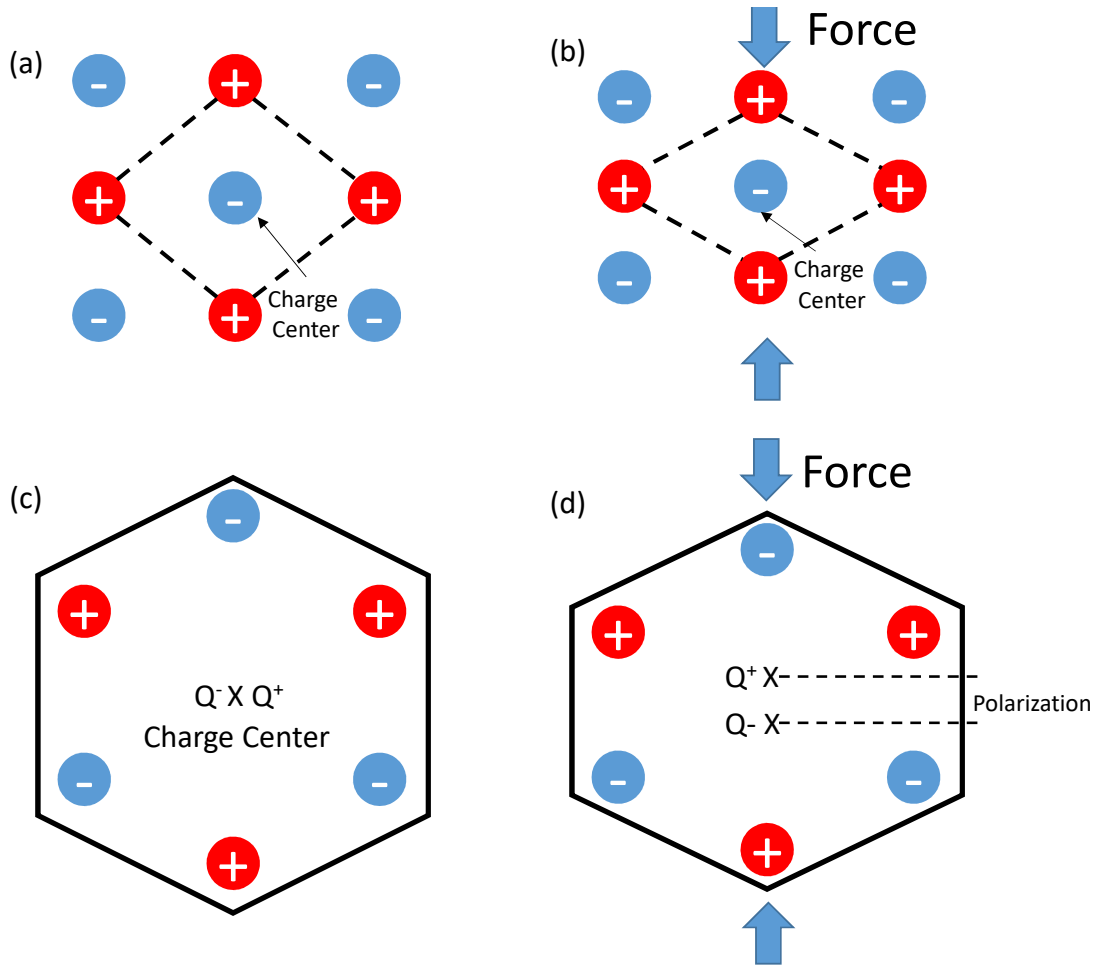

Figure 3.1. (a) Centrosymmetric crystal with no applied force, resulting in overlapping charge centers and no polarization. (b) Centrosymmetric crystal with an applied force, the charge centers are still overlapping and there is no polarization. (c) Non-centrosymmetric crystal with no force, where both charge centers overlap. (d) With an applied force the charge centers to move away from each other resulting in a polarization.

can be derived and may be more convenient for certain applications than the equations described above [114].

The piezoelectric constant d is typically expressed in matrix notation, where matrix notation -> tensor notation 1->11; 2->22; 3->33; 4->23,32; 5->31,13; 6->12,21. The sign convention assumes that the poling direction is always in the "3" direction (for ceramics). For example a d_{31} coefficient means the field is applied in the "3" (parallel to the poling) direction and strain is measured in the "1" (perpendicular to the poling) direction

The typical ferroelectric curve is illustrated in figure 3.2(a) showing the polarization

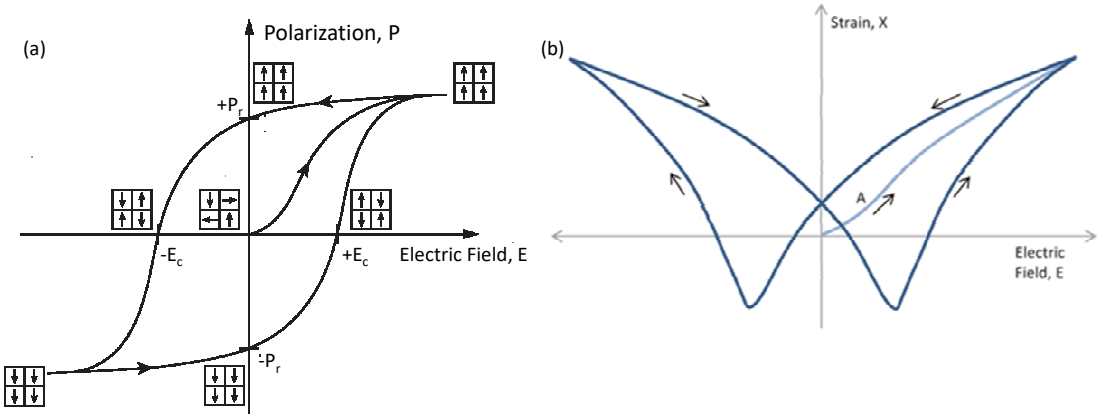

Figure 3.2. (a) Typical ferroelectric hysteresis curve. The initial random polarization is aligned with application of an electric field. Upon removal of the field a remanent polarization ($\pm P_r$) remains. To return the domains to null net polarization an opposite field of sufficient magnitude, known as the coercive field $\pm E_c$ must be applied. (b) The typical piezoelectric strain curve shows how the strain develops with an applied electric field.

vs. electric field. Initially the as-fabricated materials is assumed to have perfectly random polarization (in real devices this is not always true). After initial application of a positive electric field the polarization increases until saturation. Next, upon reversing the direction of the electric field a remanent polarization $+P_r$ at 0 V/m until the polarization is zero at the coercive field $-E_c$. Sweeping the electric positive again produces an analogous effect with a negative remanent polarization $+P_r$ at 0 V/m and a $+E_c$. A typical ferroelectric piezoelectric curve, sometimes refereed to as a "butterfly curve", is illustrated in figure 3.2(b) showing the strain vs. electric field. Analogous to the ferroelectric curve, initial application of a positive electric field increases the strain until it saturates and upon removal of the electric field a remanent strain remains. Reversing the electric field produces negative strain at first, then it will reverse direction and positive strain will increase until it is saturated. It should be noted that while the step (inverse slope) is linear at low electric fields at higher fields the step is larger (more voltage is needed produce the same strain), conversely a differential strain produced on a biased piezoelectric will produce a larger differential voltage making it a better strain to voltage transducer. The effect has been experimentally demonstrated by Li et al. [117] and shown in figure 3.3.

Table 3.1 shows some contemporary piezoelectric materials and their piezoelectric coefficients. Quartz is commonly used for sensing due to it's high quality factor resonance modes. Despite having a lower piezoelectric coefficient PZT is relatively inexpensive and exhibits good temperature stability with piezoelectric properties observable up to

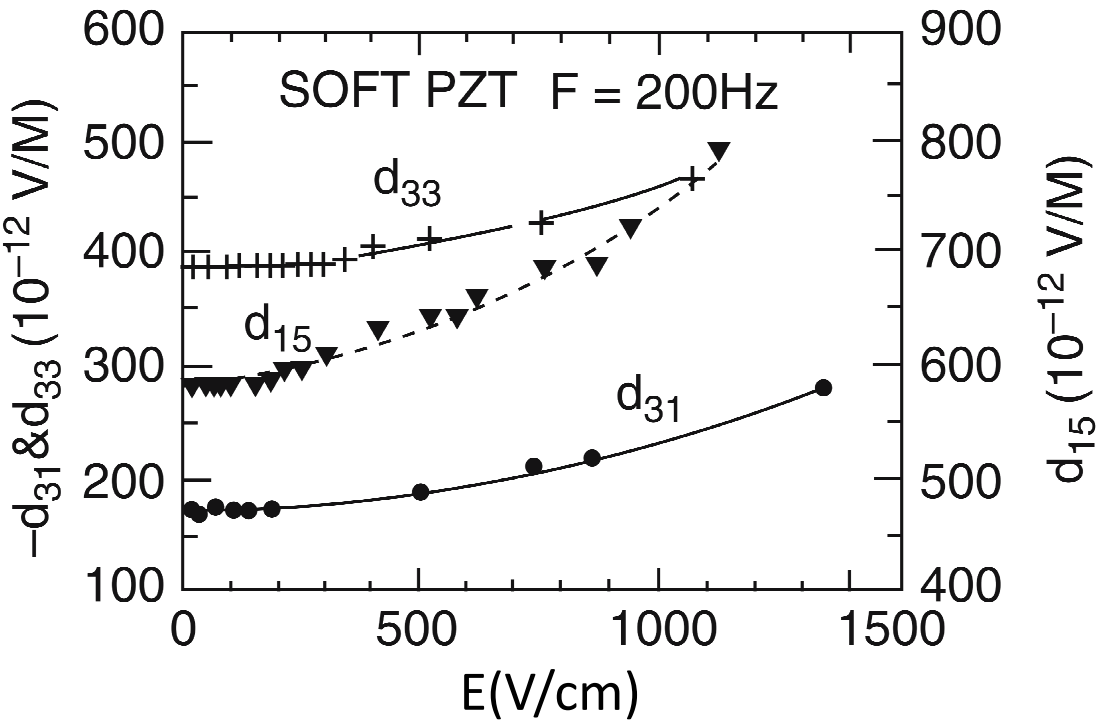

Figure 3.3. Ferroelectric piezoelectric coefficients increasing with increased electric field due to the non-linear nature of the phenomenon. [117]

approximately it's phase transition to β-quartz at 573 °C [118]. Where as the Curie temperature of PMN-32PT is 150 °C [119] and PZN-4.5PT has a ferroelectric phase transition at 130 °C [120].

Table 3.1. Piezoelectric constants and their permittivity for several commonly used materials: x-cut quartz, Pb[Zr_xTi_{1-x}]O_3 (PZT), polyvinylidene difluoride (PVDF), 0.70Pb($Mg_{1/3}$ $Nb_{2/3}$)O_3-0.30$PbTiO_3$ (PMN-30%PT), 0.93Pb($Zn_{1/3}$ $Nb_{2/3}$)O_3 -0.08$PbTiO_3$ (PZN-8%PT)

Material	d_{31} (pm/V)	d_{33} (pm/V)	ϵ_{33}:ϵ_{11}
Quartz X-cut [121]	-	2.3	4.6:4.6
PZT-5A [122]	-171	374	1700:1730
PZT-5H [122]	-276	630	
PVDF	21 [123]	-32.5 [123]	7.6:6.9 [124]
PMN-30%PT [125]	-921	1981	7800:3600
PZN-8%PT [126]	-1455	2890	7700:2900

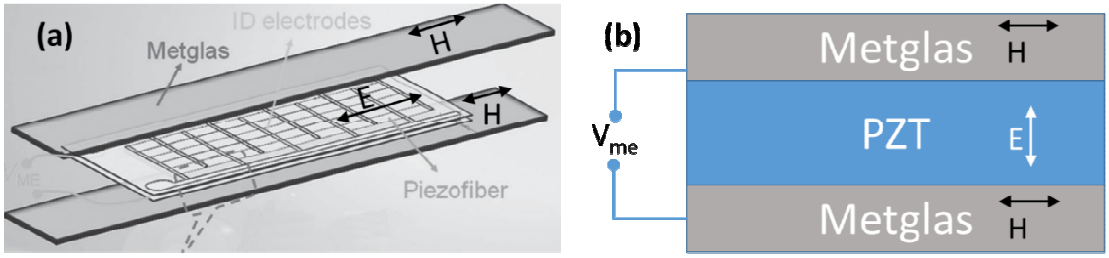

Figure 3.4. (a) Illustration of an in-plane longitudinal ME device [48]. The magnetic field (H) is applied in-plane and the electric field is measured in-plane. (b) Illustration of a transverse ME device. The H field is in-plane and the electric field is measured out of plane.

3.2.2 Magnetoelectric Effect

The magnetoelectric effect was introduced earlier in section 1.3.1. Applying a DC magnetic to bias the magnetostriction film allows for the linear sensing of weak AC magnetic fields. This oscillating magnetic field translates into an oscillating mechanical strain. That strain is then transduced into a charge/voltage by the piezoelectric material.

Two commonly reported methods of fabricating a magnetoelectric device are to use the in-plane longitudinal, as illustrated in figure 3.4(a), or the transverse piezoelectric effect, as illustrated in figure 3.4(b). The in-plane longitudinal device has the benefit of higher in-plane piezoelectric constant that exists for PZT and PMN-PT, but requires interdigitated electrodes and has a more complex construction process.

The magnetoelectric phenomenon can be modeled by relating the strain between the piezoelectric and magnetostrictive phases as first demonstrated by Harshe et al. [127]. The strain from the phases can be modeled as (3.4) and (3.5):

$$ {}^{m}S_i = {}^{m}s_{ij}\,{}^{m}T_j + {}^{m}q_{ki}\,{}^{m}H_k \tag{3.4} $$

$$ {}^{p}S_i = {}^{p}s_{ij}\,{}^{p}T_j + {}^{p}d_{ki}\,{}^{p}E_k \tag{3.5} $$

where m and p denote the magnetostrictive and the piezoelectric phases respectively. q is the pseudo-piezomagnetic coefficient (also known as the magnetostrictive coefficient), d is the piezoelectric coefficient, T is the stress, H is the magnetic field, s is the compliance matrix, and S is the strain. The prefixes m and p refer to the magnetostrictive and piezoelectric phases respectively.

A general strain equation, which takes into consideration the contributions from the

stress field, electric field (piezoelectric) and magnetic field (magnetostrictive) can be written as (3.6):

$$\mathbf{S} = \mathbf{sT} + \mathbf{dE} + \mathbf{qH} \tag{3.6}$$

The electric displacement (D) for a piezoelectric is

$$\mathbf{D} = \mathbf{dT} + \varepsilon\mathbf{E} \tag{3.7}$$

Assuming some boundary conditions, the magnetoelectric voltage α(E/H) can be solved analytically. For example, first consider the case of a magnetoelectric device in free space with a piezoelectric and a magnetostrictive layer stacked on each other, with the piezoelectric electrodes along the out of plane (3 - axis) direction and the magnetic field applied in the out of plane direction. In this case the *H* field is applied out of plane and the *E* field is measured out of plane $\alpha(E_3/H_3)$ the following boundary conditions can be established (3.8), (3.9), (3.10):

Assuming free body conditions with no stresses present there will be no out of plane stress

$$^{m}T_3 = {}^{p}T_3 = 0 \tag{3.8}$$

Assuming in plane stresses are equal: $^{p}T_1 = {}^{p}T_2$ & $^{m}T_1 = {}^{m}T_2$

$$\begin{aligned} {}^{m}T_1 {}^{m}v &= -{}^{p}T_1 {}^{p}v \\ {}^{m}T_2 {}^{m}v &= -{}^{p}T_2 {}^{p}v \end{aligned} \tag{3.9}$$

where *v* = volume fraction.

The strain in plane is equal for both materials

$$\begin{aligned} S_1 = {}^{m}S_1 = {}^{p}S_1 \\ S_2 = {}^{m}S_2 = {}^{p}S_2 \end{aligned} \tag{3.10}$$

Using (3.6), a general strain relationship for each phase is written as (3.11)

$$
\begin{aligned}
{}^{m}S_1 &= {}^{m}s_{11}\,{}^{m}T_1 + {}^{m}s_{12}\,{}^{m}T_2 + {}^{p}s_{13}\,{}^{m}T_3 + {}^{m}q_{31}H_3 \\
{}^{p}S_1 &= {}^{p}s_{11}\,{}^{p}T_1 + {}^{p}s_{12}\,{}^{p}T_2 + {}^{p}s_{13}\,{}^{p}T_3 + {}^{p}d_{31}E_3
\end{aligned}
\tag{3.11}
$$

Since $T_3 = 0$, ${}^{m}T_1 = {}^{m}T_2$, and ${}^{p}T_1 = {}^{p}T_2$, the equations in (3.11) can be equated to get (3.12).

$$
\left({}^{m}s_{11} + {}^{m}s_{12}\right){}^{m}T_1 + {}^{m}q_{31}H_3 = \left({}^{p}s_{11} + {}^{p}s_{12}\right){}^{p}T_1 + {}^{p}d_{31}E_3 \tag{3.12}
$$

substituting ${}^{m}T_1 = -{}^{p}T_1\,{}^{p}v/{}^{m}v$ one gets (3.13)

$$
\left({}^{m}s_{11} + {}^{m}s_{12}\right) - {}^{p}T_1\left({}^{p}v/{}^{m}v\right) + {}^{m}q_{31}H_3 = \left({}^{p}s_{11} + {}^{p}s_{12}\right){}^{p}T_1 + {}^{p}d_{31}E_3 \tag{3.13}
$$

Assuming open circuit conditions (D=0):

$$
D_3 = {}^{p}d_{31}\,{}^{p}T_1 + {}^{p}d_{32}\,{}^{p}T_2 + {}^{p}d_{33}\,{}^{p}T_3 + {}^{p}\varepsilon_{33}E_3 = 0 \tag{3.14}
$$

Using ${}^{p}T_1 = {}^{p}T_2$ and ${}^{p}d_{31} = {}^{p}d_{32}$ in (3.14), results in (3.15)

$$
{}^{p}T_1 = -\frac{{}^{p}\varepsilon_{33}^{T}E_3}{2{}^{p}d_{31}} \tag{3.15}
$$

and now ${}^{p}T_1$ can be substituted out using (3.15) and rearranged, resulting in (3.16)

$$
\alpha_{(E)33} = \frac{E_3}{H_3} = \frac{-2{}^{m}q_{31}\,{}^{p}d_{31}\,{}^{m}v}{\left({}^{m}s_{11} + {}^{m}s_{12}\right)\left({}^{p}\varepsilon_{33}^{T}\right){}^{p}v + \left({}^{p}s_{11} + {}^{p}s_{12}\right)\left({}^{p}\varepsilon_{33}^{T}\right){}^{m}v - 2\left({}^{p}d_{31}\right)^{2}{}^{m}v} \tag{3.16}
$$

For the case of the piezoelectric electrodes along the out of plane (3 - axis) direction and the magnetic field applied in the in plane direction such as the device in figure 3.4(b), the solution is similar, only the ${}^{m}q_{33}$ value is swapped for ${}^{m}q_{11} + {}^{m}q_{21}$ (3.17). Bichurin et al. included a coupling factor, k making the equation (3.18) [88, 128]. For the special case of k=1, (3.18) = (3.17).

$$\alpha_{(E)31} = \frac{E_3}{H_1} = \frac{-2({}^{m}q_{11}+{}^{m}q_{21})^{p}d_{31}{}^{m}v}{({}^{m}s_{11}+{}^{m}s_{12})\,({}^{p}\varepsilon_{33}^{T})\,{}^{p}v + ({}^{p}s_{11}+{}^{p}s_{12})\,({}^{p}\varepsilon_{33}^{T})\,{}^{m}v - 2({}^{p}d_{31})^{2}{}^{m}v} \tag{3.17}$$

$$\alpha_{(E)31} = \frac{E_3}{H_1} = \frac{-2k({}^{m}q_{11}+{}^{m}q_{21})^{p}d_{31}{}^{m}v}{({}^{m}s_{11}+{}^{m}s_{12})\,({}^{p}\varepsilon_{33}^{T})\,k{}^{p}v + ({}^{p}s_{11}+{}^{p}s_{12})\,({}^{p}\varepsilon_{33}^{T})\,{}^{m}v - 2({}^{p}d_{31})^{2}k{}^{m}v} \tag{3.18}$$

3.3 Experimental Setup

3.3.1 Magnetoelectric Device Fabrication and Sensing

To measure the magnetoelectric coefficient, laminate structures are fabricated using the same method described earlier in section 2.2.1.4, figure 2.4(a-b). However, a number of parameters are varied to test their effect on the magnetoelectric coefficient. The three components of the PZT-5A/Metglas 2605SA1 magnetoelectric device are optimized. PZT-5A is chosen for these sets of experiments because of it's low cost ($10 USD for 3 mm $\times$ 13 mm $\times$ 200 μm plate) and commercial availability. First the effect of Metglas dimension in regards to flux concentration is investigated by COMSOL simulations and by experimentally varying the Metglas length from 15 mm to 50 mm. Next, the coupling efficiency of the epoxy is investigated by modeling the average stress transfered for varying epoxy thicknesses and epoxy modulus. Based on the simulation results an appropriate epoxy modulus is chosen and the magnetoelectric coefficient is measured using an epoxy layer cured without a clamp (thicker epoxy) and a device using an epoxy layer cured while mechanically clamped. Finally, the domain aligned Metglas is incorporated and the effect of DC voltage biasing the PZT-5A during sensing to temporarily increase the d_{31} coefficient during sensing. The limit of detection is compared for all of the optimizations.

The devices are tested in a custom designed box with three layers of magnetic shielding as described earlier in section 2.2.1.4. Two pairs of Helmholtz coils are used for DC and AC magnetic stimulation inside the shielded box. An AC current source is used to automatically adjust for impedance variations in the coil and provide a stable magnetic field strength across a range of frequencies. The voltage generated by the PZT

is measured by a lock-in amplifier as seen in the illustration of the test setup in figure 2.5.

3.4 Force Coupling Optimization

The coupling between the magnetostrictive component and piezoelectric must be as ideal as possible to realize the full potential of the ME laminate. The effect of epoxy thickness and Young's modulus is studied in COMSOL 5.2 Multiphysics software. It can be seen from figure 3.5(a) that as the thickness of epoxy is reduced, the stress coupling to the PZT becomes better as the average stress increases for an epoxy Young's Modulus of 1 GPa to 12 GPa. However, the average stress is seen to peak for an epoxy Young's modulus between 5 GPa to 10 GPa, depending on the epoxy thickness as seen in figure 3.5(b), due to a trade-off between the epoxy absorbing strain when it is too compliant and reduction in strain transfer when the epoxy is too stiff.

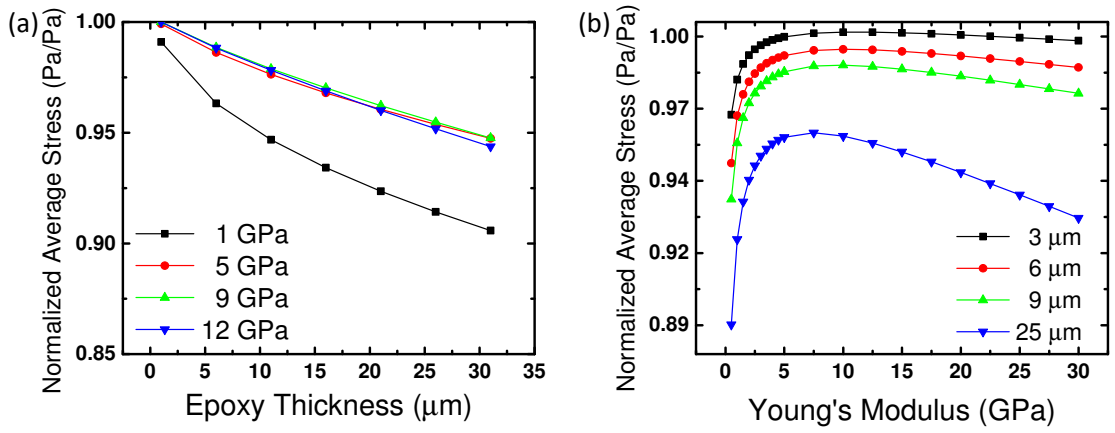

Figure 3.5. (a) Average stress coupling as a function of epoxy thickness with varying Young's modulus of the epoxy from 1-12 GPa shows thinner films are more effective at stress coupling. (b) Average stress coupling versus epoxy Young's modulus shows an optimal Young's modulus of 5 GPa to 10 GPa, depending on epoxy thickness.

A conductive silver epoxy with a Young's modulus of 6 GPa is chosen for these experiments [129]. Applying the epoxy without clamping during the cure results in a relatively thickness of 10 µm to 17 µm and porous film as seen in the scanning electron micrograph (SEM) cross section shown in figure 3.6(a). Applying a clamp during the cure reduced the thickness to 3 µm to 9 µm with clearly reduced porosity in the epoxy layer as seen in figure 3.6(b). This resulted in a significantly improved α_{me} of 2.02

MV/(m·T) compared to 0.32 MV/(m·T) for non-clamped curing. All further tests in this thesis uses the clamped curing method.

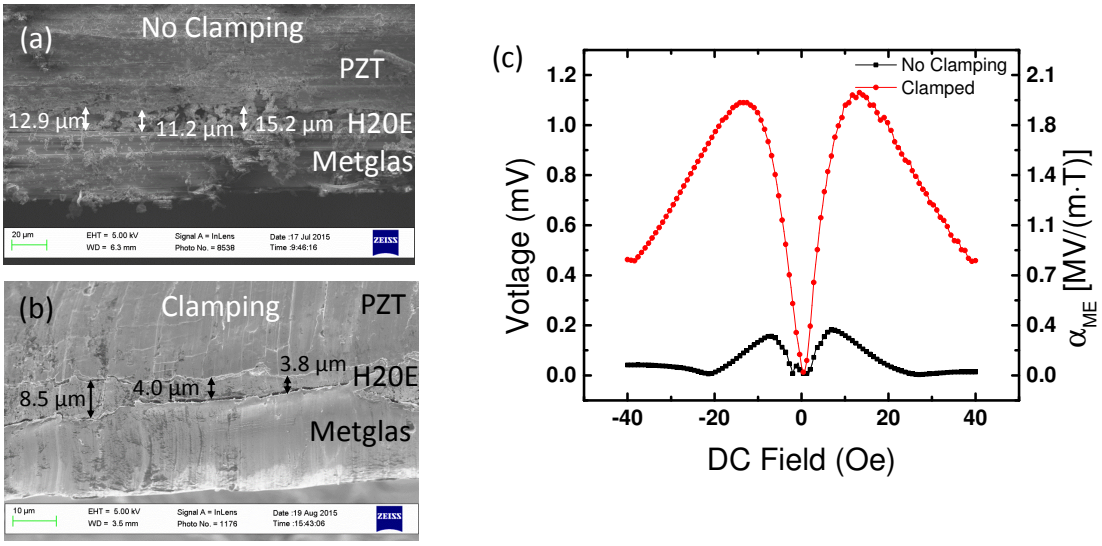

Figure 3.6. SEM cross sections of devices: (a) constructed with manual application of H20E without clamping results in a 10 µm to 17 µm thick and porous interface. (b) Constructed with clamping during the cure results in a thinner, 3 µm to 9 µm thick and non-porous H20E epoxy interface. (c) The experimental α_{me} difference between the clamped and unclamped curing process, showing a large improvement from 0.32 MV/(m·T) to 2.02 MV/(m·T).

3.5 Flux Concentration of Metglas 2605SA1

Flux concentration occurs in high permeability materials like Metglas. The ferromagnetic material "draws in" magnetic flux lines because these lines have a strong preference for high permeability materials over air/vacuum. A 2D COMSOL simulation is used to investigate how length and width effect the flux concentration and offer insight into trends one may expect when defining the shape of the Metglas ribbons. A 3D COMSOL simulation is also carried out to investigate the thickness trend. In the 2D COMSOL model the width is varied from 1 mm to 8.5 mm and the length from 5 mm to 30 mm, while the μ_r is kept constant at 10,000. There are reports of Metglas with much higher μ_r values, but the goal of this work is to see the trend and it is only important that the material being modeled have a much higher permeability than the surrounding medium($\mu_r \gg 1$) to investigate the trends. For consistency, the surrounding air in the medium is also

scaled by the same factor as the high μ_r material dimensions scale. Figure 3.7(a) shows a 1 mm $\times$ 5 mm high μ_r strip in air with a background 25 μT magnetic field. As can be seen by the streamlines of the magnetic field, strong magnetic flux concentration is occurring. A cutline measuring the magnetic field along the length is used to compare the flux concentration effect. Figure 3.7(b) shows that the magnetic field scales directly with length and inversely with width. The trends in the simulations are in good agreement with similar analysis done by Zhao Fang [50].

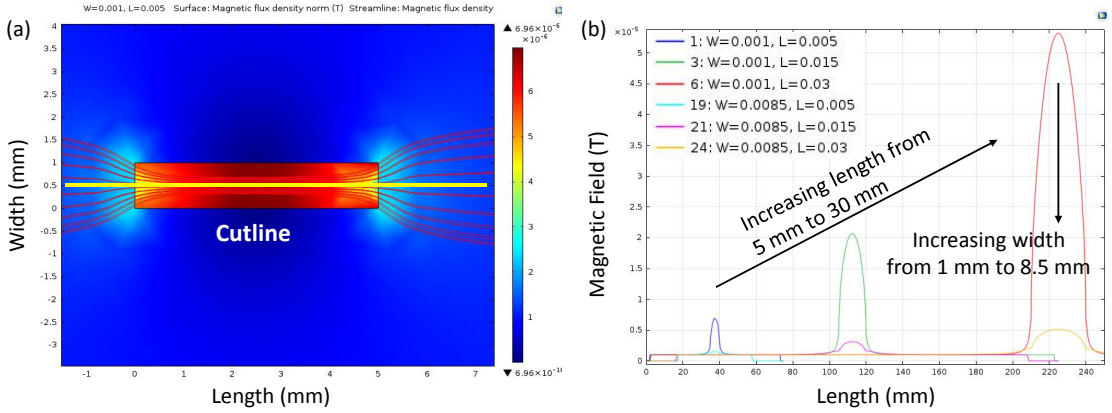

Figure 3.7. (a) 1 mm $\times$ 5 mm 10,000 μ_r permeability material in air, with a background 25 μT field along the length of the ribbon. The streamlines show the effect of flux concentration into the high permeability material. The magnetic field along the cutline is evaluated in (b), showing a summary of the trends observed by varying length and width. The internal magnetic field increases directly proportional to length, but inversely proportional to the width of the high permeability material.

Experimental verification of the length trend is done by making magnetoelectric devices from PZT 5A/Metglas 2605SA1 with varying Metglas lengths of 15 mm, 30 mm and 50 mm. As predicted, the magnetoelectric voltage scales directly with length as seen in figure 3.8, where a 20 Hz, 5.6 μT AC magnetic field is applied, while the DC magnetic field is varied. It should also be noted that the magnitude of the DC magnetic field corresponding to the peak magnetoelectric response decreased as the length increased, consistent with what one would expect from magnetic flux concentration.

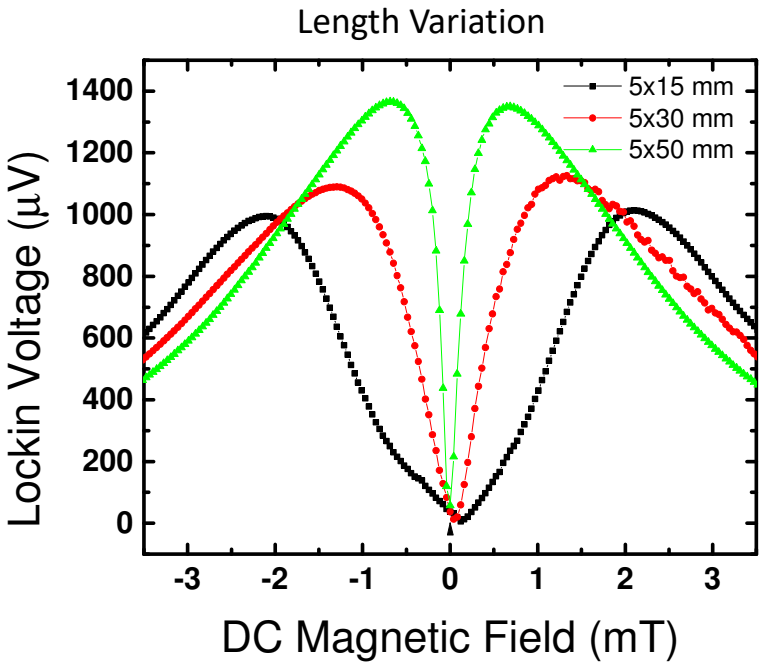

Figure 3.8. Flux concentration experiment showing significant improvement in the magnetoelectric voltage by increasing the length of the Metglas.

To investigate the effect of thickness a 3D COMSOL model must be used. A 5 mm $\times$ 80 mm $\times$ 500 μm to 2000 μm thick high permeability ($\mu_r = 10,000$) film is placed between a pair of Helmholtz coils as seen in figure 3.9(a). To keep the model simple the thickness is made much larger than the actual Metglas ribbon thickness (25 μm), but the observed trends will still be valid. The magnetic field in the material is probed along the length using a cutline placed in the center of the ribbon. As the thickness increased the magnetic field decreased as seen in figure 3.9(b), meaning there was less flux concentration. Some authors have reported higher magnetoelectric response when epoxying multiple Metglas ribbons together [130], but this may be because the improved magnetostriction to piezoelectric volume ratio has a stronger effect than the reduced flux concentration in some cases. Authors also report an increase in the magnitude of the DC magnetic field required to reach peak magnetoelectric voltage as the number of Metglas layers is increased, consistent with reduced flux concentration.

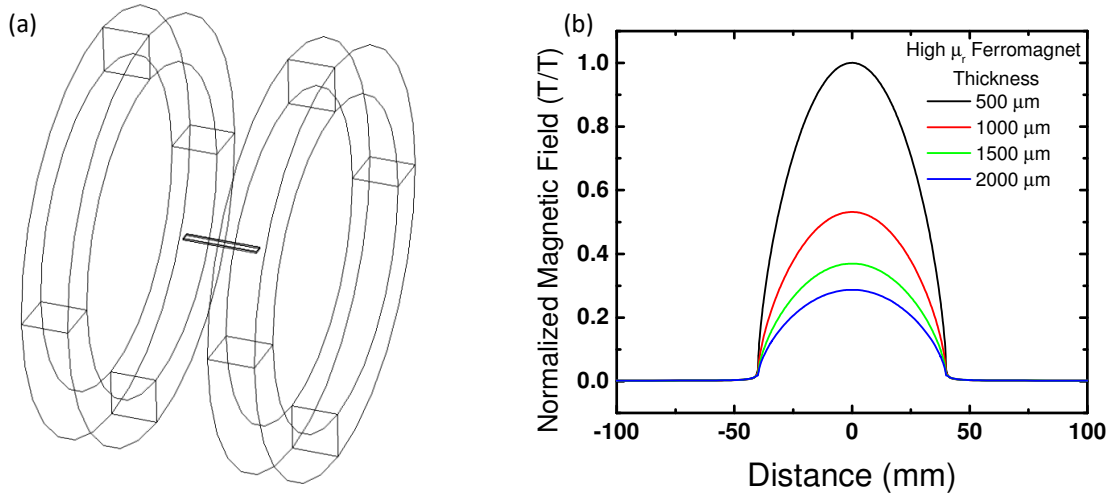

Figure 3.9. (a)3D COMSOL model used to study the thickness effects on Metglas. A 5 mm $\times$ 80 mm $\times$ 500 μm to 2000 μm thick high permeability ($\mu_r = 10,000$) film is placed between a pair of Helmholtz coils. (b) A cutline taken through the center of the ribbon shows the magnetic field inside the Metglas decreases at the thickness increases, meaning there is less flux concentration with increased thickness.

3.6 Piezoelectric Optimization via Active Biasing

Electric field biasing of the PZT-5A modifies the d_{31} coefficient and thus improves α_{me}. A 30 minute vacuum annealed and magnetically poled Metglas-PZT device is DC electric field biased to alter the d_{31} coefficient. Varying electric fields are applied by series connected DC batteries to minimize unwanted noise. Figure 3.10 shows the magnetostriction curve as a function of the applied magnetic field for applied DC electric fields from -2 to +2 kV/cm (limited by the maximum DC voltage permitted on the lock-in amplifier). At +2 kV/cm α_{me} increases by 59 % to 9.52 MV/(m·T) from the no electric field α_{me} of 5.98 MV/(m·T) and at -2 kV/cm α_{me} decreases 50 % to 3.02 MV/(m·T). The increased α_{me} of 9.52 MV/(m·T), enables an improved lower detection limit in ME magnetic field sensing. The improvement in sensitivity due to the optimization is measured in the next chapter.

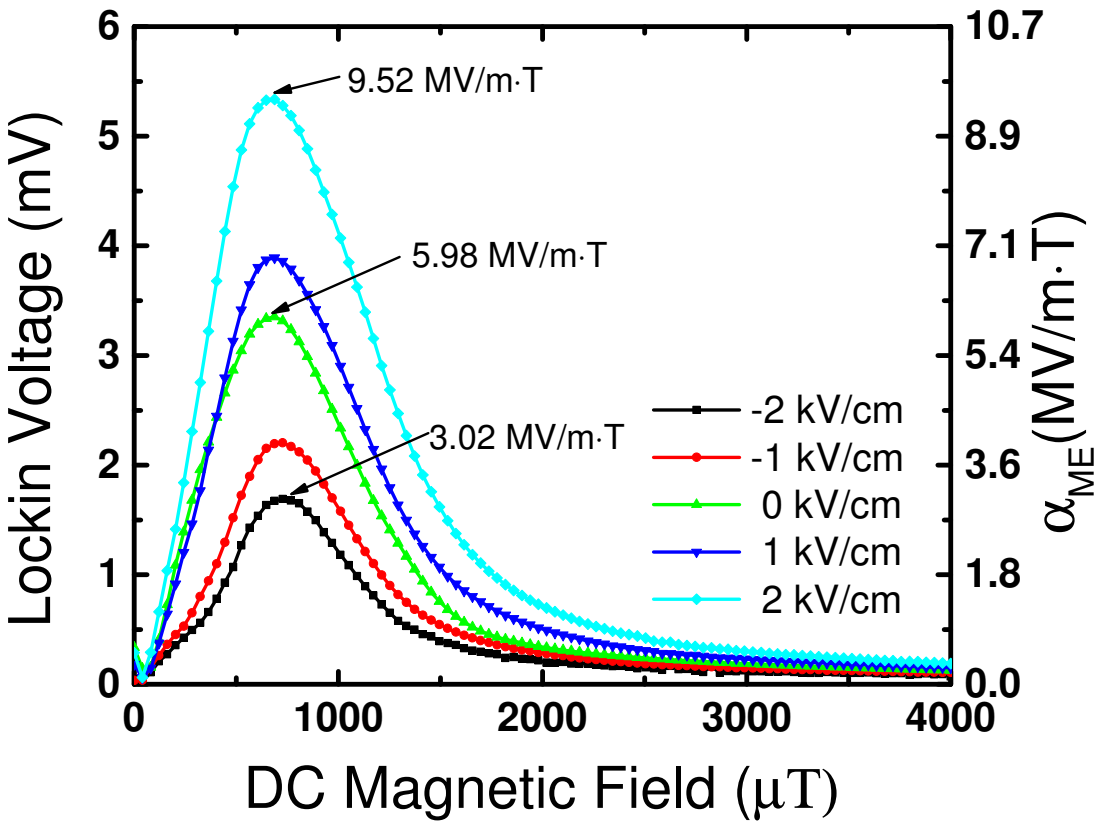

Figure 3.10. Magnetostriction curves under a DC electric field bias measured under a 2.8 μT AC field at 20 Hz. A 59% improvement is observed with a +2 kV/cm electric field.

3.7 Optimized Magnetometer Limit of Detection

The sensor resolution is compared for the various optimization methods. All of the optimizations improve the signal and unless the sensing setup is limited by magnetic noise the signal to noise ratio should improve and result in improved sensitivity. To evaluate the sensitivity the sensors are biased in their optimal DC magnetic field and a 20 Hz AC magnetic field is gradually reduced until the response becomes non-linear signaling a limit of detection. Figure 3.11 shows the limit of detection (LOD) for the optimizations discussed in this chapter. The initial un-clamped and un-annealed device had a 6 nT LOD. After curing in a clamp the LOD improves to 1 nT. The addition of an annealing step to remove residual stress with a 5 minute 400 °C anneal in atmosphere without a magnetic field improved the LOD to 350 pT. Next, by aligning the magnetic domains perpendicular to the sensing axis the maximum amount of magnetostriction

coefficient the LOD is reduced to 250 pT. This alignment is achieved by a 30 minutes 400 °C anneal in nitrogen with a 160 mT magnetic field aligned along the short axis of the Metglas ribbon. At the time of these experiments the annealing setup could only accept a maximum length of 30 mm and the strip width was limited to 5 mm for ease of handling. Finally the PZT-5A is biased with a +40 V DC bias along the remanent polarization direction to temporarily improve the d_{31} coefficient and provide a further improvement in the LOD to 150 pT.

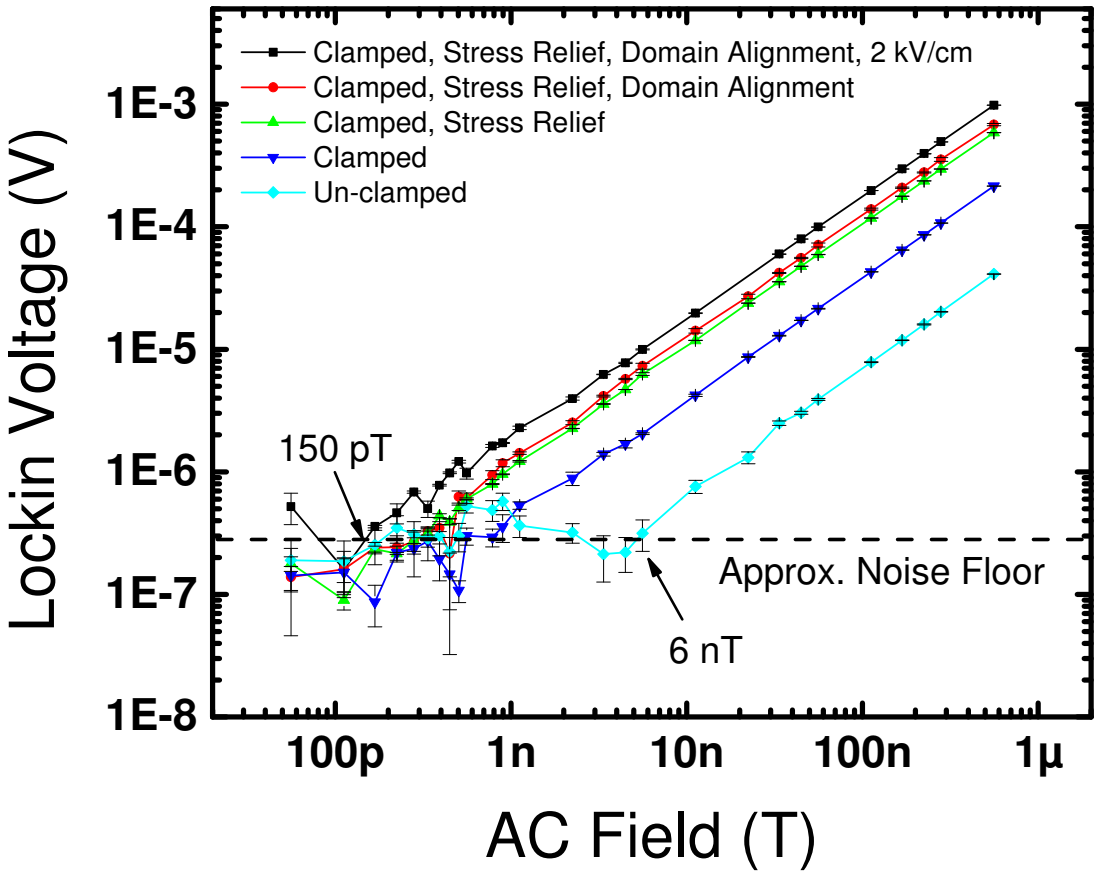

Figure 3.11. Measured lock-in voltage for decreasing 20 Hz AC magnetic showing an improvement in sensitivity from 6 nT in the un-optimized sample to 150 pT in the optimized sample with no observable change in the noise floor.

3.8 Conclusion

Thinning the epoxy and reducing the porosity using a mechanical clamp resulted in a 6.7× improvement in the magnetoelectric coefficient from 0.3 MV/(m·T) to 2.0 MV/(m·T). Annealing the Metglas without a magnetic field improved the magnetoelectric coefficient by 2.5× from 2.0 MV/(m·T) to 5.0 MV/(m·T). Annealing the Metglas with a 160 mT magnetic field to align the domains along the short axis of the ribbon and limit crystallization by using an oxygen free environment resulted in a further 1.2× improvement from 5.0 MV/(m·T) to 6.1 MV/(m·T). Finally a 2.0 kV/cm DC electric field is used to increase the d_{31} resulted in a 1.6× improvement from 6.1 MV/(m·T) to 9.5 MV/(m·T). The limit of detection at 20 Hz improved from 6 nT to 150 pT due to the optimizations. Further improvements by using PMN-PT in d_{33} sensing mode with interdigitated electrodes and longer domain aligned Metglas strips to improve flux concentration is discussed later.

Chapter 4

PMN-PT/Metglas 2605SA1 In-plane Magnetoelectric Magnetometer

4.1 Introduction

The magnetostriction component of the magnetoelectric device has been optimized in chapter 2. The piezoelectric component can be replaced with a more sensitive element, namely (1-x)[Pb($Mg_{1/3}Nb_{2/3}$)O_3]-x[$PbTiO_3$] (PMN-PT). Furthermore the large d_{33} component can be exploited using interdigitated electrodes. PMN-PT is commercially available and PMN-PT macro fiber composites with interdigitated electrodes are commercially available.

In the first part of the chapter COMSOL finite element modeling is used to investigate the electric field distribution due to the interdigitated electrodes. Nelson et al. showed that dead spots and the electric field is non-uniform [131] in PZT based interdigitated electrode devices. The displacement is simulated for various electrode configurations. Poling procedures are evaluated to pole the PMN-PT and optimized. Finally, Metglas 2605SA1 is epoxied to the piezoelectric and the magnetoelectric response was compared and modeled by COMSOL.

4.2 Finite Element Modeling

A COMSOL simulation was done to evaluate the electric field lines produced by the interdigitated electrodes. The displacement was simulated for various electrode configu-

rations. A COMSOL model using PMN-PT sections was created with 1 mm PMN-PT sections and 0.2 mm electrodes. The final dimensions are 27 mm long, 4 mm wide and 0.4 mm thick. 1 V is applied between each 1 mm section and one end surface is fixed as a hard point. Figure 4.1(a) shows the simulated displacement of the device. Figure 4.1(b) is the y-component of the electric field taken as a cut-line near the surface, where the field is approximately 600 V/m or 60% of the ideal value expected based on the electrode spacing due to the longer path the field lines take. This is consistent with other simulations and experiments done with interdigitated electrodes [132]. Figure 4.1(c) is a cut-line of the displacement showing a linear response with small breaks due to the deadzones induced by the electrodes. Equation (4.1) is the analytical expression used to calculate displacement (λ) in a piezoelectric, where d_{33} is the piezoelectric constant, *E* is the electric field and *l* is the length. Using the 600 V/m electric field simulated earlier, and the length of the active length is subtracted by length lost to the electrodes (4.8 mm), the displacement was calculated to be 27 nm, close to the 25 nm simulated.

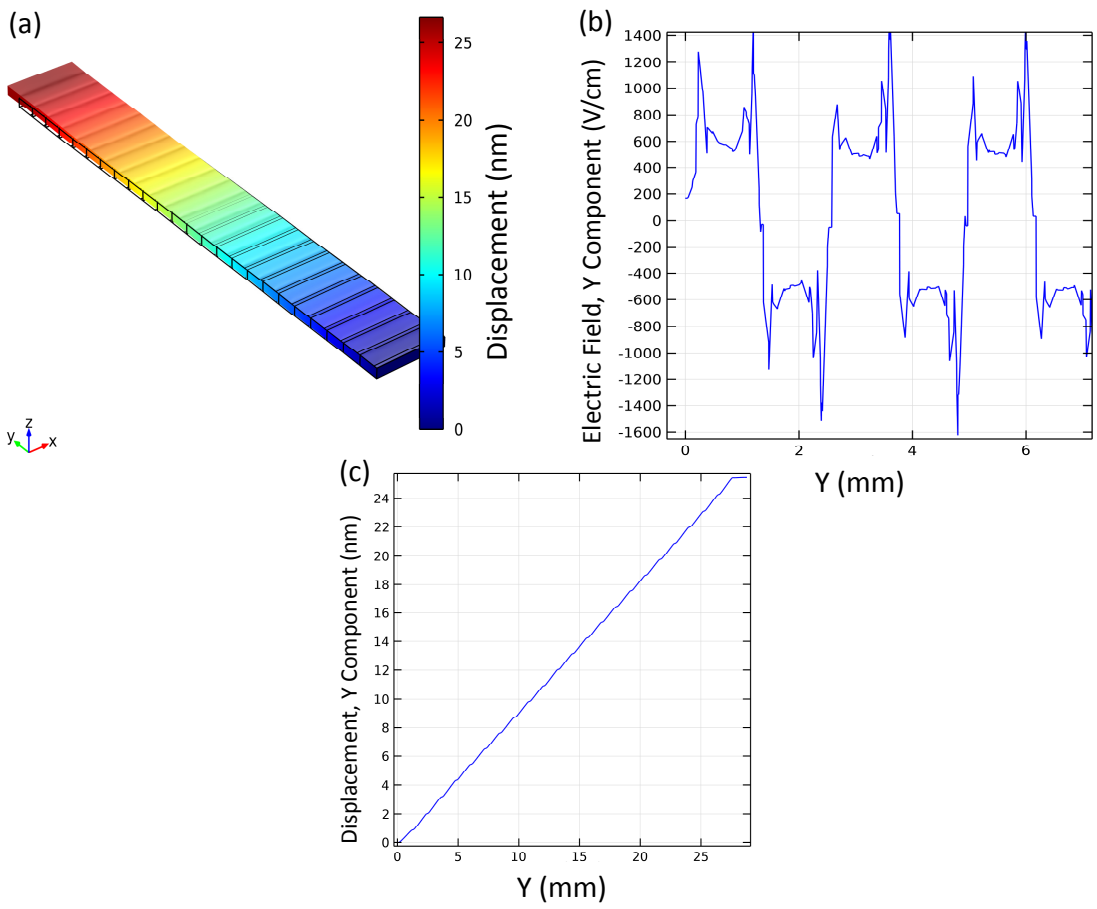

Figure 4.1. (a) Displacement of a PMN-PT cantilever with 1 V applied to the electrodes. (b) The electric field is approximately 600 V/m or 60% of the ideal value. (c) Total displacement was simulated to be approximately 25 nm.

$$\lambda = d_{33} \cdot E \cdot l = 2000 \frac{\text{pm}}{V} \left(\frac{\text{m}}{\text{m}}\right) \cdot 600 \ \frac{\text{V}}{\text{m}} \cdot (27 - 4.8) \ \text{mm} = 27 \ \text{nm} \qquad (4.1)$$

Now that the model has been validated the non-ideal nature of practical electrodes is simulated. Figure 4.2 shows the displacement for a realistic configuration where electrode rails running along the length of the sample are 0.3 mm from the edges and the interdigitated fingers lengths go up to 600 μm from the edge of the opposite electrode rail. The reduced piezo-active area results in a reduced displacement of 14.5 nm.

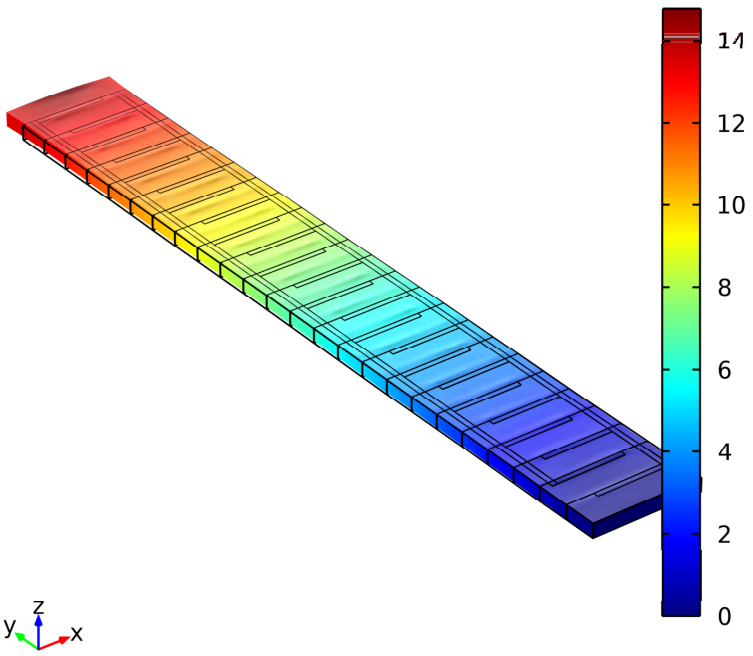

Figure 4.2. Using a realistic electrode configuration the deflection is reduced to approximately 14.5 nm.

4.3 Fabrication of In-plane PMN-PT/Metglas 2605SA1 Magnetoelectric Devices

Magnetoelectric devices based on the d_{33} mode of PMN-PT are fabricated. Shadow masks are used to evaporate 50 nm Cr and 150 nm Au on each side of a 4 mm $\times$ 15 mm or 30 mm wide and 400 nm thick [001] PMN-0.3PT X2B single crystal sample, purchased from TRS Technologies (Pennsylvania, USA). Due to pseudo cubic structure of the material near identical performance can be expected when poling in either X,Y or Z axes. The electrodes are 300 µm wide and 2.4 mm long and spaced 1 mm edge to edge. A ceramic package (Spectrum Semiconductor CBS01652) was cut using a diamond saw to form the anchor of the cantilever. A 5 mm $\times$ 3 mm ceramic insert with 2 electrodes is epoxied, using Epotek H20E silver epoxy, to the ceramic package. Epotek H20E silver epoxy is again used to epoxy the PMN-PT to the conducting electrodes and is used to make the bottom connection of the PMN-PT. The silver epoxy is then used to epoxy a 3D printed plastic piece to help secure the sample in place. Finally epoxy is used to carefully connect ceramic insert contacts to the top electrode and to the package electrode. The

sample is cured at 90 °C for 3 hours. This is near the rhombohedral phase transition temperature of the PMN-PT, meaning it must be poled after this step. The package was inserted into a mini breadboard to form the final electrical connection and poling. Various poling procedures are explored in this chapter and ultimately a 30 second, 250 V poling in silicone oil at 60 ° is used. When poling the field is reported at the "ideal" field, meaning the electric field is *V/d*, where *V* is the applied voltage and *d* is the electrode to electrode gap. It will be explained in this chapter that the actual field felt by the PMN-PT is only a fraction of the ideal field. 5 mm $\times$ 30 mm $\times$ 23 μm thick Metglas 2605SA1 is magnetically poled and aligned in a nitrogen atmosphere under a 160 mT magnetic field for 30 minutes at 400 °C. The Metglas ribbon was epoxied to the sample using a non-conductive room temperature curable epoxy, Devcon 10 minute epoxy. The epoxy was applied to the Metglas and excess epoxy is carefully removed by a single edged steel razor blade. The sample was left to cure for 12 hours in a mechanical clamp.

Alternatively, commercially prepared d_{33} mode PMN-PT macro fiber composites (MFC) can be purchased from Smart Materials, who also use single crystal [001] PMN-PT X2B from TRS technologies. The MFC is composed of similar in dimensions to the monolithic PMN-PT samples 27 mm $\times$ 3 mm $\times$ 180 μm thick using 350 μm in-line PMN-PT fibers to form the composite. Similar to the monolithic case, magnetically poled and aligned 5 mm $\times$ 30 mm $\times$ 23 μm thick Metglas 2605SA1 was epoxied to the sample using a non-conductive room temperature curable epoxy, Devcon 10 minute epoxy and allowed to cure for 12 hours in a mechanical clamp.

4.4 Interdigitated Electrodes on Monolithic PMN-PT Single Crystal

4.4.1 Poling Procedure

To determine the appropriate poling procedure a 500 nm thick PMN-PT plate is poled through its thickness from 5.0 to 8.0 kV/cm and the d_{33} is measured using a Piezotest PM200 piezoelectric testing unit. Figure 4.3 shows saturation at 2000 pm/V at 6.0 kV/cm and another sample saturating at 1700 pm/V at 7.0 kV/cm. Poling was done in a silicone oil bath for 10 minutes. Conversations with engineers at TRS technologies, the PMN-PT manufacturer, suggest that poling for only 30 seconds is sufficient to induce a remanent polarization.

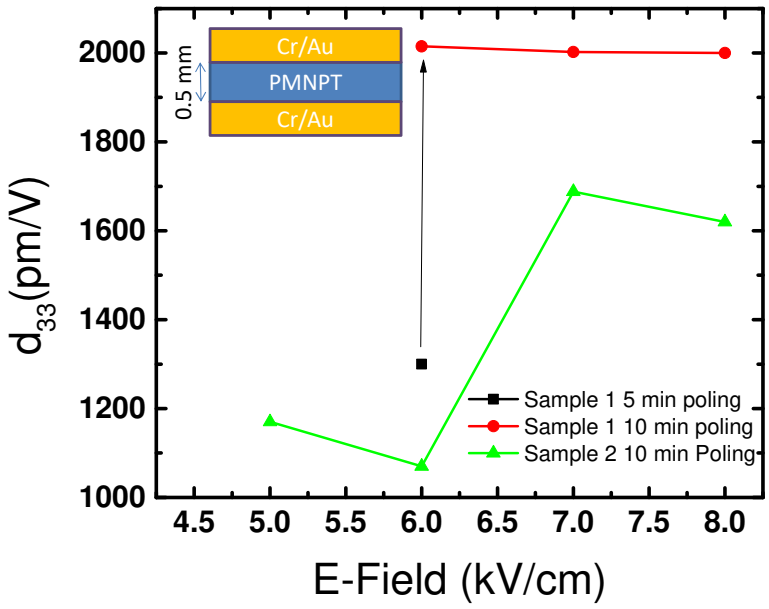

Figure 4.3. Poling through the thickness of a 500 nm thick PMN-PT shows d_{33} saturation at 2000 pm/V at 6.0 kV/cm and another sample saturating at 1700 pm/V at 7.0 kV/cm.

The 7.0 kV/cm poling field presents a problem for the interdigitated electrodes, because only approximately 60% of the electric field is expected to drop across the channel meaning the applied voltage must be high enough to compensate for the lower electric field due to the interdigitated electrodes. COMSOL simulations (not shown) suggest that there is not a significant deviation in the electric field along the thickness of the channel. Poling at 1100 V produced a significant number of cracks in the PMN-PT crystal and occasionally resulted in catastrophic cleaving of the sample. The cracking is most prominent in the regions of highest electric field, which are between the edge of the interdigitated electrode and the opposing rail electrode. The length of the electrode can be shortened at the expense of piezoelectric actuation and sensing. Figure 4.4(a) shows the effect of piezoelectric deflection in response to reducing the electrode to rail gap from 300 µm to 1300 µm, clearly showing a decrease in piezoelectric deflection as the gap is increased. Figure 4.4(b) shows the electrostatic voltage across the electrodes for the two extremes of electrode gap, where it is evident that as the gap increases, less of the piezoelectric channel sees a voltage differential. A compromise must be made to prevent high fields and cracking while enabling sensing and through as much of the channel as possible. A 600 µm gap is chosen because it only reduces the active area by 10%, yet decreases the electric field by a factor of 2× compared to 300 µm, which is the smallest

gap that can be realistically realized by our shadowmasking method. Also, to reduce the poling field, the temperature is increased to 60 °C. Shadowmasking is chosen because it offers quicker prototyping turnaround time and the technique was able to achieve the minimum desired resolution of 600 µm. Furthermore, by avoiding lithography we can reduce the number temperature cycles the PMN-PT sees during processing, reducing the potential of cracking due to thermal stresses.

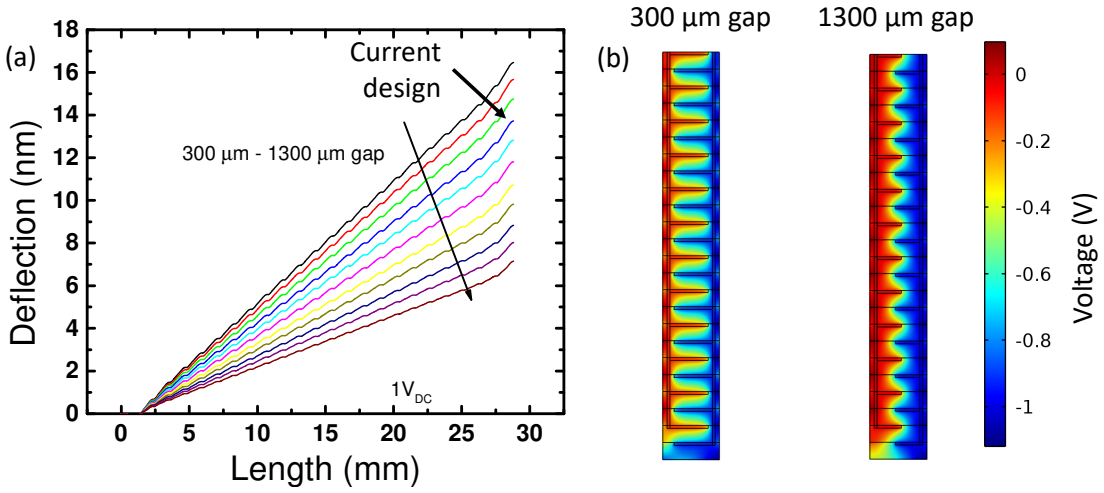

Figure 4.4. (a) Simulation of deflection with 1 V applied to the electrodes for a range of electrode to rail gap of 300 µm to 1300 µm, showing a decrease in active piezoelectric area with increased electrode to rail gap. (b) The electrostatic voltage for the two extremes of electrode to rail gap highlighting the reduced piezoelectric active area.

Figure 4.5 shows the X-Y-Z displacement is measured using a Polytec 3D MSA-100 laser Doppler vibrometer from a 15 mm × 4 mm 400 µm thick PMN-PT with 1 mm electrode to electrode gap and 600 µm electrode to rail gap. The deflection, and by relation the piezoelectric coefficients, saturate at 2.5 kV/cm. It should be noted that there is significant X and Z axis motion meaning that the poling is non-uniform in magnitude and/or at an angle to the Y-axis, which is expected given the complex field lines created from interdigitated electrodes.

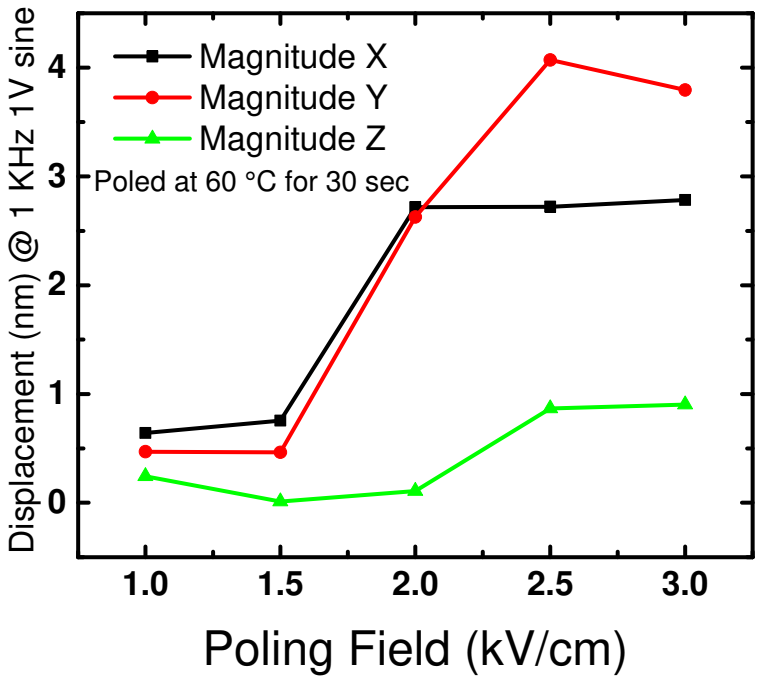

Figure 4.5. Experimental X-Y-Z displacement in versus poling field showing saturation of piezoelectric response at 2.5 kV/cm. The displacement in the X and Z axes is non ideal and is indication of non-uniform poling magnitude and/or an angle to Y-axis.

Figure 4.6(a) shows the electric field in the mid-plane of PMN-PT simulated on COMSOL with 1 V applied to the electrodes with the scale set to highlight the high field regions. As expected the gap between the electrode edge and the opposing electrode rail is the area of highest electric field. It should be noted that the opposing rails can be bulged out near the electrode edge to prevent high fields, however this would also create some dead area in the device. The current design already puts the rails very close to the edge of the PMN-PT material. Furthermore, it should be noted that the region between the interdigitated electrodes has some high field regions near the electrodes and a diagonal shape to the high field region is observed. Figure 4.6(b) is a camera image of the experimental device after poling with 250 V (2.5 kV/cm), showing a change in transmittance after poling that is consistent with the high-field regions predicted in the mid-plane by COMSOL. Figure 4.6(c) shows the high-field regions in the top plane of the PMN-PT sample to be near the electrodes and have a triangular shape between the electrode edge and opposing rail gap. Observing the sample under a microscope and limiting the depth of focus to the top plane confirms this phenomenon experimentally

as seen in Figure 4.6(d). The excellent agreement between the COMSOL simulated high electric field regions and experimentally observed change in optical transmission confirms the COMSOL model is accurately simulating the electric field.

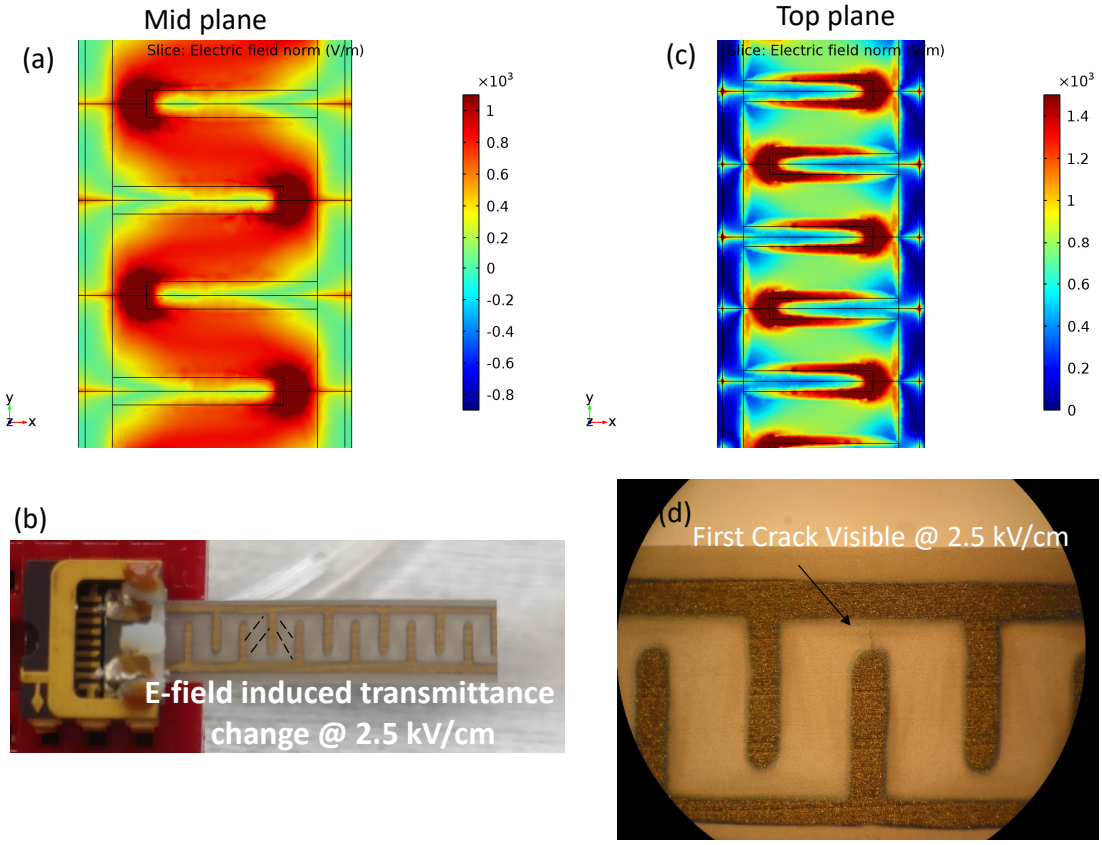

Figure 4.6. (a) COMSOL simulation of the electric field at 1 V applied to the electrodes scaled to show the regions of high electric field at the mid plane. (b) Camera image after poling at 250 V; the transmittance of the PMN-PT is slightly changed and the same high-field regions are visible. (c) COMSOL simulation of the electric field highlighting high field region at the top plane. (d) Camera image under a microscope with the depth of field limited to the top plane showing reduced light transmission in areas predicted to have high fields by the COMSOL simulation. One visible crack is was found across the entire sample.

4.5 Magnetoelectric Magnetic Sensing

Magnetoelectric devices are fabricated from 4 mm × 15 mm or 30 mm long, 400 μm thick PMN-PT crystals and magnetically poled and aligned Metglas 2605SA1. The

magnetoelectric sensitivity is reported for these devices instead of the magnetoelectric coefficient. This is because the magnetoelectric coefficient is fundamentally normalized to the electric field in the piezoelectric, which is not simple to determine in interdigitated devices. Furthermore, the sensitivity is arguably a more important metric since it ultimately determines sensing capability. Figure 4.7(a) shows the magnetoelectric sensitivity for the 15 mm long monolithic PMN-PT device for 1 layer of Metglas on each side (50 μm total) and 3 layers on each side (50 μm total). Some authors have reported improvements by optimizing the Metglas to piezoelectric volume ratio. However, simulations in chapter 3 show that flux concentration is worse for thicker films of Metglas. This explains why the 3 layered magnetoelectric device performed poorly as compared to the single layered device. This is also evident from the increased DC magnetic field required to bias the device confirming the flux concentration is worse. The sensitivity is 0.9 V/mT for the single layer device and 0.7 V/mT for the 3 Metglas layered 15 mm long device. A longer 30 mm monolithic PMN-PT device is also fabricated with 1 Metglas layer on each side and the sensitivity improved to 1.3 V/mT.

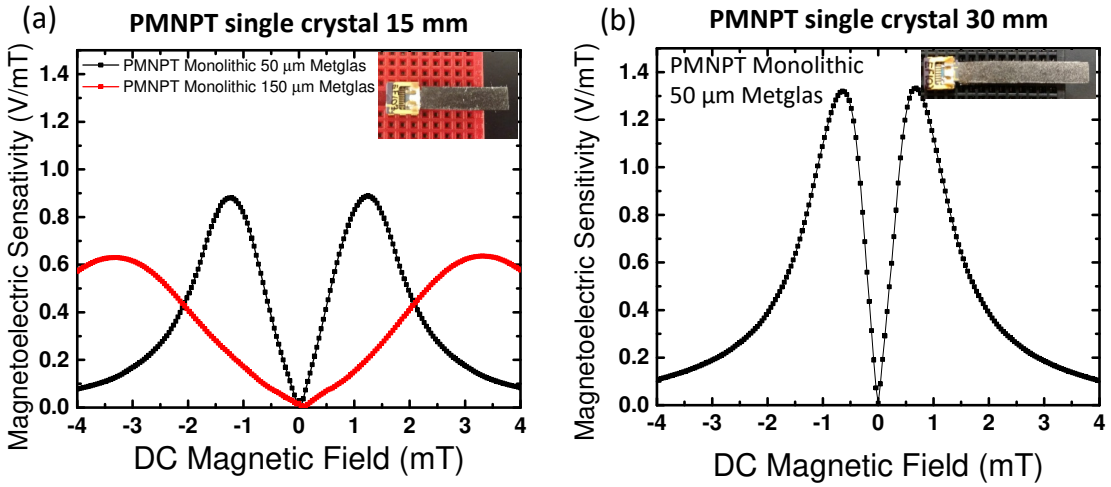

Figure 4.7. (a) 4 mm × 15 mm, 400 μm thick monolithic PMN-PT magnetoelectric device with 1 (50 μm) layer and 3 (150 μm) layers of Metglas on each side. The single layer device performed better with a 0.9 V/mT sensitivity compared to the 3 layer device which has 0.7 V/mT sensitivity due to the reduced flux concentration. (b) A longer 30 mm device is made, which demonstrated better performance of 1.3 V/mT due to a larger sensing area and increased flux concentration effect. All testing is done at 20 Hz

The MFC based device has several advantages. The PMN-PT in the MFC is 180 μm

thick, compared to the 400 μm thick monolithic devices. The epoxy matrix provides mechanical compliance to the structure and helps reduce cracking and damage from handling. Also, the non-conductive epoxy matrix helps the poling maintain a more ideal direction by limiting electric field strength in the short axis of the device. However, the polyimide interface reduces coupling and the epoxy matrix contributes to dead space in the device. The effective d_{33} achievable with interdigitated electrodes is lower than what is realizable with parallel plate poling [133]. Figure 4.8 shows the magnetic sensitivity of the 27 mm $\times$ 3 mm $\times$ 180 μm thick MFC based device with 1 layer of Metglas (50 μm total thickness) showing a large improvement in sensitivity of 6.5 V/mT compared to the monolithic sample. The sensitivity of the d_{31} device fabricated in chapter 3 is 1.1 V/mT is also plotted for comparison. As with the monolithic case, adding layers of Metglas reduces the flux concentration and reduces performance.

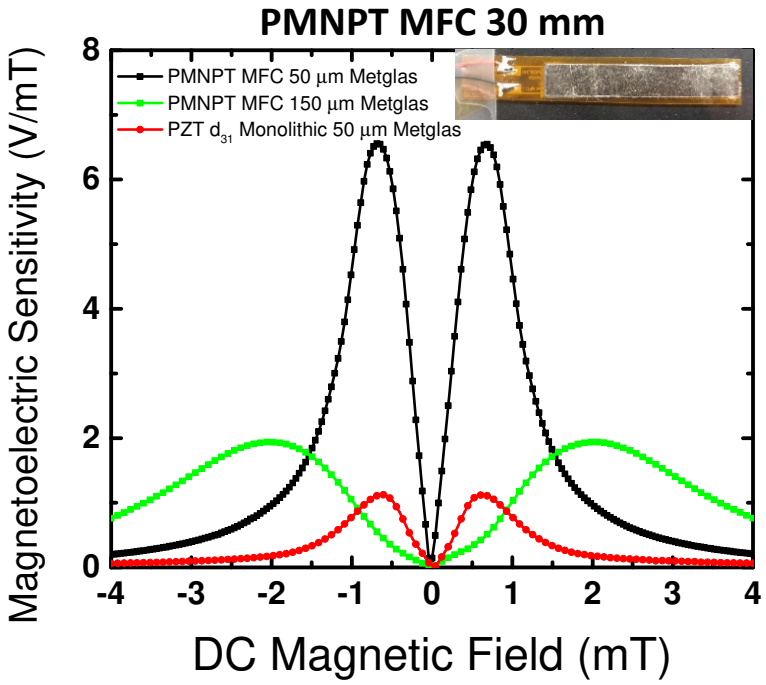

Figure 4.8. Magnetic sensitivity of the 27 mm $\times$ 3 mm $\times$ 180 μm thick MFC based device with 1 layer of Metglas (50 μm total thickness) shows a large improvement compared to the d_{31} PZT device. The reduced flux concentration from adding more Metglas layers is evident when with the PMN-PT device with 3 layers (50 μm total thickness).

The limit of detection and noise characteristics, measured using a Stanford Research SR760 spectrum analyzer, of the d_{33} PMN-PT MFC based magnetoelectric device

are evaluated. Figure 4.9(a) compares the noise characteristics of the d_{31} PZT device using as-cast Metglas, the optimized d_{31} PZT device using domain aligned Metglas and the PMN-PT-MFC device with domain aligned Metglas. The PMN-PT-MFC device with domain aligned Metglas has the best sensitivity and as a result the best magnetic equivalent noise floor of approximately 200 pT/$\sqrt{\text{Hz}}$. Figure 4.9(b) compares the limit of detection at 20 Hz using PZT d_{31} optimizations done in chapter 3 with the PMN-PT-MFC device with 1 layer of Metglas built in this chapter. The limit of detection decreased further to 50 pT at 20 Hz by taking advantage of the higher piezoelectric coefficient of PMN-PT.

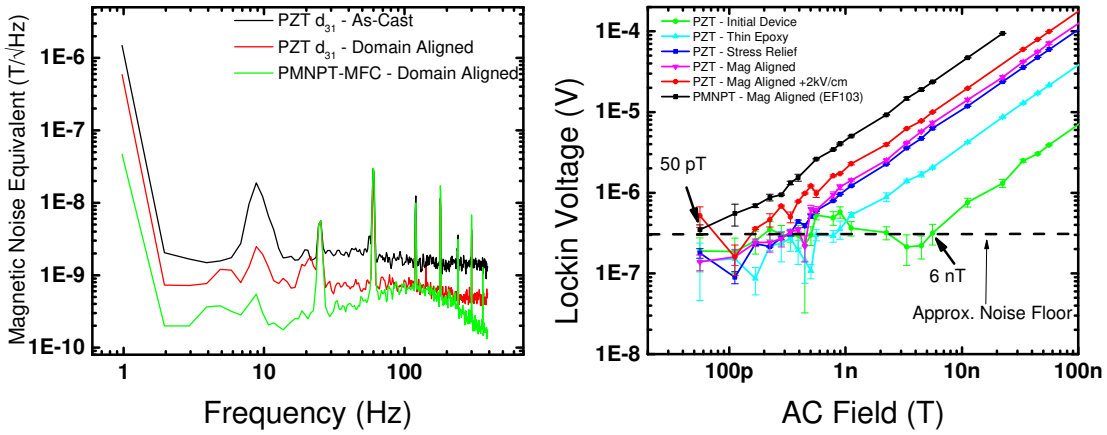

Figure 4.9. (a) Magnetic noise equivalent noise spectrum for the d_{31} PZT using an as-cast Metglas film and a d_{31} PZT using a magnetic domain aligned Metglas film with the d_{31} PMN-PT-MFC with magnetic domain aligned Metglas. The PMN-PT-MFC device has the best sensing magnetic noise floor of approximately 200 pT/$\sqrt{\text{Hz}}$ (b) The limit of detection evaluated at 20 Hz shows the PMN-PT-MFC device has the lower limit of detection at 50 pT compared to the d_{31} PZT devices.

4.6 Conclusion

A select set publications detailing various performance achievements and configurations over the last 20 years of laminate magnetoelectric magnetometer development is shown in table 4.1. Early work on laminate magnetoelectric development used terfenol-D and galfenol based magnetostriction materials. However, the high DC magnetic bias point of those materials and the relatively low magnetostriction coefficient compared to Metglas 2605SA1 and other magnetostrictive amorphous metallic glasses has resulted in less magnetoelectric magnetometer publications using terfenol-D and galfenol. The most

sensitive magnetoelectric magnetometers use PMN-PT over PZT, due to the higher d_{33} coefficient in PMN-PT. The limit of detection has improved from hundreds of pT to single digit and tens of pT for modern magnetoelectric magnetometers. Likewise, the magnetoelectric coefficient has increased from single digit $\mathrm{MV}/(\mathrm{m}\cdot\mathrm{T})$ to 52 $\mathrm{MV}/(\mathrm{m}\cdot\mathrm{T})$ in the most sensitive devices [48].

In this work, using an annealed and domain aligned Metglas 2605SA1 ribbon as the magnetostrictive phase, an impressive 9.7 $\mathrm{MV}/(\mathrm{m}\cdot\mathrm{T})$ was achieved for an PZT device in d_{31} configuration and 18.6 $\mathrm{MV}/(\mathrm{m}\cdot\mathrm{T})$ for a PMN-PT MFC device in d_{33} configuration. This is lower than the 52 $\mathrm{MV}/(\mathrm{m}\cdot\mathrm{T})$ achieved by Wang et al., despite having an extraordinarily large magnetostriction coefficient of 79.3 $\frac{\mu\mathrm{m}}{\mathrm{m}\cdot\mathrm{mT}}$, compared to 40 $\frac{\mu\mathrm{m}}{\mathrm{m}\cdot\mathrm{mT}}$ reported by Wang et al. The lower magnetoelectric coefficient may be due to several factors. First the Metglas used in [48] was 80 mm long, compared to 30 mm in this work, and flux concentration improves for longer Metglas ribbons. Second, the thinner 0.1 mm thick PMN-PT used by Wang et al. experiances more strain than the 0.18 mm thick PMN-PT used in this work. Finally, the larger area PMN-PT MFC used by Wang et al. may be producing more charge/voltage due to the increased charge collection area.

Table 4.1. Comparison of some previous magnetoelectric devices and their configuration. Where possible the electrode spacing is used to determine the sensitivity or vice versa. N/R means not reported.

	Magnetostrictive			Piezoelectric		Magnetoelectric					
Year	**Material**	**Dimensions** [$\phi \times$ T] or [L×W×T]	$\partial\lambda/\partial B$ $\left(\frac{\mu\mathrm{m}}{\mathrm{m}\cdot\mathrm{mT}}\right)$	**Material**	**Dimensions**	**Sensing Mode**	**Electrode Spacing (cm)**	α_{me} $[\mathrm{MV}/(\mathrm{m}\cdot\mathrm{T})]$	**Sensitivity** (V/mT)	**LOD**	**Ref.**
2001	Terfenol-D	ϕ: 12.7 × 1 mm		PZT	ϕ: 12.7 × 0.5 mm	d_{31}	0.05	4.7	2.3	N/R	[61]
2005	Fe-20%Ga	12.7 mm × 6 mm × 1 mm		PMN-PT	14 mm × 6 mm × 1 mm	d_{33}	0.7	1	7	120 pT @ 1 kHz	[134]
2006	FeBSiC (Metglas)	100 mm × 7 mm × 25 µm	40	PZT-5A	30 mm × 7 mm × 0.1 mm	d_{33}	0.05	22	1.1	N/R	[107]
2006	Terfenol-D	14 mm × 6 mm × 1.2 mm		PZT	16 mm × 6 mm × 2 mm	d_{33}	0.8	1.3	0.66	20 pT @ 1 Hz	[135, 136]
2010	Metglas 2605SA1 & Terfenol-D	Met.: 15 mm × 15 mm × 0.2 mm Terf.: 13 mm x 13 mm 4 mm		PMN-PT	10 mm × 10 mm × 1 mm	d_{31}	0.1	5	5	500 nT	[137]
2011	Metglas	80 mm × 10 mm × 25 µm (12 layers)		PZT (MFC)	40 mm × 10 mm × 0.1 mm	d_{33}	0.085	8.5	8	20 pT @ 10 Hz	[138]
2011	Metglas	80 mm × 10 mm × 25 µm	22	PMN-PT (MFC)	40 mm × 10 mm × 0.1 mm	d_{33}	0.10	52	52	5 pT @ 1 Hz	[48]
2011	Metglas (annealed)	80 mm × 10 mm × 25 µm		PZT (MFC)	42 mm × 10 mm × 0.2 mm	d_{33}	0.085	7.2	6.1	-	[77]
2012	Metglas	80 mm × 10 mm × 25 µm (6 layers)		PMN-PT (MFC)	40 mm × 10 mm × 0.2 mm	d_{33}	N/R	35	N/A	7 pT/$\sqrt{\mathrm{Hz}}$ @ 1 Hz	[139]
2013	Metglas	80 mm × 10 mm × 25 µm (6 layers)		PZT (MFC)	40 mm × 10 mm × 0.1 mm	d_{33}	0.18	9.7	17.5	-	[140]
2017	Metglas 2605SA1 (annealed)	30 mm × 5 mm × 25 µm	79.3	PZT-5A	13 mm × 3 mm × 0.2 mm	d_{31}	0.02	9.7	1.9	150 pT @ 20 Hz	this work
2017	Metglas 2605SA1 (annealed)	30 mm × 5 mm × 25 µm	79.3	PMN-PT (MFC)	27 mm ×4 mm × 0.18 mm	d_{33}	0.035	18.6	6.5	50 pT @ 20 Hz	this work

In conclusion integrating a PMN-PT d_{33} macro fiber composite piezoelectric greatly improved the magnetic sensitivity from 1.1 V/mT to 6.5 V/mT. The electric field profile produced by the interdigitated electrodes produces non-uniform poling and deadspaces in the piezoelectric, which do not contribute to sensing. The macro fiber composite limits electric fields along the short axis of the piezoelectric and reduces cracking due to the pliable epoxy matrix enabled thinner piezoelectric films to be used and handled.

Ultimately the magnetic noise floor is approximately 200 pT/$\sqrt{\text{Hz}}$ between 5 Hz and 300 Hz. The limit of detection measured by a lock-in amplifier is 50 pT at 20 Hz.

Chapter 5

Passively-Powered Wireless Micromachined Quartz Magnetoflexoelastic Magnetometer

In this chapter a passively-powered wireless magnetometer based on the magnetoflexoelastic effect is demonstrated and the wireless interaction is incorporated as a component of the Butterworth-van-Dyke (BVD) model as a resistive loss element.

Highly sensitive, wirelessly powered, and maintenance-free sensors are of great interest to the biomedical, geological, hazardous environment, and traffic control communities. The wireless coupling is achieved using coupled near-field resonant loop antennas, which excite the high Q-factor (~6600) of a micromachined quartz resonator. Magnetostrictive curves are acquired both wired and wirelessly at distances up to 45 mm to confirm the phenomenon is magnetoflexoelastic in nature. A 49.1 Hz/Oe sensitivity was achieved in wireless operation and the ultimate detectable limit was 7 μT at 0.5 Hz.

5.1 Introduction

High Q-factor quartz crystal resonators (QCR) have been demonstrated as highly sensitive (bio)chemical, infrared, and physical sensors [141, 142, 143]. The surface of quartz can be modified to adsorb a wide variety of substances resulting in viscosity and mass changes which influence its resonance frequency characteristics. The frequency and Q-factor changes can be used to determine viscoelastic properties of adsorbed substances using

detailed analysis using Butterworth-van-Dyke (BVD) model or in the case of thin, rigid, elastic layers the adsorbed mass using Sauerbrey's equation [144]. Furthermore, the temperature insensitivity of AT and BT cut quartz substrates allow them to be operated at room temperature for low noise measurements. Recent efforts have developed a magnetoflexoelastic quartz magnetometer with a 79 nT limit of detection using a 10 Hz signal [51]. Hatipoglu et al. predicted that a limit of detection of 28 pT is possible for 180 nm thick quartz, making it relevent for biomagnetic measurements. Furthermore, a passively powered implantable magnetic sensor may be placed close to the biomagnetic source and not require a low limit of detection. This phenomenon has been modeled by combining Lee's theory and magnetostrictively induced Euler-Bernoulli beam bending theory [51].

Thompson et al. first described wireless interaction with an AT-cut QCR and measured protein adsorption wirelessly [145]. This was accomplished without electrodes by exciting an electric field from a spiral coil into the piezoelectric and then detecting the resonant signal from the quartz. Ogi et al. demonstrated 170 MHz electrodeless quartz operation using a similar mechanism [146]. However, both implementations require high power amplifiers and the antenna was just 30 μm from the QCR. Line antennas were used to increase this gap to larger than 3 mm [147]. Long range wireless communication with electronics which interact with QCRs has been exploited before [148], however this requires actively powering the QCR and its electronics locally.

This work demonstrates the wireless operation of a magnetoflexoelastic QCR magnetometer. The magnetometer is made of a micromachined quartz resonator plate with one of its faces coated with magnetostrictive Metglas ($Fe_{85}B_5Si_{10}$) thin film. The resulting quartz-Metglas unimorph plate is clamped at one end and free on all other sides. The strain generated in the magnetostrictive layer, in response to externally applied magnetic field, is elastically coupled to the QCR and thus results in an out-of-plane bending of the laminate plate structure. This results in a shift of the QCR resonance frequency and consequently changes its at-resonance admittance characteristics and is the principle of operation of the quartz magnetoflexoelastic magnetometer. Since the QCR resonates at RF frequencies such that remote magnetic field detection can be achieved without any actively powered electronics on the magnetometer. Resonance is remotely excited in the magnetometer through a coupled loop antenna. The limit of detection is evaluated for this device and the wireless loss is modeled as a component in the BVD model.

General	Definition	Electrical	Mechanical	Fluidic	Thermal
Effort (e)	$e = \frac{dp}{dt}$	Voltage, V	Force, F	Pressure, P	Temp. Difference, ΔT
Flow (f)	$f = \frac{dx}{dt}$	Current, I	Velocity, V	Vol. flow rate, Q	Heat Flow
Displacement (x)	x	Charge, Q	Displacement, x	Volume, V	Heat, Q
Momentum	p (t)	-	Momentum, p	Pressure Momentum, Γ	-
Resistance (R)	R=e/f	Resistor, R	Damper, b	Fluidic Resistance, R	Thermal Resistance, R
Capacitance (C)	C=e/x	Capacitance, C	Spring, k	Fluid Capacitance, C	Heat Capacity, mcp
Intertance (L)	$L = e/\frac{df}{dt}$	Inductor, L	Mass, m	Inertance, M	-
Node Law	$\sum f = 0$	KCL	Continuity of space	Mass conservation	Heat energy conservation
Mesh Law	$e = L\frac{df}{dt}$	KVL	Newton's 2nd law	Pressure is relative	Temperature is relative

Table 5.1. Mechanical, fluidic, thermal and electrical analogs. Adapted from [150]

5.2 Theory

Mechanical, fluidic and thermal effort-flow relations can be analogously modeled as electrical components as shown in table 5.1. In general terms, flow is the displacement per unit time and effort is momentum per unit time. This transformation can lead to a more intuitive representation of the physics and the ability lump many energy domains into one. This allows one to model the electrical components of quartz along with the mechanical components. This flexibility has helped enabled the commercial success of the quartz crystal microbalance which provides accurate thickness monitoring [149] for in many deposition systems. Furthermore an extensive amount of research has been conducting using quartz for chemical, biological, physical (viscoelastic, temperature, mass, magnetic fields, etc) sensors have been demonstrated [143, 141, 51].

5.2.1 Butterworth-van-Dyke Model

A piezoelectric plate can be modeled as a 3-port Mason circuit which has electrical and mechanical components, which are coupled by a transformer. Furthermore the model has 2 mechanical ports allowing for a substrate and electrode loading to be included into the model. If the piezoelectric slab is monolithic with the electrodes only in contact with air on both sides, a more convenient equivalent circuit may be used [144]. This circuit must have an electrical capacitance C_0 and be mechanically described as a having a damper component with a resistance R_m, a spring component with capacitance C_m and mass component inductance L_m. The circuit must also meet the requirement to have a series and parallel resonance. The equivalent circuit used to achieve these criteria is seen in figure 5.1 and is known as the Butterworth-van-Dyke model [144].

The mechanically analogous electrical components can be related back to the acoustic properties of the quartz and are detailed below in (5.1), (5.2), and (5.3) for R_m, L_m

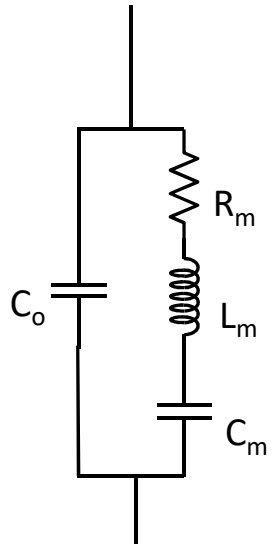

Figure 5.1. Butterworth-van-Dyke equivalent circuit model of a quartz resonator.

and C_m respectively. ω is the excitation frequency, ω_r is the resonance frequency, ρ is density of the piezoelectric, η is the acoustic viscosity, *A* is the surface area of the resonator, v_a is the particle velocity, c^D is the stiffness constant at zero displacement, *e* is the piezoelectric constant and ε^S is the dielectric permittivity. A detailed derivation can be found in [144]

$$\begin{aligned} R_m &= \frac{\pi\eta\varepsilon_r\varepsilon_0}{8k_t^2\rho A\omega v_a} \\ k_t^2 &= \frac{e^2}{\varepsilon^S c^D} \end{aligned} \tag{5.1}$$

$$\begin{aligned} L_m &= \frac{\pi^3 v_a}{8k_t^2\omega_r^3\varepsilon_r\varepsilon_0 A} \\ \omega_r &= \sqrt{\frac{1}{L_m C_m}} \end{aligned} \tag{5.2}$$

$$C_m = \frac{8}{\pi^2}k_t^2 C_0 \tag{5.3}$$

The series resonance condition occurs when L_m and C_m reactance cancel each other, defined by (5.4). Similarly, the parallel resonance condition occurs when the reactance of the L_m and C_m leg cancel out the reactance of the C_0 of the circuit as seen in (5.5). The Q for a oscillating circuit is defined as $Q = \frac{v_a \rho}{\omega \eta}$, which from the BVD model operating at series resonance can be re-written as (5.6).

$$f_s = \frac{1}{2\pi\sqrt{L_m C_m}} \tag{5.4}$$

$$f_p = \frac{1}{2\pi\sqrt{\frac{L_m C_m C_o}{C_m + C_o}}} \tag{5.5}$$

$$Q = \frac{2\pi L_m f_o}{R_w} \tag{5.6}$$

5.2.2 Force Frequency Effect Coupled with Magnetostriction

Quartz is a piezoelectric which exhibits a high *f-Q* product and room temperature compensated cuts like AT-cut and BT-cut offer high stability. The high quality factor (Q) and frequency (f) stability make are why Quartz has been widely use for precision timing application, clocking for electronics [151] and is found in nearly every commercial wrist watch. The force-frequency effect was first confirmed by Bottom in 1947 [152] and was generally considered a non-ideality in terms of time keeping. Later it was exploited for sensing applications [153, 154] and well quantified by EerNisse et al., who performed variational calculations on doubly rotated quartz resonators (AT, FC, IT and X cuts) to determine the force-frequency effect constants [155].

To analytically couple the force-frequency effect with the magnetostriction phenomenon Hatipaglu et al. [51] integrated Lee and Markenschoff's model of quartz frequency shift [156] due to force-frequency effect with Devoe's et al. model of unimorph tip deflection [103] with the magnetostriction material acting as the active element instead of the piezoelectric.

The cantilever structure used in this work is illustrated in figure 5.2. The electrodes are circular but focused ion beam (FIB) cutting is used to define a square shaped cantilever, illustrated as the white lines in figure 5.2. The structure can not bend unless it is released and no magnetic sensitivity was observed before the FIB cut. The resonance in quartz is confined to the center of the electrode due to energy trapping, with energy decaying

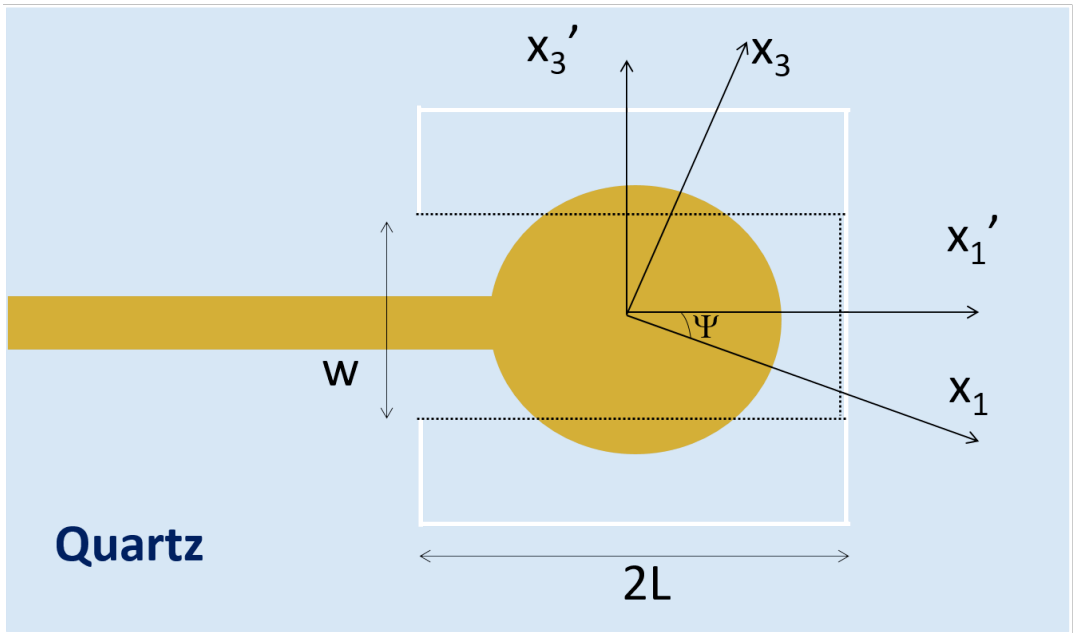

Figure 5.2. Illustration of the fabricated quartz cantilever. The gold regions are the electrodes and the white lines are the release points for the quartz. The dashed lines are a guide for the eye to help define the cantilever region of interest. The width of the cantilever, *W* and the half length (*L*) are labeled.

with a Gaussian shape towards to edges of the electrodes. Therefore the device area is estimated to be the shape of a rectangle shown as the dash lines in figure 5.2. A detailed fabrication process is discussed in 5.3.1 and appendix A. The cantilever deflection (δ_z) is calculated from the stress induced by the Metglas/quartz unimorph using 5.7, where *t* is the thickness *C*, is the elastic modulus, λ_m is the magnetostriction deflection in ppm. The subscripts *m* and *q* refer to the magnetostrictive layer and quartz layer, respectively. The *Y* subscript refers to the appropriate modulus tensor.

Next, the δ_z is used to calculate the equivalent point load (*P*) on the cantilever using (5.8), where *L* is the **half** length, *W* is the width, and *I* is the second moment of inertia.

$$\delta_z(L) = \frac{3t_m t_q (t_q + t_m) C_{Yq} C_{Ym} (2L)^2 \lambda_m}{C_{Yq}^2 t_q^4 + C_{Yq} C_{Ym} (4t_q^3 t_m + 6t_q^2 t_m^2 + 4t_q t_m^3) + C_{Ym}^2 t_m^4} \tag{5.7}$$

$$\delta_z = \frac{P(2L)^3}{3C_{Yq}I}$$
$$I = \frac{(2L)W^3}{12} \tag{5.8}$$

Once the point load is known, the stress components (T) can be calculated. The non-zero components have been determined by Wang et al [157] and are shown in (5.9). It should be noted that there is an azimuthal angular component ψ, the angle between the crystallographic axis and the applied force.

$$\begin{aligned}
T_4^{(0)} &= -P\sin(\psi)/w \\
T_6^{(0)} &= -P\cos(\psi)/w \\
T_1^{(1)} &= P\cos^2(\psi)(L - \cos(\psi)x_1 - \sin(\psi)x_3)/w \\
T_3^{(1)} &= P\sin^2(\psi)(L - \cos(\psi)x_1 - \sin(\psi)x_3)/w \\
T_5^{(1)} &= P(L\cos(\psi)\sin(\psi) - \cos^2(\psi)\sin(\psi)x_1 - \cos(\psi)\sin^2(\psi)x_3)/w
\end{aligned} \tag{5.9}$$

Next, the strain (S) is calculated from from the stress using (5.10). Finally, the change in resonance frequency ($\frac{\Delta f}{f_0}$) is calculated using (5.11). The force frequency effect depends on the zeroth and first order strains and the first order strain gradients, via the second and third order elastic stiffnesses.

$$T_{ij} = C_{ijkl}E_{kl} + 0.5C_{ijklmn}S_{kl}S_{mn} \tag{5.10}$$

$$\begin{aligned}
\frac{\Delta f}{f_0} &= \frac{1}{2C_{66}}\left(2C_{66}E_1 + C_{166}S_1 + C_{266}S_2 + C_{366}S_3 + C_{466}S_4\right) \\
&-\frac{L^2/\sqrt{3}}{\pi C_{66}}\left(C_{165}S_{5,1}^{(1)} + C_{561}S_{1,3}^{(1)} + C_{563}S_{3,3}^{(1)}\right)
\end{aligned} \tag{5.11}$$

5.2.3 Wireless Interaction

The coupling effect demonstrated in this chapter to wirelessly probe the QCR magnetometer relies on near field antenna interactions. The difference between far field and near field area is a function of radiation wavelength (λ) and distance. The far field is defined as 2λ and further from the radiation source. The a transition region between 1λ and 2λ from the antenna. The near field is defined as the distance within 1λ of the antenna. The near field is further split into a reactive region ($\frac{\lambda}{2\pi}$) and a radiative region between $\frac{\lambda}{2\pi}$ and 1λ. For this experiment the frequency used is approximately 86 MHz, meaning the near field reactive region is approximately 55 cm.

In the reactive region electromagnetic waves are reactive to the surrounding medium and the field is sensitive to electromagnetic absorption in the region. The origin of this can be understood by considering the self-capacitance and self-inductance of the antenna. For example, when current moves in an antenna it generates a magnetic field, and when the current reverses the magnetic field changes direction inducing a voltage in the antenna and returns the stored magnetic energy in a regenerative manner. Similarly, electrons building up in one section of the antenna results in an electric field from the antenna's self-capacitance. When the electrons oscillate to another section of the antenna the e-field assists the motion, again returning energy. If there is a nearby electromagnetic absorber not all of the energy is returned (or extra energy is returned) to the antenna, producing an energy change in the primary antenna that is seen as a change in impedance by the generator. This changes the matching characteristics of the antenna, resulting in a change in reflected power.

The electric field (*E*) and magnetic field (*H*) as a function of distance (*D*) is given by (5.12) and (5.13), respectively:

$$E_{\varphi} = \eta\beta^2(IA)\sin\theta\left(1+\frac{1}{j\beta D}\right)\frac{e^{-j\beta D}}{4\pi D} \tag{5.12}$$

$$H_{\varphi} = -\beta^2(IA)\sin\theta\left(1+\frac{1}{j\beta D}-\frac{1}{\beta^2 D^2}\right)\frac{e^{-j\beta D}}{4\pi D} \tag{5.13}$$

where $\eta = \sqrt{\mu/\varepsilon}$ and $\beta = \frac{\omega}{\sqrt{\mu\varepsilon}}$, μ is the permeability of the medium and ε is the permittivity of the medium, *I* is the current, *A* is the area of the loop and θ is the phase. In the near field the $E \propto D^{-2}$ and $H \propto D^{-3}$ where as in the far field region the higher order terms in the parenthesis can be ignored and $E \propto D^{-1}$ and $H \propto D^{-1}$. The *E* and *H*

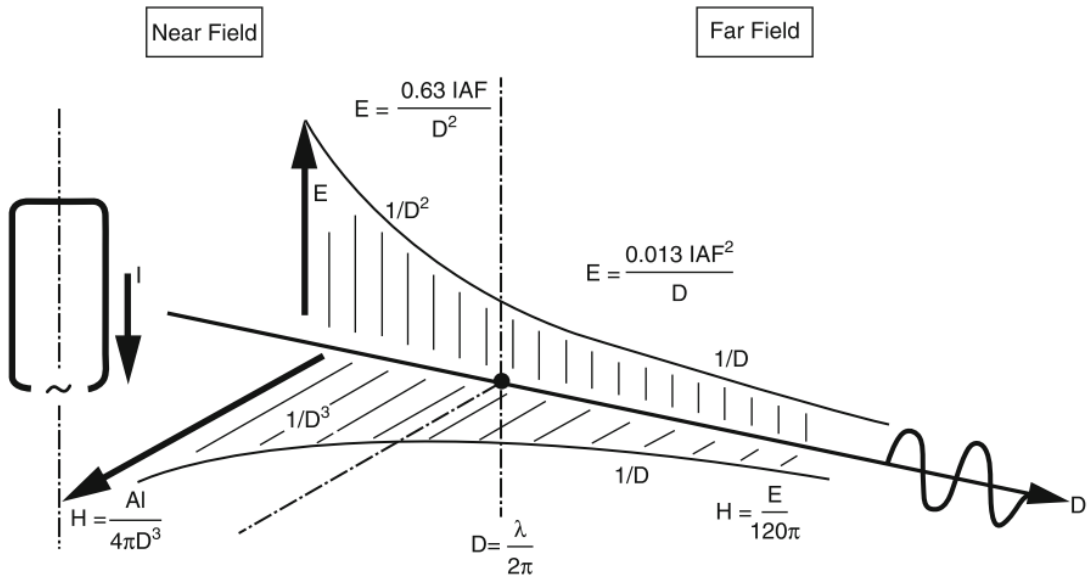

Figure 5.3. Illustration of the E and H fields in the near and far field regions for a perfect loop conductor. In the near field the $E \propto D^{-2}$ and $H \propto D^{-3}$ where as in the far field $E \propto D^{-1}$ and $H \propto D^{-1}$. [158]

fields across the near and far field are illustrated in figure 5.3.

5.3 Experimental Setup

5.3.1 Device Fabrication

The sensor is fabricated from a 100 μm thick AT-cut quartz substrate as shown in figure 5.4(a), which is micromachined to form a 500 μm x 500 μm cantilever on 19 μm thick plate QCM. Thinning of the QCM area is achieved by Ar/SF_6 reactive plasma etching using 15 μm nickel as a hard mask as illustrated in figure 5.4(b-c). A 20/100 nm Cr/Au signal electrode is evaporated and patterned onto the top surface of the QCM as seen in figure 5.4(d). Next, a ground electrode of 20/100 nm Cr/Au is evaporated and the

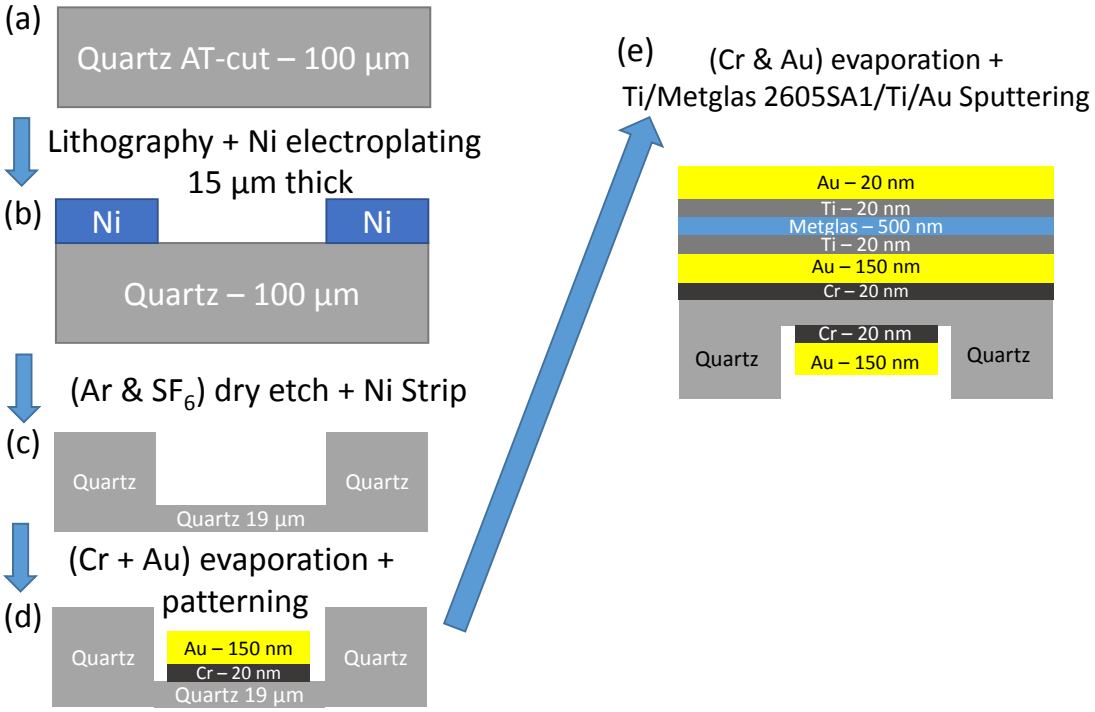

Figure 5.4. (a) Starting with 100 µm AT cut quartz, the a metallic seed layer is deposited on the quartz (not shown) and (b) lithographically patterned and electroplated with 15 µm thick Ni and the photoresist is stripped away. (c) An Ar & SF_6 dry etch is used to thin the quartz down to 19 µm using the Ni as a hard mask, followed a strip of the hardmask. (d) Cr/Au is evaporated and patterned using a spray coat lithography process followed by a wet etch and a photoresist strip. (e) The back electrode Cr/Au is evaporated and patterned using a lift-off lithography process, followed by mask-less sputtering of 20/300/20/20 Ti/Metglas ($Fe_{85}Si_5B_{10}$)/Ti/Au on the backside electrodes.

device is tested for resonance. Then, 20/300/20/20 nm Ti/Metglas ($Fe_{85}Si_5B_{10}$)/Ti/Au is deposited onto the bottom surface of the QCM sputter deposition resulting in the device illustrated in figure 5.4(e). The Metglas is in situ poled, parallel to the cantilever width axis, during sputter deposition using permanent magnets with a uniform field of 50 mT at the sample location. The sputtering target is a 25 µm thick, 25 mm diameter disc of Metglas 2605SA1. The 20 nm Au capping layer is used to prevent oxidation of the magnetic film in atmosphere and the Ti and Cr layers are to enhance stiction. Complete details of the fabrication process can be found in appendix A. Finally, the plate is released to form a cantilever using focused ion bean milling, as seen in the scanning electron micrograph in figure 5.5.

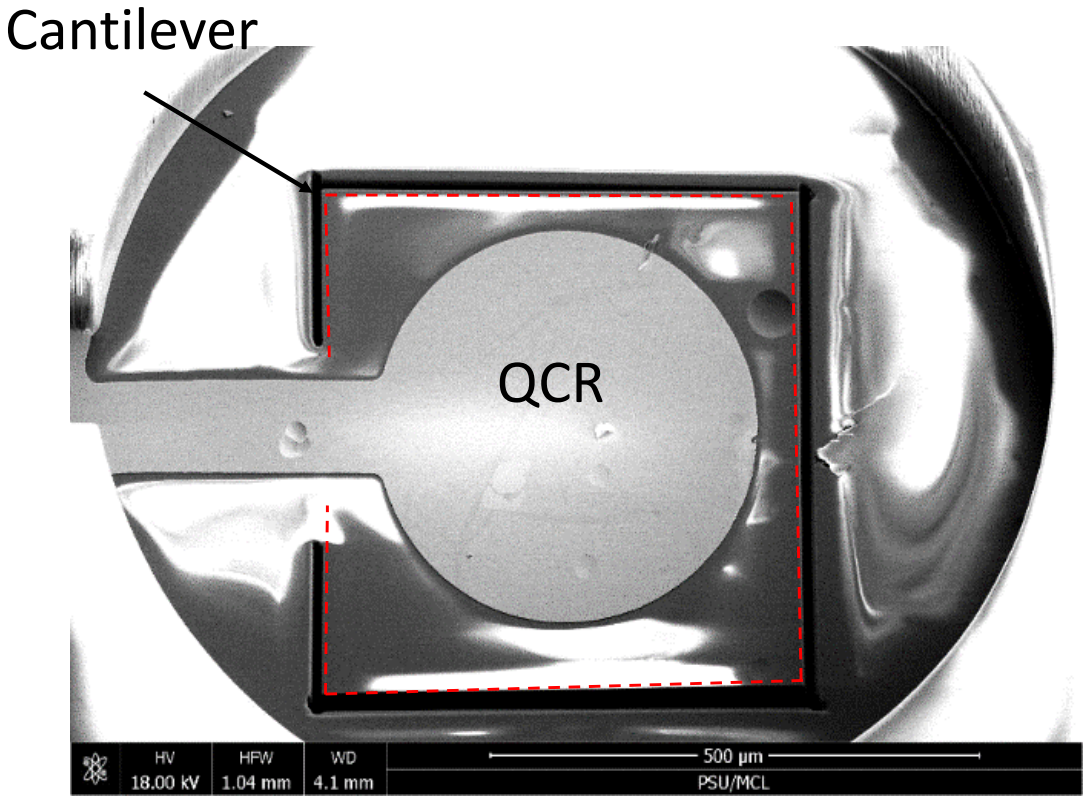

Figure 5.5. Scanning electron micrograph of the micromachined QCR. The red dashed lines indicate the FIB cut regions.

5.3.2 Wireless Setup

The device is packaged onto a patterned Rogers RO4360G2 substrate and connected to a 2.2 cm diameter near field coupling loop printed onto an FR4 substrate. An 11 cm diameter loop is used as the detector antenna with a series air-dielectric variable capacitor which is used to tune the resonant frequency of the loop such that it coincides with the fundamental resonance mode of the QCR. A camera image of the final constructed wireless device is shown in figure 5.6(a). An Agilent 8720ES vector network analyzer is used to excite the coupled antenna/QCR system and collect the reflection (S_{11}) parameter. A Lakeshore MH-12 Helmholtz coil and a GPIB controlled Agilent E3632A power supply are used to apply DC and low frequency AC magnetic fields to the sample during testing as is illustrated in figure 5.6(b). Wireless components were constructed by University of California, Los Angeles (UCLA) and wireless testing is performed at the University of California Los Angeles Near Field System Incorporated anechoic chamber.

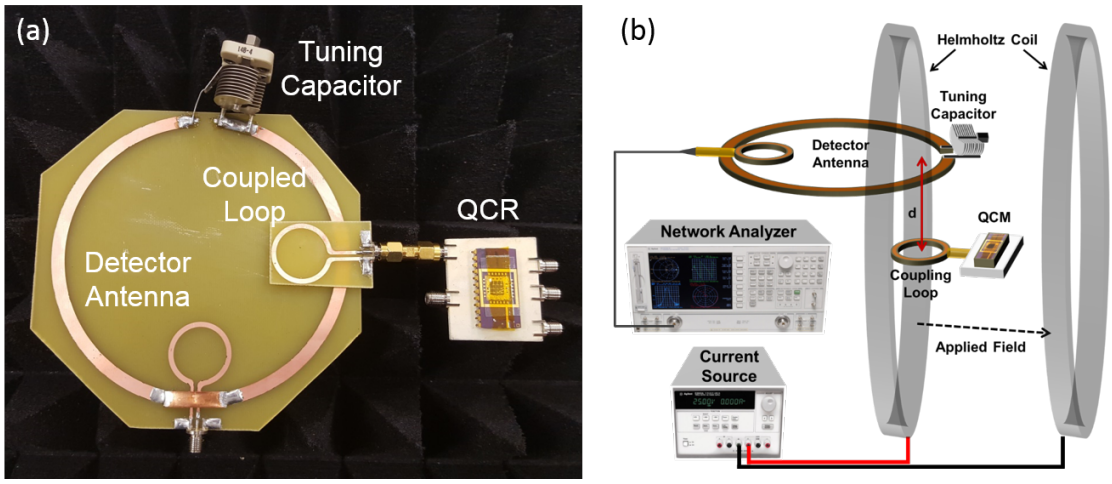

Figure 5.6. Schematic of wireless testing setup. (a) The packaged QCR is attached to the coupling loop. The detector antenna along with an air gap tuning capacitor is connected to an Agilent 8720ES network analyzer, which collects the S_{11} parameter. A Helmholtz coil powered by an Agilent E3632A current source magnetically stimulates the QCR. (UCLA)

5.4 Remote Magnetic Sensing

5.4.1 Wireless Coupling

The wireless interaction is determined by the antenna and the QCR. However, the QCR has a much higher quality factor than the broadband resonance of the antenna system, allowing the two to be easily distinguished from each other. The recorded S_{11} magnitude and phase of the coupled system, obtained from the detector antenna, are shown in figure 5.7. The S_{11} parameters demonstrate a relatively large bandwidth resonance originating from the resonant loop antenna superimposed onto a high Q-factor (6617) resonance from the thickness shear mode of the QCR centered at 86 MHz.

Next, the device response to a magnetic field is observed for the wireless (at 0 mm separation) and wired case. For the wired test, the network analyzer is connected via an SMA cable to the SMA port on the board housing the device, bypassing the antennas. Figure 5.8 shows the center frequency shift extracted from both wireless and wired connection methods over a range of applied DC magnetic fields from 0 to 19 Oe. The two interfaces are in good agreement and the characteristic magnetostriction curve associated with Metglas is clearly observable, confirming the phenomenon is magnetostrictive in

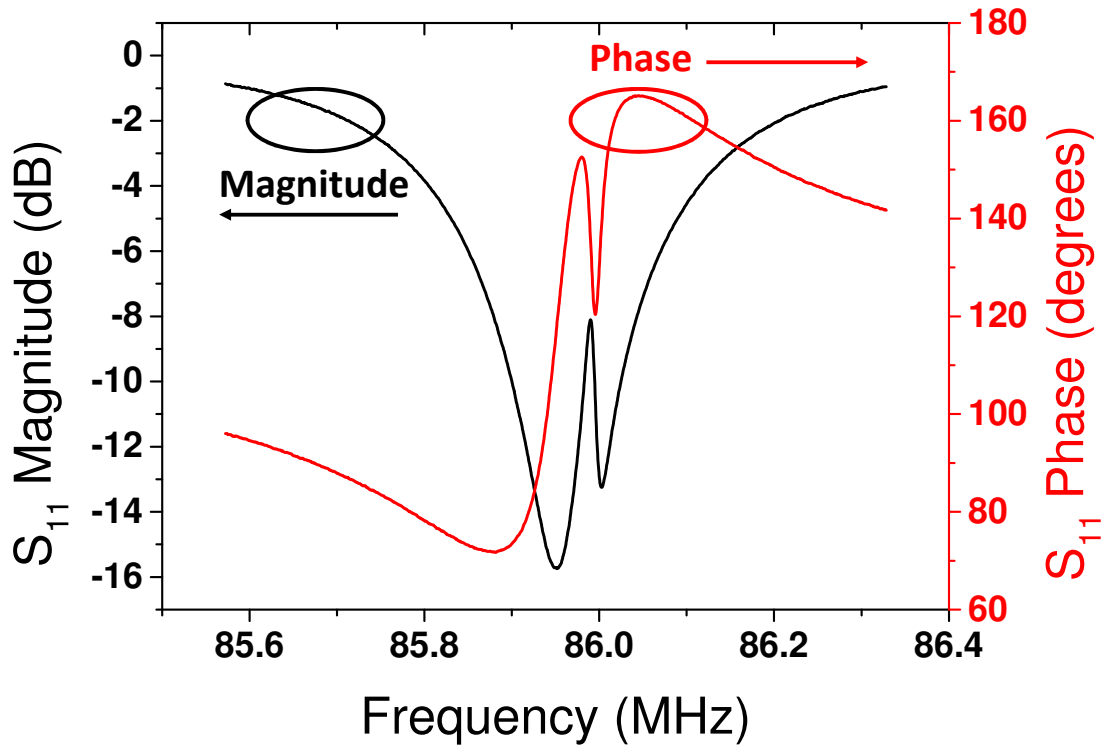

Figure 5.7. S_{11} magnitude and phase obtained wireless from the QCM and near field antenna. The large bandwidth loop resonance is superimposed on the 6617 Q-factor QCR 86 MHz resonance.

nature. The device has a sensitivity of 49.1 Hz/Oe in the linear region.

5.4.2 Separation Distance

To investigate the effect of separation distance between the antennas, the magnetostriction curve is measured for varying separation distances. Figure 5.9 shows the frequency shift measured wirelessly with detector antenna to coupling loop separation distances of 0, 7, 21 and 45 mm. The characteristic magnetostrictive behavior is distinctly observed at all distances. As the separation distance is increased, the magnitude and quality factor of the reflected QCM peak falls. Beyond separation distances of 45 mm, the 86 MHz peak observed in the reflected signal is no longer discernible from the measurement system noise. In this proof of concept the power on the transmitter was only 1 mW, and this can readily be increased by several orders of magnitude to increase the signal to noise ratio. In principle the near-field would extend to approximately 555 mm at 86 MHz defining the theoretical limit of this interface. These sort of separation distance limits are still

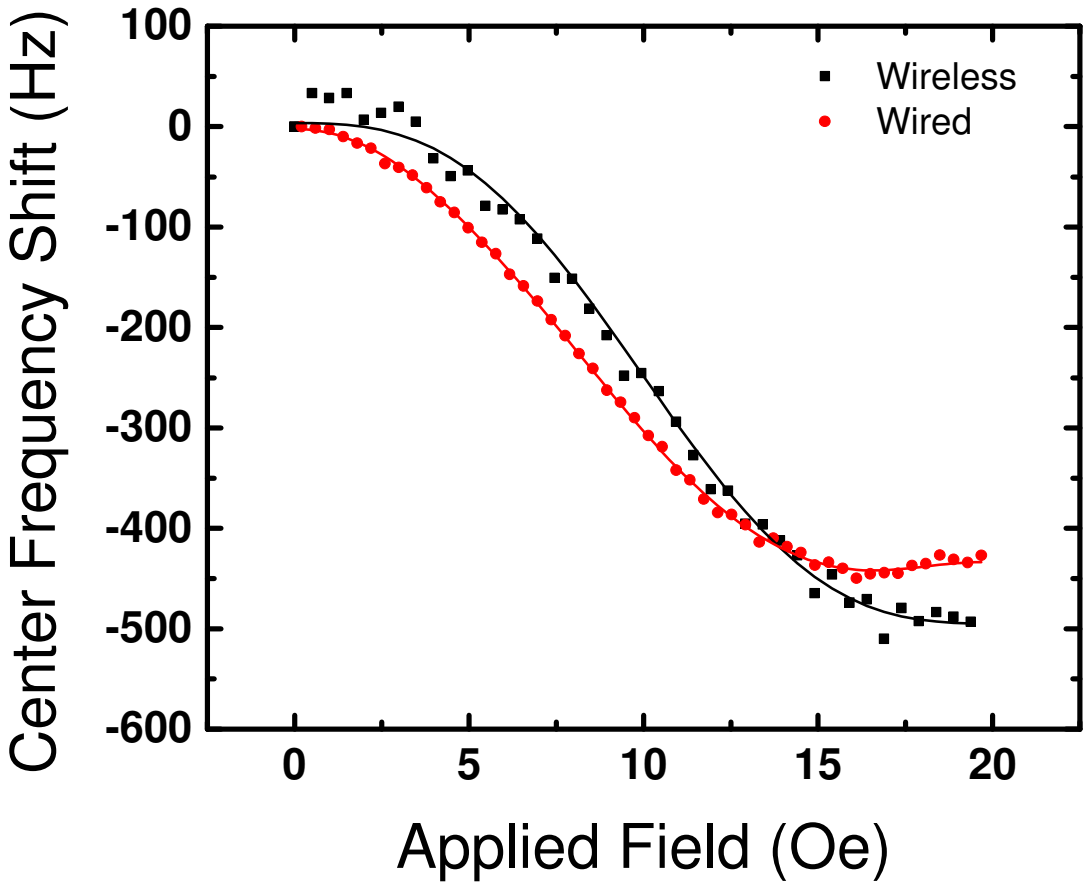

Figure 5.8. Measured center frequency shift for the wired and wirelessly (0 mm separation) obtained signal are in good agreement. Sensitivity in the linear region is approximately 49.1 Hz/Oe.

very useful, for example as an implantable sensor which would only need to pass a few millimeters of tissue to be used as a remote sensor and is a preferred alternative to having wires and ports imbedded in ones skin.

The S_{11} magnitude response near the QCR resonance frequency for separation distances 7, 21, and 45 mm shown in figure 5.10 shows that the resonance frequency does not change, however the magnitude of the reflected power from the QCR device decreases as the separation distance increases. The extra loss results in a decrease of the measured Q-factor, but does not fundamentally change the quartz mechanical Q-factor. To be implemented in the BVD model the wireless energy loss component must cause a decrease in the observed Q-factor, but does not effect the resonance frequency. A wireless loss resistance R_w is the only component that fits this criteria. A inductance or capacitance

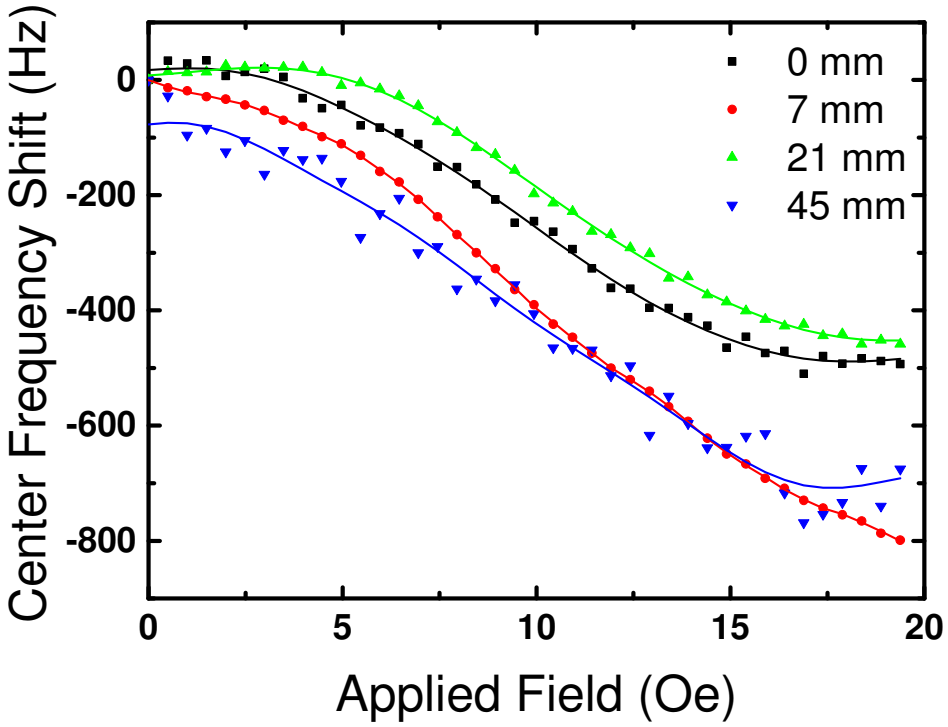

Figure 5.9. Center frequency shift versus applied magnetic field acquired at vertical separation distances from 0 to 45 mm. The magnetostrictive trend is observed at all distances. Beyond 45 mm the signal is no longer discernible from the noise with this setup.

would influence the resonance frequency, which is not observed in experiment. The modified BVD model with the R_w loss resistance is shown in figure 5.12(a), where C_o is the electrical capacitance, C_m, L_m and R_m are the motion capacitance, inductance and resistance used to describe the mechanical properties of the quartz.

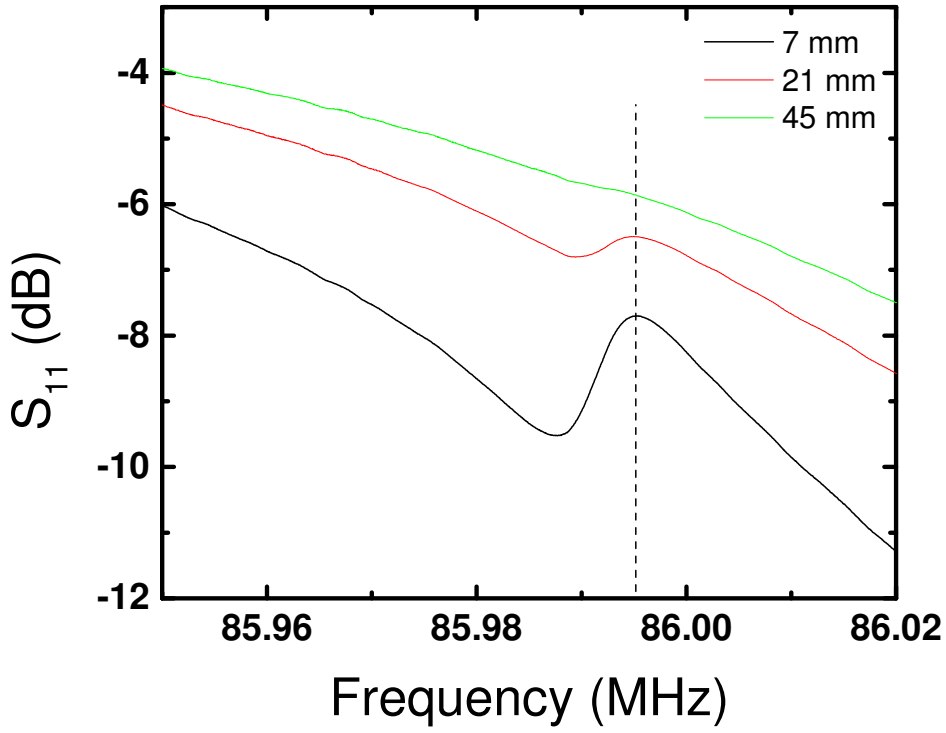

Figure 5.10. S_{11} magnitude response near the QCR resonance frequency at 7, 21 and 45 mm separation distances. The dashed line shows the location of the resonance frequency. As the separation distance increases the observed quality factor decreases but the resonance frequency is unaffected.

To extract the R_w value the device must first be measured and modeled in it's wired state and R_m must be determined. The traditional, wired BVD model is illustrated in figure 5.1. The real (conductance) and imaginary (suseptance) components of the impedance are shown in figure 5.11(a). R_m can be determined from this data as the inverse of the maximum conductance (G_{max}) as seen in (5.14). G_{max} can be seen in the impedance circle shown in figure 5.11(b) and R_m is determined to be 392 Ω. Next, L_m is be extracted from the Q factor using (5.16), where f_0 is the resonance frequency. The L_m is calculated to be 3.9 mH for a f_0 of 85.962689 MHz.

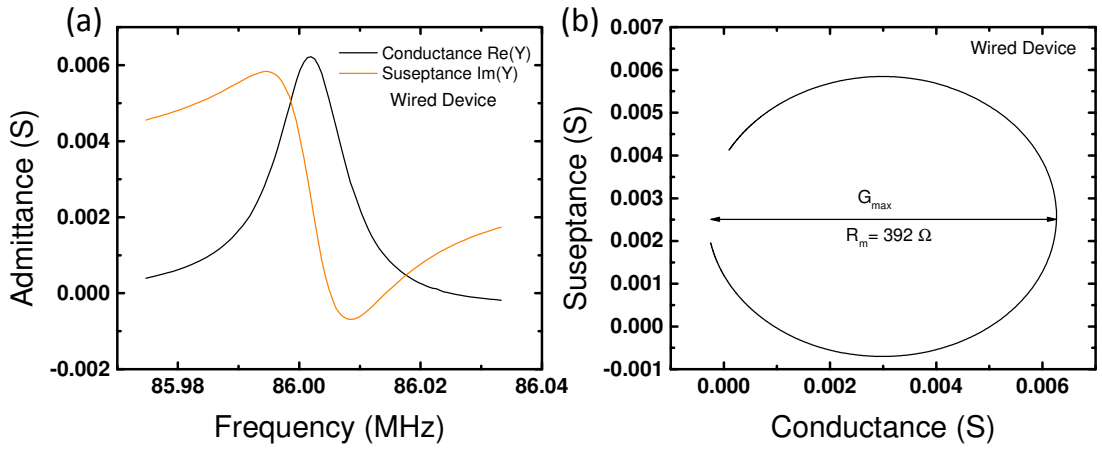

Figure 5.11. (a) The admittance vs. frequency measured with the device connected by an SMA cable. A Q-factor of 6617 is measured for the wired case. (b) The admittance circle clearly showing the G_{max} resulting in a R_m of 392 Ω.

$$R_m = \frac{1}{G_{\max}} \tag{5.14}$$

Finally, the wireless loss parameter R_w can be extracted from the S_{11} collected for the 0 mm to 45 mm separation distance. The S_{11} is modeled as two three-parameter Lorentzian functions shown in (5.15) to separate the loop resonance and the QCR resonance, I is the magnitude, f_a is the antenna resonance frequency, f_q is the quartz resonance frequency and γ_a and γ_q are the half width half max of the antenna and QCR respectively. Once the q-factor is determined from the QCR resonance Lorentzian, (5.16) is used to extract R_w for the different separation distances as plotted in figure 5.12(b). The Q-factor decreases linearly with distance and R_w increases linearly with distance.

$$S_{11[mag]} = 1 - I_a \left[\frac{{\gamma_a}^2}{(f - f_a)^2 + \gamma_a} \right] + I_q \left[\frac{{\gamma_q}^2}{(f - f_q)^2 + \gamma_q} \right] \tag{5.15}$$

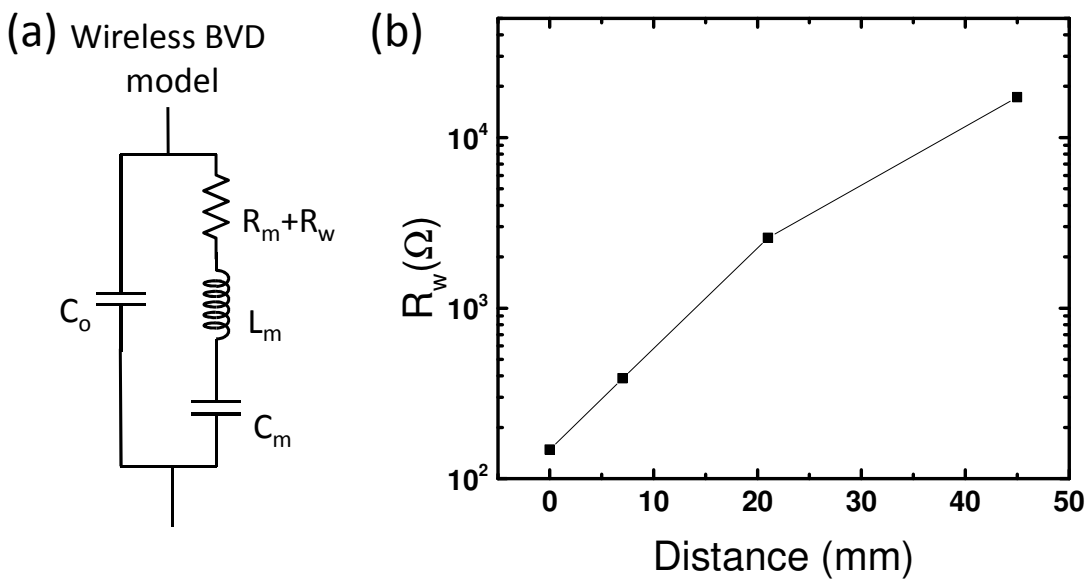

Figure 5.12. (a) Modified BVD model with an R_w component representing wireless losses. (b) Extracted R_w values versus distance showing an exponential increase as the separation distance increases.

$$Q = \frac{2\pi L_m f_0}{R_m + R_w} \tag{5.16}$$

5.5 Magnetic Sensitivity

The limit of detection for the wirelessly coupled magnetometer system is measured by recording the time based phase shift at the fundamental resonance resulting from excitation of the QCR with a low frequency AC magnetic field of incrementally decreasing amplitude. A 0.5 Hz AC magnetic field is applied to the QCR with amplitudes ranging from 7 μT to 130 μT at 0 mm separation distance. Figure 5.13(a) shows progressively smaller phase shifts as the AC field amplitude is decreased with signals down to 20 μT being visually observable. Using a fast fourier transform (FFT), a 7 μT signal is resolvable by using both wired and wireless connection (0 mm separation distance) to the sample as is shown in figure 5.13(b). The wireless connection has approximately 4× lower signal magnitude than the wired connection with comparable noise. The addition of the wireless energy loss does not shift the resonance frequency, however the full phase shift (θ) of 180° cannot be achieved due to the large R_w due to the phase being inversely

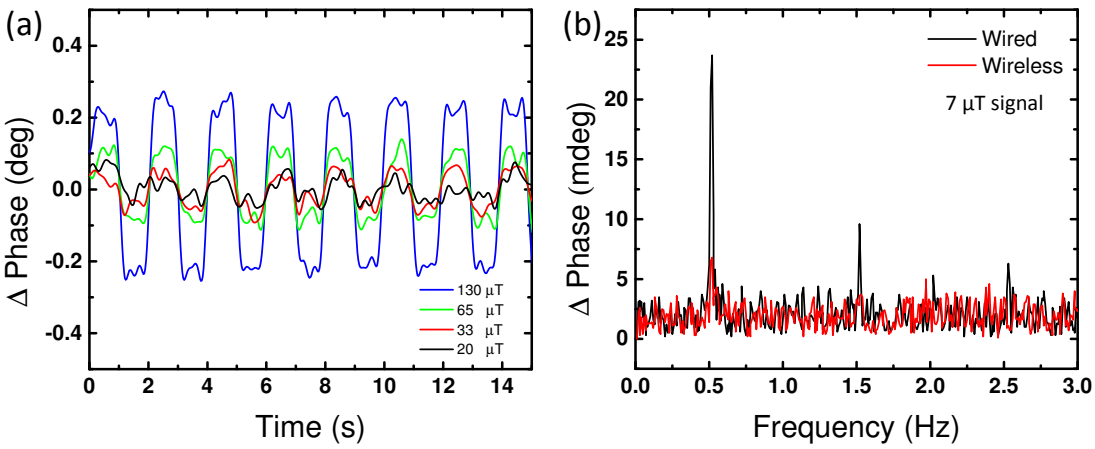

Figure 5.13. (a) The phase shift as a function of time during perturbation by 0.5 Hz square wave magnetic signals. (b) Phase shift as a function of frequency for the wired and wireless configurations collected with a 7 μT 0.5 Hz signal. The signal magnitude for the wireless case is approximately 4× lower than the wired connection with comparable noise.

proportional to the total the real resistor components as seen in (5.17), where X_L and X_C are the inductive and capacitive components of the reactance.

$$\arctan\theta = \frac{X_L - X_C}{R_m + R_w} \tag{5.17}$$

5.6 Conclusion

In conclusion, a resonant loop antenna and coupling loop are used to wirelessly interface with and resonate an 86 MHz magnetoflexoelastic quartz magnetometer. Experimental observations demonstrate clear magnetostrictive behavior at antenna separations of up to 45 mm. The limit of detection for the coupled wireless system is determined to be 7 μT at 0 mm separation distance and is comparable to the 1.5 μT limit of detection observed in the wired system. The frequency shift is similar in the wired and wireless case; however increasing separation distances reduces the phase shift sensitivity. The passively powered wireless quartz coupling system discussed in this chapter can be adapted to virtually any quartz sensor, since it simply requires changing the typical wired connector to an antenna. The fundamental frequency shifts of the quartz due to an external influence were not effected, but the extra loss factor due to the wireless coupling must be quantified, especially if phase shift is monitored. The wireless coupling can be improved with highly

directional horn antennas to increase the maximum separation distance and optimize the resolvable sensitivity of the sensor. For practical implementation of a biosensor only a few millimeters of separation distance is required to pass through tissue near the skin. With short separation distances, directional antennas and higher transmission power the limit of detection of these sensors may be very close to their wired counterparts making this a very promising development for many applications, including those requiring high sensitivity.

Chapter 6

Chip-Scale Whispering Gallery Mode Magnetometer

6.1 Introduction

There has been extensive research into low cost room temperature magnetometers with the goal of replacing superconducting quantum interface devices for biomagnetic sensing. Whispering gallery mode (WGM) optical resonators can tightly confine optical fields to a small mode volume and exhibit a very high quality factor, resulting in an extremely high sensitivity for a variety of sensing applications. WGM resonator sensors have shown exceptional promise for temperature [159], pressure [160], biomedical [161], and other applications.

Optical fiber-based interferometers have been studied for magnetic sensing applications [162, 163, 164]. The main concept of this kind of device is to immerse the interferometer into a magnetic fluid, and then quantify the spectral response while applying an external magnetic field. However, the full-width at half-maximum (FWHM) of resonances in most of the fiber-based interferometers is relatively large, thus hindering the resolution of the magnetic field sensing. Zu et al. demonstrated a sensitivity of 167 pm/mT with a resolution of 60 μT with a magneto-optical fiber [163]. Chen et al. used an optical fiber and magnetic fluid system to demonstrate a 905 pm/mT sensitivity, but did not report a limit of detection [162]. Luo et al. demonstrated an impressive 1918 pm/mT using a magnetic fluid and optical fiber, but did not report a limit of detection [164]. Recently, Amil et al., demonstrated a silicon micro-ring with a magnetic fluid

cladding with a sensitivity of 16.8 pm/mT; however the Q-factor of the device suffered significantly after application of the magnetic fluid [165]. Forstner et al. implemented a cavity optomechanical magnetometer using a toroidal whispering gallery mode resonator that is deformed by a magnetostrictive Terfenol-D epoxied to the micro-toroid and demonstrated a limit of detection down of 400 nT/$\sqrt{\text{Hz}}$ at mechanical resonance of approximately 9.5 MHz [166].

In this work, a new type of WGM magnetic sensor is proposed that is capable of retaining high Q-factors during the sensing process, and thus can perform as a high sensitivity magnetic sensor at low frequency. The basic configuration of the proposed design is a dome-like microbubble resonator with a rare-earth magnet attached on the top. When a magnetic field is applied, the attractive/repulsive force deforms and stresses borosilicate microbubble and results in a shift in the spectrum. It is worth mentioning that the Q-factor of the resonator does not show a significant change since the attachment of the magnet on the spherical shell does not induce any significant dissipation channels. Owing to the on-chip structure, the proposed device exhibits great potential for lab-on-chip applications using integrated photonic circuits.

6.2 Theory

The initial mathematical analysis of whispering gallery modes was done on acoustic waves by John William Strutt (Lord Rayleigh) when he studied sound waves propagating around the dome of St. Paul's Cathedral in London [167]. He discovered that the sounds waves were guided by reflections from the curved dome walls. The acoustic wave cross-section normally expands as it propagates in free space and the amplitude of decreases with the square of the distance from the source. However, in a whispering gallery the acoustic wave is not allowed to expand as much and the amplitude of the wave decreases only proportionally to the distance from the source.

6.2.1 Total Internal Reflection

The concept of reflecting waves can be applied to electromagnetic waves as well as acoustic waves like Lord Rayleigh did. To achieve resonance the electromagnetic wave in the dielectric medium must experience a total internal reflection. Total internal reflection originates from Snell's law seen in (6.1)

$$n_1 \sin\theta_i = n_2 \sin\theta_t \tag{6.1}$$

where n_1 and n_2 are the index of refraction of the material with the incident ray and the adjacent material, respectively. θ_i and θ_t are the incident and transmitted ray angles, respectively. It is clear from the equation that if $n_1 > n_2$ there are incident angles for which θ_t has no solution. The critical angle (θ_c)for when this occurs is defined as the $\theta_c = \theta_i$ expressed as (6.2), for which $\theta_t = 90°$ and therefor $\sin\theta_t = 1$

$$\theta_c = \arcsin\left(\frac{n_1}{n_2}\right) \tag{6.2}$$

6.2.2 Electromagnetic Analysis of WGM Resonators

The optical modes of a WGM resonance must match to constructively interfere so the resonance condition is (6.3)

$$\frac{\lambda_0}{n} m = 2\pi R_0 \tag{6.3}$$

where λ_0 is the 0th order resonant wavelength, *n* is the index of refraction, R_0 is the radius of the microbubble and *m* is the mode index, an integer.

For the 0th and 1st order modes are (6.4) and (6.5) respectively:

$$\lambda_0 = \frac{2\pi R_0 n}{m} \tag{6.4}$$

$$\lambda_1 = \frac{2\pi R_0 n}{m+1} \tag{6.5}$$

The successive orders can be rewritten as (6.6) and the spacing between the modes, also known as the free spectral range (FSR) can be written as (6.7). If R_0 » λ_0 then the FSR is relatively small compared to the radius so $\lambda_0 \approx \lambda_1$.

$$\frac{\lambda_0 - \lambda_1}{\lambda_0 \lambda_1} = \frac{1}{2\pi R_0 n} \tag{6.6}$$

$$FSR = \lambda_0 - \lambda_1 = \frac{\lambda_0 \lambda_1}{2\pi R_0 n} \approx \frac{{\lambda_0}^2}{2\pi R_0 n} \tag{6.7}$$

The Helmholtz equation is the fundamental basis of the methods used to describe

spherical electromagnetic wave behavior inside and outside a dielectric medium. A comprehensive derivation is given by Oraevsky [168]. The compact version of the equation is (6.8)

$$\left(\nabla^2 + k^2 n^2\right) \Psi = 0 \tag{6.8}$$

where $k = \frac{2\pi}{\lambda}$, the angular frequency and Ψ is the amplitude of the wave. Transforming to spherical coordinates and assuming the E-type waves (TE modes) have H_r=0 and H-type waves have E_r=0. The Helmholtz equation can be formulated (6.8).

$$\frac{1}{r^2}\frac{\partial}{\partial r}\left(r^2\frac{\partial \psi}{\partial r}\right) + \frac{1}{r^2\sin(\theta)}\frac{\partial}{\partial \theta}\left(\sin(\theta)\frac{\partial \psi}{\partial \theta}\right) + \frac{1}{r^2\sin^2(\theta)}\frac{\partial^2 \psi}{\partial \phi^2} - n_s^2 k_0^2 \psi = 0 \tag{6.9}$$

By applying the separation of variables method *R*, θ, and ϕ three sets of equations can be produced (6.10),(6.11),(6.12).

$$\frac{d^2\psi_r}{\partial r^2} + \frac{2}{r}\frac{d\psi_r}{\partial r}\left[r^2 n_s k_0^2 - \frac{l\,(l+1)}{r^2}\right]\psi_r = 0 \tag{6.10}$$

$$\frac{1}{\cos(\theta)}\frac{d}{d\theta}\left(\cos(\theta)\frac{d}{d\theta}\psi_\theta\right) - \frac{m^2}{\cos\left(\theta\right)^2}\psi_\theta + l\,(l+1)\,\psi_\theta = 0 \tag{6.11}$$

$$\psi_\phi = \frac{1}{\sqrt{2\pi}} e^{\pm im\varphi} \tag{6.12}$$

The solution for ψ_θ is $\psi_\theta = P_l^m(cos(\theta))$, where P_l^m are the Associated Legendre Polynomial.

Of particular interest is (6.10), which is the spherical Bessel function and can be used to determine the field inside and outside of the microbubble. The general solution is given by

$$\psi_r = c_1 j_l(kr) + c_2 y_l(kr) \tag{6.13}$$

where j_l and y_l are the first and second kind of spherical Bessel functions, respectively, of the order l and defined by the ordinary Bessel functions J_l and Y_l by (6.14) and (6.15):

$$j_l(x) = \sqrt{\frac{\pi}{2x}} J_{l+1/2}(x) \tag{6.14}$$

$$y_l(x) = \frac{\pi}{2x} Y_{l+1/2}(x) = (-1)^{l+1} \sqrt{\frac{\pi}{2x}} J_{-l-1/2}(x) \tag{6.15}$$

When the radial solution given by equation (6.13) is evaluated for $r \to 0$ the spherical Bessel functions for x«1 are $j_l(x) \to \frac{x^l}{(2l-1)!!}$ and $y_l(x) \to \frac{(2l-1)!!}{x^{l+1}}$ and it is clear that y_l(r) becomes divergent as $r \to 0$ so the field distribution inside the sphere is 6.16

$$\psi_r = c j_l(n_s k_0 r) \text{ for } r < R_0 \tag{6.16}$$

To evaluate the electric field outside of the microsphere the local coordinate system must be adjusted so that the coordinate transform $r = R_0(1 + x/R_0)$ and r_{-1} is expanded as $R_0^{-1}(1 - x/R_0)$

$$\frac{d^2\psi_r}{dr^2} + \frac{2}{r}\frac{d\psi_r}{dr} + \left[n_s^2 k_0^2 - \frac{l(l+1)}{R_0^2} + \frac{2x(l(l+1)+2}{R_0^3} \right] \psi_r = 0 \tag{6.17}$$

This is the familiar Airy equation. We can assume that the evanescent wave only extends a few wavelengths out of the microsphere and that the radius of the sphere is much larger than the wavelength (x/R_0 « 1), the Airy equation reduces to (6.18)

$$\frac{d^2\psi_r}{dr^2} + \frac{2}{r}\frac{d\psi_r}{dr} + \left[n_s^2 k_0^2 - \frac{l(l+1)}{R_0^2} \right] \psi_r = 0 \tag{6.18}$$

The solution to (6.18) is $\psi_r \sim e^{-\alpha_l x}$, where $\alpha_l = \sqrt{\beta_l^2 - k_0^2 n_0^2}$ and $\beta_l = \sqrt{l(l+1)}/R_0$

$$\psi_r = N_r \begin{cases} j_l(k_0 n_s r) & (r < R_0) \\ B h_l(k_0 n_0 r) & (r > R_0) \end{cases} \tag{6.19}$$

where N_r is the normalization constant (6.20),

$$N_r = \frac{2}{R_0^3} \left(\left(1 + \frac{1}{\alpha_s R_0} \right) j_l^2(k_0 n_s R_0) - j_{l-1}(k_0 n_s R_0) j_{l+1}(k_0 n_s R_0) \right)^{-1} \tag{6.20}$$

B is a constant determined from boundary conditions. The electric field at the boundary should be continutues so the equations can be equated at $r = R_0$ leading to $j_l(k_0 n_s r) = B h_l(k_0 n_0 r)$, so (6.19) can be rewritten as (6.21)

$$\psi_r = N_r \begin{cases} j_l(k_0 n_s r) & (r < R_0) \\ \frac{j_l(k_0 n_s r)}{h_l(k_0 n_0 r)} h_l(k_0 n_0 r) & (r > R_0) \end{cases} \tag{6.21}$$

6.2.3 Force Applied by the Permanent Magnet

The force applied by a magnetic field on a permanent magnet can been analytically evaluated. For the case of a permanent magnet axial to an electromagnetic coil Shiri and Shoulaie's filament method is adapted [169]. They proposed a filament method to break up the problem into circular conducting filaments was originally design for 2 conducting electromagnetic single turn coils, but can be adapted to 1 electromagnet and 1 cylindrical permanent magnet, magnetized axially [170]. First the case for axial force felt by a free coil in the 2-coil system is considered, then the adaptation for 1 coil and 1 permanent magnet will be explained.

The force felt on a free electromagnetic coil in response to another electromagnetic coil is given by (6.22)

$$F(r_1, r_2, z) = \mu_0 I_1 I_2 z \sqrt{\frac{m}{4r_1 r_2}} \left[K(m) - \frac{m/2 - 1}{m - 1} E(m) \right] \tag{6.22}$$

where μ_0 is the permeability of free space, I_1 and I_2 are the currents in the fixed and floating coils respectively, r_1 and r_2 are the radius of the fixed and floating coils respectively, m is given by (6.23). E(k) and K(k) are the first and second order elliptical integrals give by (6.24) and (6.25) respectively. $k = m^2$

$$m = \frac{4r_1 r_2}{(r_1 + r_2)^2 + z^2} \tag{6.23}$$

$$K(k) = \int_0^{\pi/2} \frac{d\theta}{(1 - k^2 \sin^2\theta)^{1/2}} \tag{6.24}$$

$$E(k) = \int_0^{\pi/2} \left(1 - k^2 \sin^2\theta\right)^{1/2} d\theta \tag{6.25}$$

Using the filament method, the force from any arrangement of coaxial coils can be calculated by summing the force from each turn of a multi-turn coil system as a superposition of forces using the result of every pair of equations (6.22) and (6.23). To adapt the equation for the case of 1 electromagnetic coil and 1 permanent magnet, the permanent magnet is written as an equivalent electromagnetic coil where the current of the "floating coil" is determined by $I_2 = B_r l_m / (N_m \mu_0)$ where B_r is the permanent magnet strength, l_m is the number of psuedo turns assigned to the permanent magnet.

This value should be sufficiently large so that the force converges to a stable value. (6.26) is the equation of the force using the filament method, were $r(n_r)$ is (6.27) and $L\left(n_m, n_z\right)$ is (6.28),

$$F_{z_1} = \sum_{n_m=1}^{N_m} \sum_{n_r=1}^{N_r} \sum_{n_z=1}^{N_z} F_f\left(r\left(n_r\right)\right), R_m, z + L\left(n_m, n_z\right) \tag{6.26}$$

$$r(n_r) = R_c + \frac{n_r - 1}{N_r - 1}\left[R_c - r_c\right] \tag{6.27}$$

$$L\left(n_m, n_z\right) = -\frac{1}{2}\left[l_m + l_c\right] + \frac{n_z - 1}{N_z - 1} l_c + \frac{n_m - 1}{N_m - 1} l_m \tag{6.28}$$

where R_m is the magnet radius, r_c and R_c are the inner and outer coil radii, l_m and l_c are the magnet and coil lengths respectively. N_r and N_z are the number of tuns in the coil in the radial (thickness) and axial direction (length), N_m is the number of turns in the psuedo coil representing the permanent magnet. z is the axial distance between the coil and permanent magnet.

For the case of orthogonally magnetized permanent magnets Janssen et al. have proposed an analytical model to calculate the interaction forces [171]. The definition of the dimensions, coordinate system of the problem is defined in figure 6.1.

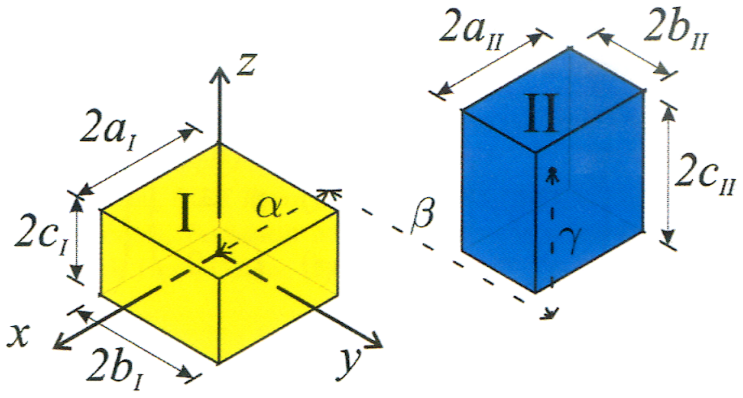

Figure 6.1. Dimensions and coordinate system of the orthogonal oriented magnets considered in the analytical derivation. Magnet *I* is magnetized along the +Z axis and magnet *II* is magnetized along the +Y axis. Adapted from [171].

The force is given by (6.29) where the magnetic field strength of the orthogonal magnets are B_{r_I} and $B_{r_{II}}$ for the floating and fixed magnet respectively. Similar to

the axial force case, a coil can be written as an equivalent permanent magnet where $B_{r_{II}} = \frac{I_c N_r \mu_0}{l_c}$. The floating cuboid magnet dimensions are defined to approximated the volume of the cylindrical magnet used in this experimental. Referring back to the axes defined in figure 6.1, the diameter of the cylindrical magnet defines the sides in the x and y axes of cuboid I and the side with the magnetized axes (z) is defined by the length of the cylindrical magnet. Similarly, the sides of fixed cuboid magnet (cuboid II) are defined to approximate the electromagnetic coil used in this experiment. Where 2 axes of the fixed cuboid (y and z) are defined by the diameter of the electromagnetic coil and the length of the coil defines the the side in the y axes. Robertson et al. shared their matlab code for this methodology and it was adapted for this work [170].

$$F_I = \frac{B_{r_I} B_{r_{II}}}{4\pi\mu_0} \sum_{i=0}^{1}\sum_{j=0}^{1}\sum_{k=0}^{1}\sum_{l=0}^{1}\sum_{p=0}^{1}\sum_{q=0}^{1} (-1)^{i+j+k+l+p+q} \psi_I \tag{6.29}$$

The force in *x, y and z* are (6.30), (6.31), and (6.32) respectively. *S, T, U and R* are (6.33) and are composed of the dimensions defined in figure 6.1.

$$\begin{aligned}\psi_{x_1} = \frac{1}{2}\Bigg\{ &\left(\tan^{-1}\left(\frac{U}{S}\right) + \tan^{-1}\left(\frac{TU}{SR}\right)\right) S^2 \\ &+2TS - 3US - 2ST\log\left(U+R\right) - 2T^2\tan^{-1}\left(\frac{S}{T}\right) \\ &+U\Bigg[U\left(2\tan^{-1}\left(\frac{S}{U}\right) + \tan^{-1}\left(\frac{U}{S}\right) + \tan^{-1}\left(\frac{ST}{UR}\right)\right) \\ &-2T\log\left(S+R\right) + 2S\log\left(R-T\right)\Bigg] + T^2\tan^{-1}\left(\frac{SU}{TR}\right)\Bigg\}\end{aligned} \tag{6.30}$$

$$\begin{aligned}\psi_{y_1} = \frac{1}{2}\Big[&U\left(R-2S\right) + \left(T^2 - S^2\right)\log\left(U+R\right) \\ &+2S\left(T\left(\tan^{-1}\left(\frac{U}{T}\right) + \tan^{-1}\left(\frac{SU}{TR}\right)\right) + U\log\left(R-S\right)\right)\Big]\end{aligned} \tag{6.31}$$

$$\begin{aligned}\psi_{z_1} = \frac{1}{2}\Big[&T\left(R-2S\right) + \left(U^2 - S^2\right)\log\left(T+R\right) \\ &+2S\left(U\left(\tan^{-1}\left(\frac{T}{U}\right) + \tan^{-1}\left(\frac{ST}{UR}\right)\right) + T\log\left(R-S\right)\right)\Big]\end{aligned} \tag{6.32}$$

$$
\begin{aligned}
S &= \alpha - (-1)^i a_1 + (-1)^j a_{II} \\
T &= \beta - (-1)^k b_1 + (-1)^l b_{II} \\
U &= \gamma - (-1)^p c_1 + (-1)^q c_{II} \\
R &= \sqrt{S^2 + T^2 + U^2}
\end{aligned}
\tag{6.33}
$$

6.3 Experimental Setup

6.3.1 Chip-scale Whispering Gallery Mode Fabrication

Microbubbles are fabricated using a chip-scale glassblowing process inspired by a method pioneered by Eklund et al. [172]. First, 380 μm diameter circles are patterned using positive photoresist on silicon. A deep reactive ion etch process is used to etch 250 μm of silicon. The photoresist is stripped away with RemoverPG at 70 °C for 15 minutes, followed by a piranha etch (H_2SO_4:(30%)H_2O_2 3:1) to remove any remaining photoresist. Next, the etched silicon is anodically bonded to a 100 μm thick Pyrex 7740 wafer at 133 kPa (∼1000 Torr), trapping air inside the cavity. The wafer is diced and a 49% HF etch is done to thin the borosilicate glass to (75, 50 and 37.5) μm thickness to achieve a range of microbubble shell thicknesses after glassblowing. The etched die is placed in a 13.3 kPa (∼100 Torr) vacuum and heated on a silicon nitride ceramic heater to 775 °C for 30 seconds and rapidly cooled to approximately 550 °C, followed by a gradual reduction in power to prevent thermally shocking the thin glass microbubbles. During this process, the borosilicate softens and begins to expand into a spherical shell due to the pressure differential between the sealed cavity and the outside pressure. Finally, Devcon 5 minute epoxy is used to carefully attach a N48 grade 1.5 mm diameter and 1.5 mm long neodymium magnet to the top of the microbubble. It is critical to keep the epoxy from contaminating the equator of the microbubble, which is crucial for the optical resonance.

The finished devices with the magnet oriented parallel or orthogonal to the sample surface are shown in figure 6.2(a) and (b), respectively. To determine the shell thickness the microbubbles are broken after the experiment and the thickness is measured by scanning electron microscopy near the equator. It should be noted that the shell thickness varies along the height of the microbubble [172].

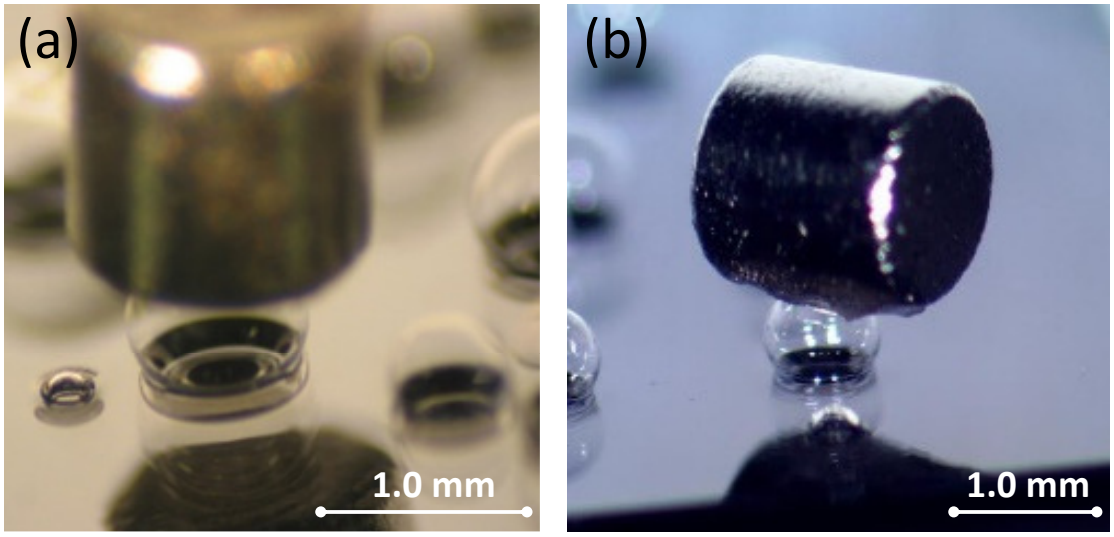

Figure 6.2. Completed devices with the magnet oriented (a) orthogonal and (b) parallel to the sample surface.

6.3.2 Magnetic Testing

The experimental setup used to apply the magnetic field and probe the optical resonance is illustrated in figure 6.3. A 25 mm diameter, 17 mm long, 23 turn coil is wound and the device is placed 8 mm from the edge of the coil. A 760 nm tunable laser (Thorlabs, TLK-L780m) evanescently couples to the microbubble through a tapered fiber. A fiber polarization controller (3 waveplates) is used to control the polarization to optimize the coupling efficiency. The transmission is measured using a photodiode (Thorlabs, DET36A). The magnetic field produced by the coil is calibrated using a commercial magnetometer (Lakeshore 475, HMMA-2504-VR). To test the magnetic sensitivity, the magnetic field is swept from 0 μT to +630 μT and then back to 0 μT, then to -630 μT and again back to 0 μT. The sample is secured to a stage to minimize motion perturbation and potentially de-coupling from the fiber. To test the limit of detection and noise characteristics of the setup, the laser is held to the steepest portion of a WGM resonance peak and a Stanford Research SR760 is used to analyze while a signal of a known frequency is applied. Figure 6.4 shows a camera image of the test setup. The pulled fiber and sample are separated to take the picture, during testing the fiber touches the equator of the sample to evanescently couple the light.

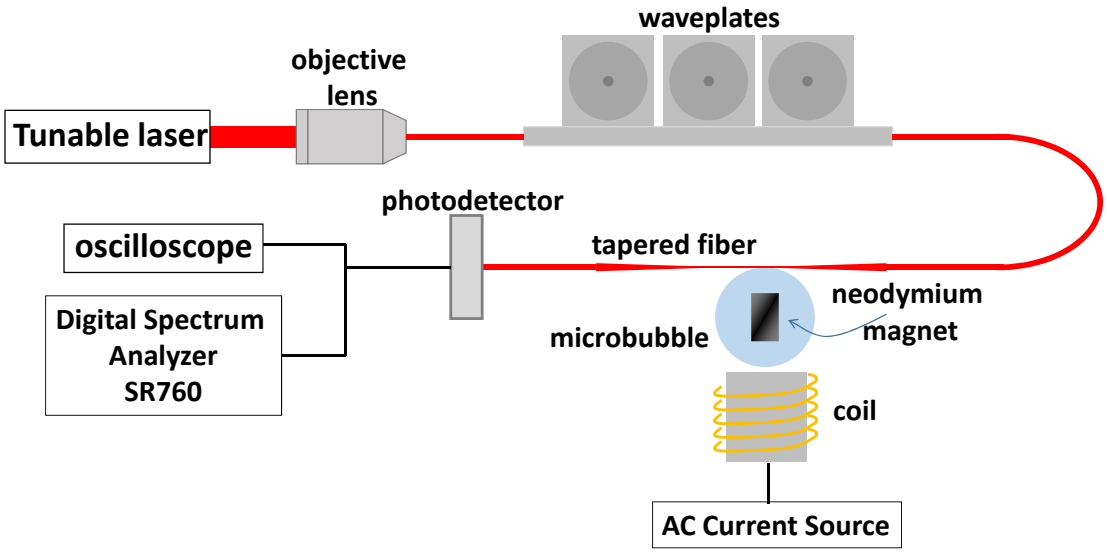

Figure 6.3. Illustration of the test setup which tracks the resonance frequency shift due to an applied magnetic field from an electromagnetic coil. For limit of detection testing, a Stanford Research SR760 is used to analyze the noise characteristics of the device.

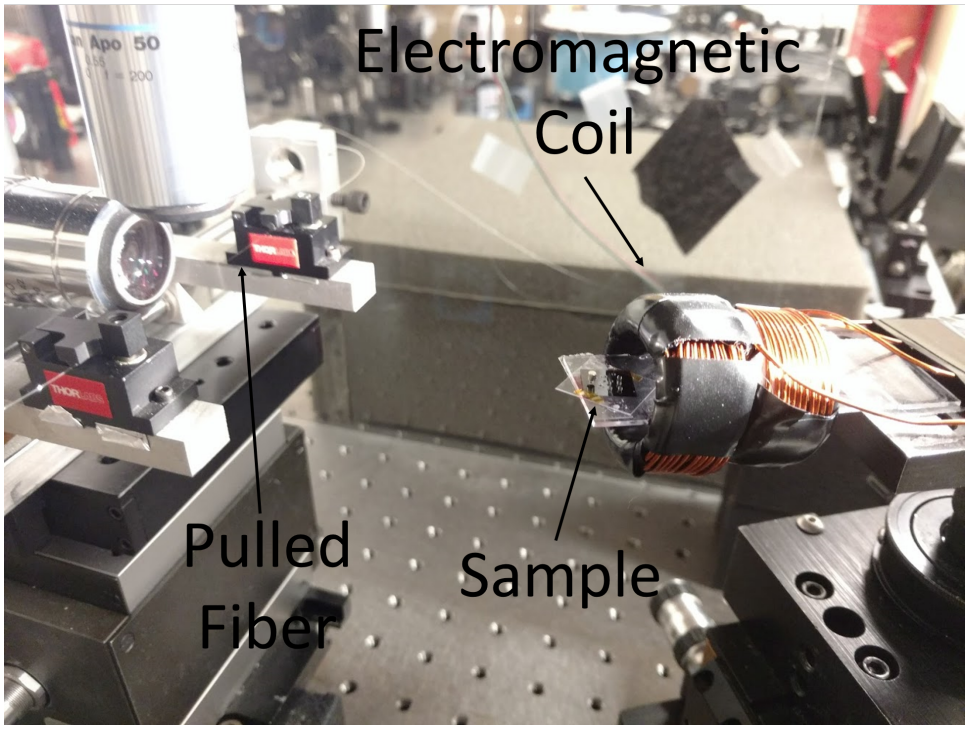

Figure 6.4. Camera image of the magnetic test setup. To take the photo the sample and fiber are separated, during test they are touching. The coil closest to the sample is energized, the coil further away is not used for this experiment.

6.4 Results and Discussion

6.4.1 Optical Resonance

Since the integration of the permanent magnet at the top of the microbubble does not introduce significant scattering losses near the equator of the device where the optical field is confined, a high Q-factor can be maintained. The typical transmission vs. detuning sweep for a microbubble and an attached neodymium magnet with a 1.1 μm shell thickness is shown in figure 6.5(a). Owing to the atomically smooth surface from the glassblowing process [173], very high optical resonant Q-factors in the range of 0.9×10^6 to 1.1×10^7 are realized for the devices used in this work. Figure 6.5(b) shows the sensor method of action where an applied magnetic field shifts the resonance frequency. It should also be noted that there was no significant change in the Q-factors of the devices for the range of magnetic fields applied in this work.

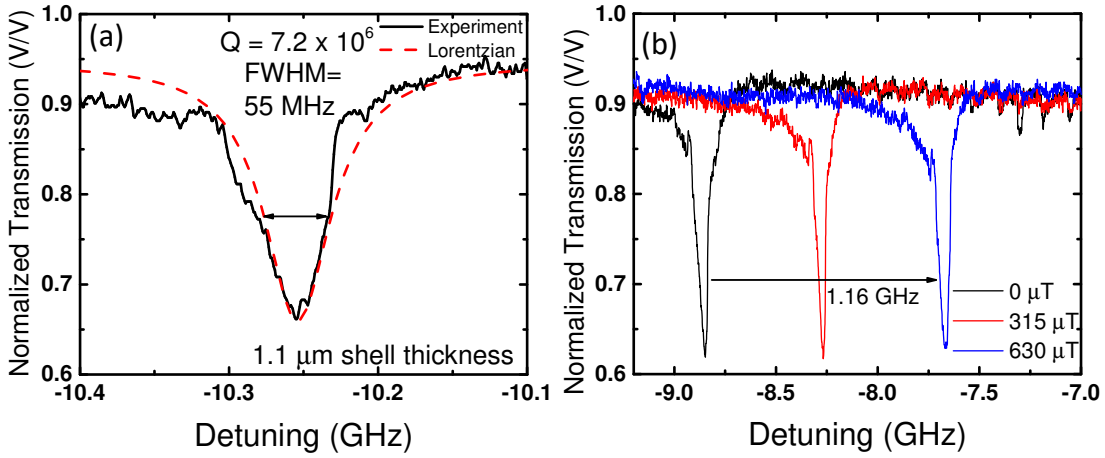

Figure 6.5. 7.2 x 10^6 Q-factor resonance for a 1.1 μm shell thickness microbubble with an attached neodymium magnet. The inset shows other resonant peaks and their Q-factors for this microbubble. (b) Resonance frequency shift due to an applied magnetic field, showing no significant change in Q-factor for at least 630 μT

6.4.2 Magnetic Sensing

Figure 6.6(a) shows the magnetometer sensitivity measured for 3 devices with 2.4 μm, 1.5 μm and 1.1 μm shell thickness with a neodymium magnet epoxied orthogonal to the microbubble sample plane. As expected, the sensitivity is inversely proportional to the shell thickness. The device shows little hysteresis and the frequency shift switches from a red-shift (negative Δf) to a blue-shift (positive Δf) when the magnetic field direction goes from negative to positive. This confirms that the phenomenon is due to the magnetic forces and not heat from the coil, which would have caused only a red shift. The best sensitivity was measured to be 1.9 GHz/mT from the 1.1 μm shell thickness device

Figure 6.6(b) shows the magnetometer response measured for devices with 1.8 μm, and 1.2 μm shell thickness with a neodymium magnet epoxied parallel to the sample plane and coaxial to the coil central axis. The sensitivity is measured to be 0.2 GHz/mT and 0.1 GHz/mT for the 1.8 μm and 1.2 μm shell thickness devices, which were much lower than the orthogonal case and does not increase inversely to shell thickness. This suggests the devices are operating through the non-ideal alignment of the magnet and coil, which is imparting some orthogonal forces. The observed hysteresis is within the natural drift in the laser.

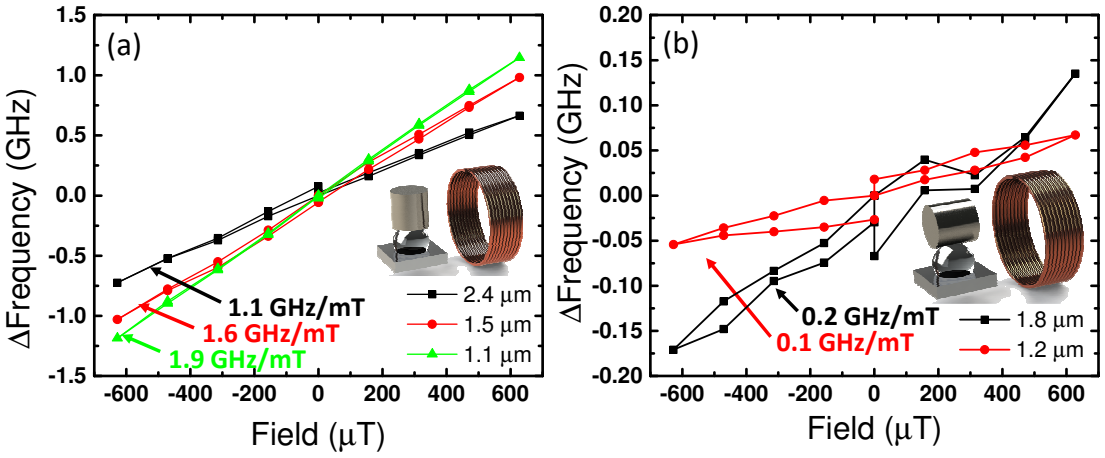

Figure 6.6. (a) Up to 1.9 GHz/mT sensitivity and a trend inversely proportional to shell thickness is observed for devices with the magnet oriented normal to the device place and orthogonal to the coil. (b) Lower sensitivity of up to 0.2 GHz/mT is observed for devices with the magnet oriented parallel to the device plane and axial to the coil. Illustrations are not to scale.

6.4.3 Modeling

The filament method is used to determine that an axial force (x-axis) of 310 μN/mT is applied to the magnet axially aligned to the coil (parallel to sample plane). The matlab code for this solution is found in appendix C. The solution for a magnet orthogonal to the coil calculates a 226 μN/mT in the z-axis (orthogonal to the sample plane). Using these forces as an input to a COMSOL model, the deformation for an axial force on the bubbles is seen in figure 6.7(a). For this axial case, where the sphere deforms in unison, it results in minimal radius change. The Δr per mT is extracted from the COMSOL model by finding the difference in circumference between the deformed microbubbles and an unperturbed device. Δr is determined to be very low for the axial case, just 1.8 fm and 1.2 fm, resulting in a very small shifts of 3.8 kHz/mT and 2.5 kHz/mT. The COMSOL model effectively predicts no sensitivity in this case. The small effect seen experimentally may be from non-ideal alignment between the coil and axial permanent magnet imparting a z-force. For the orthogonal case seen in figure 6.7(b), the deformation causes a bulging out of the equator, which is extracted from the COMSOL model. The Δr is determined to be 180 pm, 230 pm and 270 pm, for the (2.4, 1.5 and 1.1) μm shell thickness respectively, which is much higher than the axial case. Table 1 shows a summary of the theoretical and experimental sensitivity, which explains the poor performance of the axially aligned

magnet samples. The discrepancy between model and theory may be because the non-uniform shell thickness, which is thinner near the top of the microbubble is causing more strain to transfer to the equation than COMSOL predicts. Another possible cause of the discrepancy is that the contribution of the photoelastic effect may need to be included in the analysis. For more accurate modeling both the non-uniform shell thickness and the photoelastic effect need to be considered.

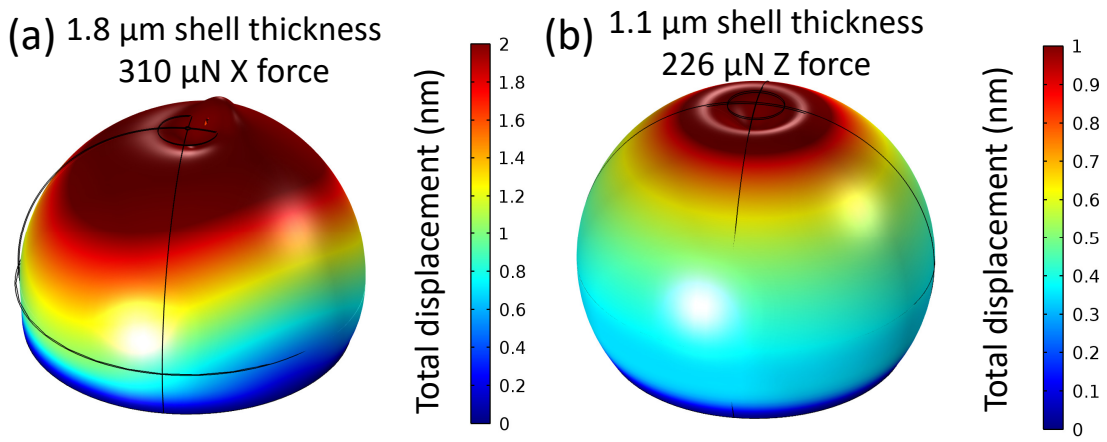

Figure 6.7. Typical deformation observed for (a) axial magnet orientation (b) orthogonal magnet orientation.

6.4.4 Limit of Detection

To test for the limit of detection a device with the highest measured Q-factor was chosen. The microbubble was fabricated from borosilicate glass etched down to 37.5 µm thick and is measured to have an approximately 1.8 µm thick glass shell at the equator. The frequency shift for this device is shown in figure 6.8(a) and the sensitivity is determined to be 1.43 GHz/mT.

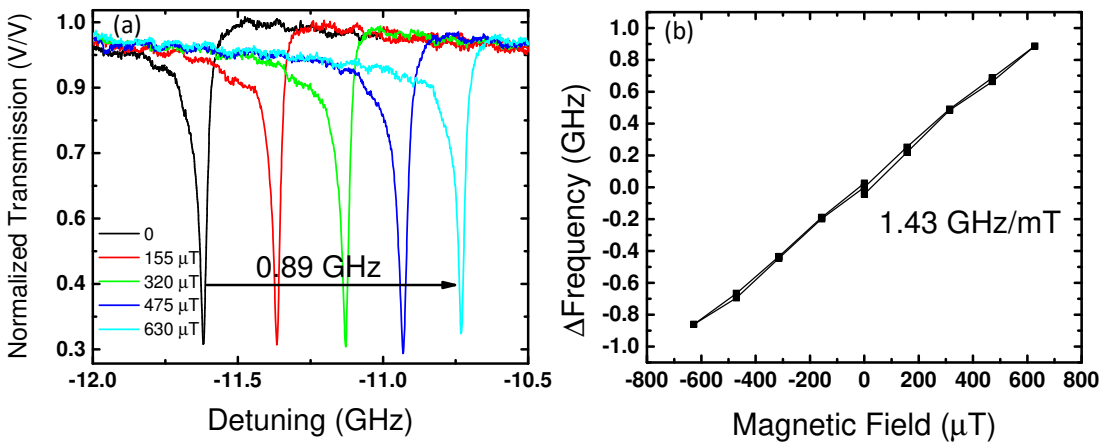

Figure 6.8. (a) Sensitivity of the WGM is evaluated by tracking the frequency shift. (b) Frequency shift is linear with a sensitivity of 1.43 GHz/mT and shows little hysteresis.

The device has an exceptional Q-factor of 1.1×10^7 as seen in figure 6.9(a) with a full width half max of 35 MHz. The laser is detuned by approximately -11.6 GHz to operate the device at the sharpest point of the WGM resonance. While applying a known 1.6 μT signal the response is monitored on the digital spectrum analyzer and a limit of detection of 60 nT/$\sqrt{\text{Hz}}$ is measured at 100 Hz as seen in figure 6.9(b). The dominant noise is evaluated by measuring the noise of the laser without any coupling to the WGM. The green line in figure 6.9(b) shows that the laser itself is the dominant source of noise, not the WGM magnetometer. Next, the photodetector noise is valuated at maximum gain, typical gain, and minimum gain. As expected there is more dark current in the photodetector as the gain increases, producing more noise. Operating at minimum gain on the photodiode and assuming a perfectly stable laser and environmental noise compensation on the WGM the LOD of this setup can be as low as 100 pT/$\sqrt{\text{Hz}}$. A photodetector operating off a DC battery may offer even lower noise, pushing the noise floor lower.

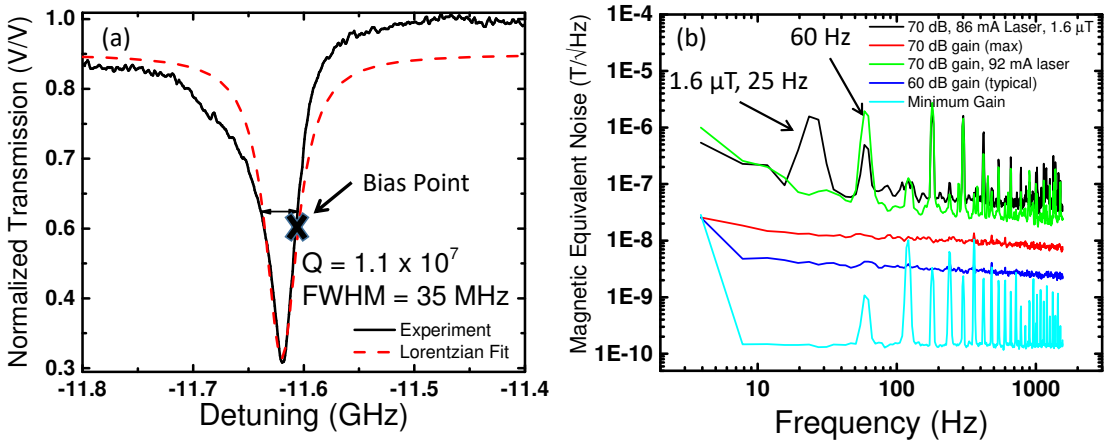

Figure 6.9. (a) Normalized transmission of a 1.1 $\times$ 10^7 Q-factor WGM mode, with the bias point highlighted. (b) Magnetic equivalent noise from the WGM magnetometer (black line), laser (green line), photodiode at max gain (red line), typical gain (dark blue line) and minimal gain (light blue line). LOD of the device is 60 nT/$\sqrt{\text{Hz}}$, which is limited by laser noise. In an ideal situation the ultimate limit of this setup is set by the photodetector noise at 100 pT/$\sqrt{\text{Hz}}$

The theoretical limit of detection can be determined using (6.34). Substituting for the best sensitivity $\left(\frac{\Delta f}{\Delta B}\right)$, 1.9 GHz/mT, the slope of the high-Q WGM resonance $\left(\frac{\Delta V}{\Delta f}\right)$, 213 V/GHz, and the resolution a high quality photo detector R_{pd} is 40 µV [174], resulting in a theoretical limit of detection of 98 pT.

$$LOD = \left[\frac{\Delta f}{\Delta B}\frac{\Delta V}{\Delta f}(R_{pd})^{-1}\right]^{-1} \tag{6.34}$$

6.5 Conclusion

In conclusion, a novel chip-scale high-Q WGM magnetometer has been demonstrated and modeled. Modeling and experimental results show that the device is most sensitive when the magnet is applying force orthogonal to the plane of the sample. By utilizing this configuration, a WGM resonator with Q-factor up to 1.1 $\times$ 10^7 has been demonstrated and a maximum magnetometer magnetic sensitivity of 1.9 GHz/mT (5.7 pm/mT) was experimentally demonstrated. An experimental limit of detection of 60 nT/$\sqrt{\text{Hz}}$, which is limited by laser noise, and a theoretical limit of detection of 98 pT. Owing to the on-chip physical structure, the proposed device exhibits great potential for future lab-on-chip applications of with integrated photonic circuits.

Chapter 7

Conclusions and Future Work

Magnetic sensing is a quickly evolving field with novel technologies being developed and current technologies being improved. Biomagnetic sensing being a major motivator for many of these advances. Three major contributions to the field of magnetic sensing were presented in this dissertation: A comprehensive optimization strategy for magnetoelectric magnetometers, including annealing and magnetic domain alignment to optimize the magnetostriction coefficient. A novel passively powered wireless interface to a quartz magnetoflexoelastic magnetometer was demonstrated, the limit of detection was evaluated and compared to a wired version, and the effect of separation distance modeled using a modified Butterworth-van Dyke model. A novel high-Q whispering gallery mode magnetometer based off a chip-scale glassblowing process was demonstrated, modeled using COMSOL and the limit of detection was evaluated.

7.1 Magnetoelectric Optimization

The sub-100 pT limit of detection achieved in magnetoelectric magnetometers offers a tantalizing possibility of realizing magnetocardiography using relatively cheap, room temperature magnetometers. Just recently, Reermann et al. used complex averaging techniques to make cardiological measurements using a magnetoelectric sensor [175]. Persistent optimization of magnetoelectric sensors will be critical to push the technology "over the finish line" so to speak and into practical biomagnetic applications.

An optimized annealing process for Metglas 2605SA1 of 400 °C for 30 minutes under a 160 mT transverse magnetic field in an N_2 ambient resulted in an exceptionally high

magnetostriction coefficient of 79.3 $\frac{\mu m}{m \cdot mT}$ and a saturation magnetostriction of 50.6 μm/m. Using SEMPA the magnetic domains were imaged and their alignment was quantified to confirm magnetic alignment in response to the applied magnetic field. The effect of flux concentration is evaluated for length, width and thickness of the Metglas ribbon. The epoxy used to couple the strain between the piezoelectric and magnetostrictive phases is optimized in terms of thickness, stiffness and porosity. Finally, implementing a PMN-PT macro fiber composite along with the other optimizations resulted a magnetoelectric coefficient of 18.6 $MV/(m \cdot T)$ and 6.5 V/mT with a limit of detection of 50 pT at 20 Hz.

For future work the annealed and aligned Metglas 2605SA1 ribbons should be made longer to take advantage of the flux concentration effect. Thinner PMN-PT should be use to maximize strain in the piezoelectric. Finally, more biomagnetic experiments need to be performed to move this technology into practical medical applications.

7.2 Passively Powered Quartz Magnetoflexoelastic Magnetometer

The passively powered wireless quartz magnetoflexoelastic magnetometer has potential applications in biomagnetic interfaces, magnetocardiography, magnetoencephalography, and traffic sensing. Furthermore, the wireless interface developed in this dissertation can be used on quartz or other resonant piezoelectrics that have been functionalized for (bio)chemical and physical force sensing. Currently, quartz magnetoflexoelastic magnetometers have been demonstrated with a limit of detection of 79 nT at 10 Hz [52]. Hatipoglu et al. predicted that 28 pT limit of detection would be possible for very thin, 180 nm thick, quartz resonators [52]. Implanting the magnetometer would allow it to be extremely close to the biomagnetic source and the sensitivity requirements would not be so stringent.

In this work, a passively powered wireless quartz magnetoflexoelastic magnetometer based on near-field coupling was experimentally demonstrated. The wireless interface is compared to a wired interface version of sensor. The resonant characteristics and wireless energy transfer are modeled using a modified Butterworth-van Dyke model to understand the effect of separation distance. The wireless probing of the quartz was demonstrated up to 45 mm using only 1 mW of power. A limit of detection of 7 μT was demonstrated at 0 mm separation distance.

The wireless interface developed in this work does not fundamentally depend on the sensor being a magnetometer. As a result this can be used to realize passively powered wireless sensing using any of the multitudes of functionalizations developed for quartz sensors. Also, the phenomenon is not limited to quartz, but can be utilized for any resonant piezoelectric based sensor. The wireless interface can be improved by using highly directional antennas and the power can be increased. Multiple sensors can be simultaneously addressed so long as their resonant frequencies do not overlap. The separation distance limits demonstrated in this work are very practical for biological implants, for example as an implantable glucose sensor for diabetics, which would only need to pass a few millimeters of tissue to be used as a remote sensor.

7.3 High Q-factor Chip-scale Whispering Gallery Mode Magnetometer

A novel novel optomechanical magnetometer was demonstrated by taking advantage of the high Q-factor (>10^7) of the MEMS whispering gallery mode resonance realized by a chip-scale glassblowing process. The integration of a micromagnet on the top of a borofloat microbubble enabled magnetic force sensing without compromising the ultra high Q-factor. The perpendicular micromagnet orientation (relative to the sample plane) with the thinnest (1.1 μm) shell thickness microbubble yielded the highest sensitivity of 1.9 GHz/mT. A COMSOL model and experimental data determined that forces acting parallel to the sample plane have minimal radial deformation of the microbubble and have poor magnetic sensing capability compared to perpendicular applied force to the top the microbubble. The experimental limit of detection was determined to be 60 nT/$\sqrt{\text{Hz}}$ at 25 Hz, which was found to be limited by laser stability. The theoretical limit of detection for the device fabricated in this work is determined to be 98 pT.

Several avenues of improvements should be explored for this sensor. If the microbubble can be made more compliant without sacrificing the Q-factor the sensitivity can be improved. Replacing the borosilicate with fused silica can improve the Q-factor. Other work has shown that fused silica can be glassblown on a chip-scale using a similar process [176].

Appendix A

Thin Quartz Crystal Resonator Process Flow

1. Initial Clean
   (a) Start with 100 μm thick, 25 mm diameter AT-quartz
   (b) Dip the quartz into Piranha cleaning solution (4:1 H_2SO_4:H_2O_2 for 30 minutes. Note that Cyantek's Nanostrip at 70 °C can also be used.
   (c) Rinse in DI water (15 s)
   (d) N_2 dry
2. Mount on Dummy Glass
   (a) Apply drop of S1805 photoresist on glass and place 1 inch quartz wafer to spread the photoresist.
   (b) Bake 115 °C for 3 minutes.
3. Evaporate Cr/Au seed layer using Semicore evaporator
   (a) Deposit 20 nm Cr. Note: Avoid Ti as it sometimes does not stick well to Quartz.
   (b) Deposit 150 nm Au.
4. 1st Lithography: Quartz Etch Pattern
   (a) Bake 97 °C for 60 s to dehydrate.

(b) Spin HMDS at 4000 RPM for 40 s.

(c) Bake 97 °C for 60 s.

(d) Spin SPR 220-7 at 1000 RPM for 40 s. Expected thickness is 15 μm

(e) Bake 115 °C for 300 s.

(f) Multiple exposure: 15s exposure (at 8.0 mW/cm^2) for 6 cycles (720 mJ/cm^2), 15s wait time.

(g) Wait 30 minutes before developing

5. Develop in CD-26 for 12 minutes.

6. Nickel Electroplating

   - Current: 7 mA (20 ms on / 80 ms off)
   - Time: 11 Hours
   - Spinner Speed: 250 RPM
   - Expected Thickness: 15 μm
   - Rinse with DI water and N_2 Dry

7. Demount and strip Photoresist using MicroChem RemoverPG at 70 ^{o}C

8. Indium Mount on 100 mm Si Wafer. Heating gradually increase temperature to 180 °C. Note: Indium melts at 155 °C.

9. Quartz Etching Alcatel AMS 100

   - Gas Flow Rates Ar: 49 SCCM / SF_6: 7 SCCM
   - Source Power: 2000 W, Substrate Power: 400 W
   - Stagger the etching to prevent overheating: Etch for 5 min, cool 10 min.
   - Etch rate is $\sim$0.3 μm/min. Total etch time is 8-10 hours.
   - The individual dies are defined in this process by etching a large square causing the quartz to easily cleave along the etched edges.

10. Release Indium submount from 100 mm Si Wafer. Heating gradually increase temperature to 180 °C and remove the Quartz dies by sliding them off the melted Indium. Note: Indium melts at 155 °C.

11. Wet etch seed layer and Indium
    (a) Etch in Aqua Regia (HNO_3:HCl 1:3) until all metal is visually gone
    (b) Rinse in DI water (3 cycles)
    (c) N_2 dry
12. Evaporate Cr/Au Top Electrode layer using Semicore evaporator
    (a) Deposit 20 nm Cr. Note: Avoid Ti as it sometimes does not stick well to Quartz.
    (b) Deposit 150 nm Au.
13. Mount Quartz die on Dummy Glass
    (a) Apply small drop of S1805 photoresist on glass and place quartz die to spread the photoresist.
    (b) Bake 115 °C for 3 minutes.
14. 2^{nd} Lithography: Top Electrodes
    (a) Spray coat S1805 as evenly as possible using a handheld sprayer
    (b) Bake 115 °C for 60 s.
    (c) Typical thickness: 200 nm to 400 nm.
    (d) Exposure:
15. Develop CD-26 120 s
16. Etching Top Electrodes
    (a) Au Etch: Transene TFA, 30 s
    (b) Rinse in DI water (15 s)
    (c) Cr Etch: Transene 1020, 10 s
    (d) Rinse in DI water (3 cycles)
    (e) N_2 dry
17. Demount and strip photoresist

(a) Heat MicroChem RemoverPG to 70 °C

(b) Insert sample for 15 minutes

(c) Rinse with acetone (15 s)

(d) Rinse with IPA (15 s)

(e) Rinse with DI water (15 s)

(f) N_2 dry

18. Mount Quartz die on Dummy Glass, etched side down

    (a) Apply small drop of S1805 photoresist on glass and place quartz die to spread the photoresist.

    (b) Bake 115 °C for 3 minutes.

19. 3rd Lithography: Bottom Electrodes. Backside Alignment

    (a) Bake 97 °C for 60 s to dehydrate.

    (b) Spin HMDS at 4000 RPM for 40 s.

    (c) Bake 97 °C for 60 s.

    (d) Spin LOR 5A at 2000 RPM for 40 s.

    (e) Bake 170 °C for 180 s.

    (f) Spin S1805 at 4000 RPM for 40 s.

    (g) Bake 115 °C for 60 s.

    (h) Expose

20. Develop CD-26 60 s

21. Oxygen Descum PT720

    - O_2: 50 SCCM
    - Power: 75 W
    - Pressure: 10 mT
    - Time: 7 s

22. Evaporate Cr/Au seed layer using Semicore evaporator

(a) Deposit 20 nm Cr. Note: Avoid Ti as it sometimes does not stick well to Quartz.

(b) Deposit 150 nm Au.

23. Demount and strip photoresist

(a) Heat MicroChem RemoverPG to 70 °C

(b) Insert sample for 15 minutes

(c) Rinse with acetone (15 s)

(d) Rinse with IPA (15 s)

(e) Rinse with DI water (15 s)

(f) N_2 dry

24. Package

(a) Device is epoxied on one corner using EPOTEK H20E conductive epoxy. Epoxying all 4 corners creates stress in the sample and lowers the Q-factor

(b) Epoxy is cured at 150 °C for 5 min

(c) Chip package is Spectrum Semiconductor's CSB02491 24 pin DIP, with a hole cut via waterjet in the center.

(d) Al wire is wedge-bonded between the device electrodes and the package.

25. Metglas Deposition

(a) 25 μm thick Metglas 2605SA1 foils are cut into circles ~25 mm in diameter and epoxied to a target holder using EPOTEK H20E.

(b) The sample is placed between two neodymium magnets applying a magnetic field of ~50 mT perpendicular to the cantilever (to be defined in the next step by focused ion beam) of the device.

(c) Ti/Metglas/Ti/Au (20/500/20/20 nm) is sputtered using a custom built sputtering system on the backside of the QCR through the backside hole in the package. The thickness is monitored using a quartz crystal monitor.

(d) Pressure: 40 μTorr, Gun voltage: 5.2 kV, Gun current: 2.2 mA for all meterials.

26. Focused Ion Beam Cut

    - Dimensions: 500 x 500 x 19 μm
    - Beam Current: 60 nA
    - Dwell Time 1 μS
    - Cut Time 4 hrs

Appendix B

Whispering Gallery Mode Magnetometer Fabrication

1. Lithography: Gas Cavity
   (a) Start with a single side polished 400 μ thick 100 mm silicon wafer. Lightly doped with boron and a 1-10 Ω - cm resistivity (doping is not expected to be a factor in process, any doping is probably OK)
   (b) Bake 97 °C for 60 s to dehydrate.
   (c) Spin HMDS at 4000 RPM for 40 s.
   (d) Bake 97 °C for 60 s.
   (e) Spin SPR 220-7 at 4000 RPM for 40 s. Expected thickness is 7 μm
   (f) Bake 95 °C for 90 s.
   (g) Bake 115 °C for 45 s.
   (h) Bake 95 °C for 90 s.
   (i) Multiple exposure: 15 s exposure (at 8.0 mW/cm^2) for 6 cycles (720 mJ/cm^2), 15 s wait time.
   (j) Wait 30 minutes before developing
2. Develop CD-26 120 s
3. DRIE Gas Cavity: Acatel AMS 100, Etch 250 μm etch

(a) Pulse 1: SF_6 300 SCCM, 3.0 seconds, Source Power: 1500 W, Substrate Power 100 W, Throttle Position: 20.4

(b) Pulse 2: C_4F_8 300 SCCM, 1.5 seconds, Source Power: 1500 W, Substrate Power 100 W, Throttle Position: 43.8

(c) Pulse 3: O_2 100 SCCM, 1.0 seconds, Source Power: 1500 W, Substrate Power 120 W, Throttle Position: 10.4

(d) Etch rate: approximately 5.2 μm/min

(e) Etch for 48.1 minutes, and check thickness by profilometer

4. Wet Bench: Clean Silicon

(a) Particles on the silicon will prevent a high quality bond. It is critical to keep the silicon as clean as possible.

(b) RemoverPG 75 °C for 15 min

(c) DI rinse

(d) N_2 Dry

(e) Nanostrip 75 °C for 10 min

(f) Spin Rinse Dry

5. Anodic Bond: EVG 520

(a) Clean the bonding face of the wafer bonder with isopropyl alcohol.

(b) Precise alignment is not required, but excess hanging glass off the silicon may easily crack and the crack may propagate before bonding is complete.

(c) Carefully align a 100 μm thick Pyrex 7740 or Borofloat 33 100 mm wafer

(d) Do not pump down the chamber! Set purge on and the pressure to 1000 mBar

(e) Heat to 400 °C and wait for temperature to stabilize

(f) Apply 50 N of force on the wafers.

(g) Silicon side of the wafer is grounded and the glass side is biased negative.

(h) Apply -200 V to -600 V to the glass slide in -200 V steps. Hold the voltage at each step until the current stabilizes to a low constant value. Current will initially exponentially decay and settle at approximately 0.8 mA.

(i) Remove voltage and cool the tool to room temperature.

(j) **IMPORTANT: Remove the purge pressure and vent the tool.** Failure to do this will cause the lid to jump up when opening and may cause injury and/or damage to tool.

6. Wafer Dice Provectus 7100

   (a) Due to the limited size of the heater, the bonded wafer must be diced.

   (b) Use 0077-1045-010-QKP hubless blade for the bonded wafer

   (c) Dicing speed 2 mm/s

7. Glass Etch

   (a) Etch glass using 49% HF.

   (b) Etch rate 6.2 μm/min

   (c) Etch to 75 μm, 50 μm or 37.5 μm.

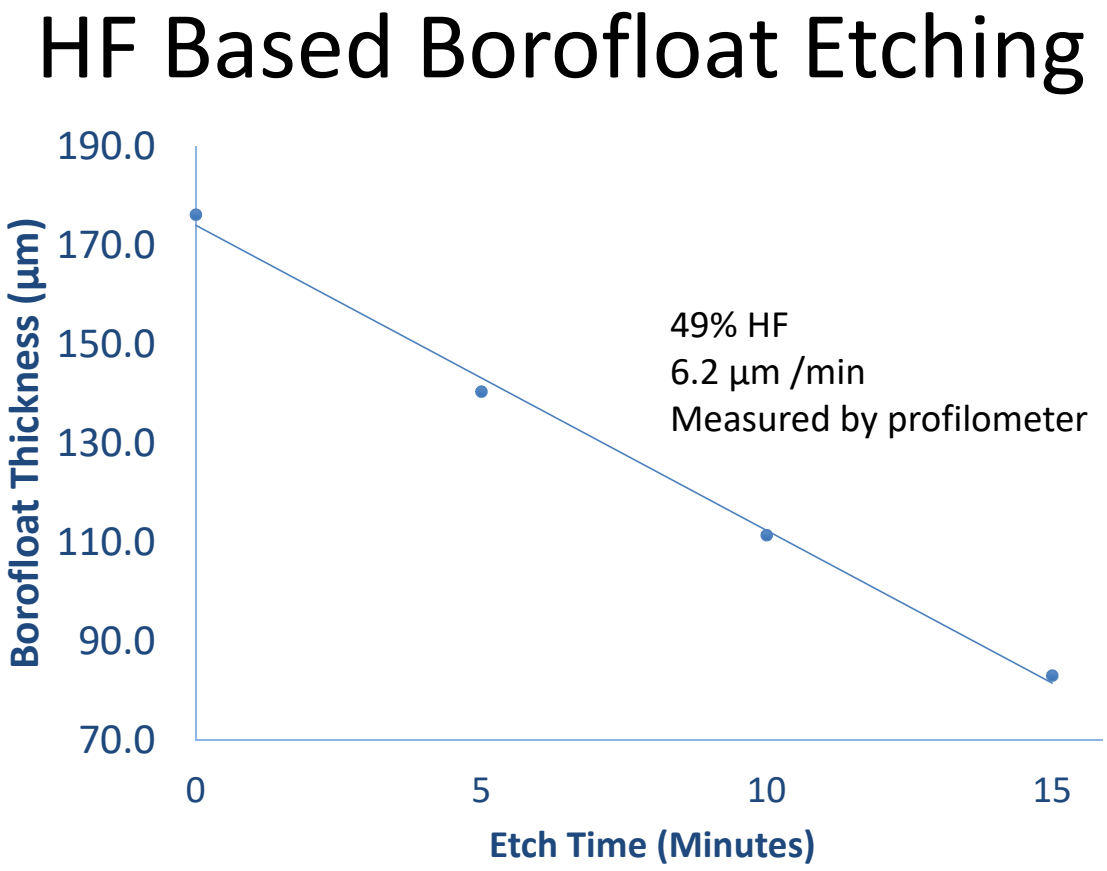

Figure B.1. Etch rate determined from etching a 175 µm thick borofloat 33 bonded to silicon with 49% HF and tracking the thickness by profilometer

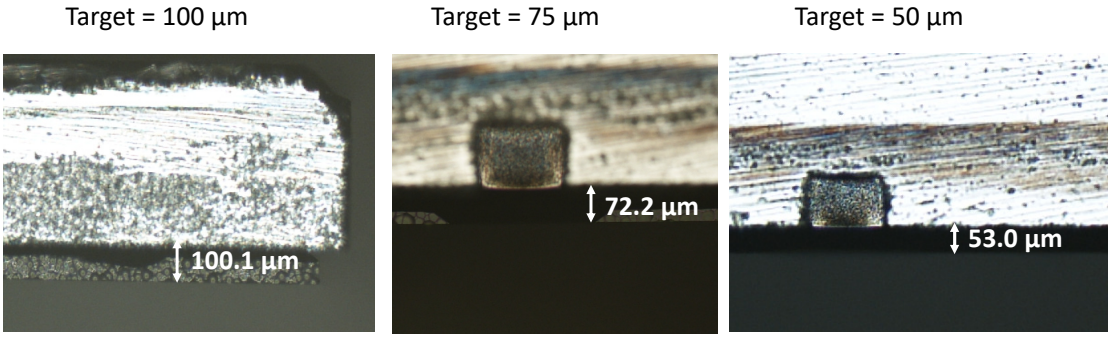

Figure B.2. Optical images of etch progression of 49% HF etching on borofloat 33. A 100 µm gas cavity is seen in some images. The etch is repeatable and controllable

8. Glassblowing

(a) Sample is placed inside of a VWR 1410 vacuum oven on a 55 mm x 23 mm x 4 mm 26 Ω silicon nitride ceramic heater purchased from Induceramic (Waterloo, Canada).

(b) Pump down chamber to -25 in Hg, or approximetly 100 Torr.

(c) Using a Volteq 3 KVA variac transformer 0-250 V, 110 V Input to control the heat.

(d) Set variac to 110 V and hold for 90 s.

(e) Increase variac to 130 V until the microbubble is "almost the desired size". This usually takes 30 seconds $\pm$ 5 s.

(f) Decrease variac to 110 V and hold for 60 s. Bubble will keep increasing in size for a few more seconds during this step.

(g) Decrease variac to 75 V and hold for 30 s.

(h) Decrease variac to 50 V and hold for 30 s.

(i) Decrease variac to 25 V and hold for 30 s.

(j) Decrease variac to 0 V.

(k) Wait 5 minutes for the sample to cool.

(l) Close the vacuum line and increase the pressure as slowly as possible (this usually takes approximately 2 minutes). Going too fast may thermally and mechanically shock the bubble causing it to shatter.

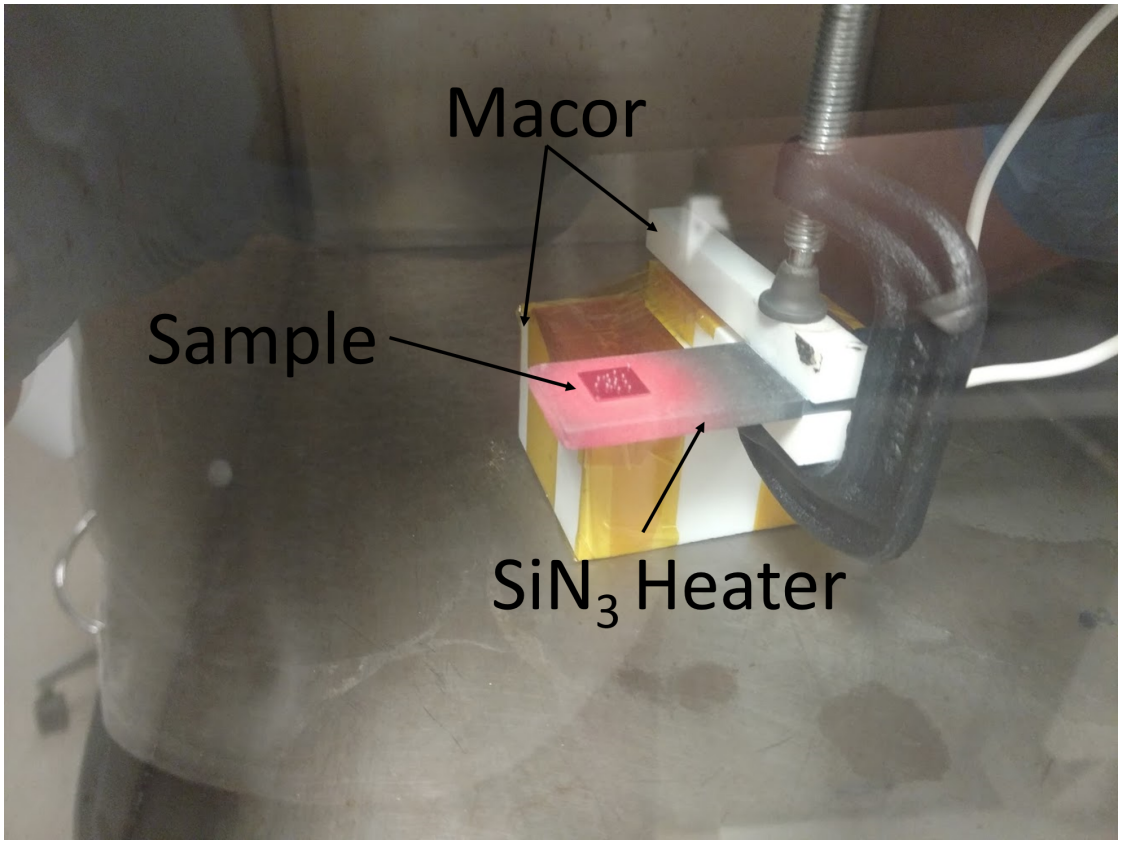

Figure B.3. Camera image of the microbubble being formed on the silicon nitride heater inside of the vacuum oven. Macor is used to thermally insulate the heater. A high temperature polyimide tape is used to hold some components together.

9. Micro-magneto Integration

   (a) Mix part A and part B of Devcon 5 minute epoxy (ITW Polymers Adhesives North America. Danvers, Massachusets, USA.

   (b) Apply the mixture using a needle to the surface of the N48 grade neodymium magnet, on the face that will be bonded to the microsphere.

   (c) Wait 3 minutes 30 seconds for the epoxy to become "tacky". This way, when it is placed on the microsphere it will not slide off.

   (d) Carefully place the magnet on the microsphere using a plastic tweezer and carefully adjust the magnet into it's optimal position.

   (e) Ensure that no epoxy goes near the equatorial plan of the microsphere, otherwise the whispering gallery mode resonance will be destroyed.

(f) Allow at least 1 hour for the epoxy to cure before testing.

Appendix C

Axial Magnetic force via the Filament Method

```
clc;
clear all;

uo=4*pi*10^(-7);%N/A^2

mag_rad = 0.75E-3;
mag_length = 1.5E-3;
mag_Br = 1.5;
Nm = 50;
mag_i=mag_Br*mag_length/(Nm*uo);

coil_rad = 12.5E-3;
coil_thick = 2E-3;
coil_length = 17E-3;
coil_outer =coil_rad+coil_thick;
coil_turns_r=2;
coil_turns_z=12;
coil_i = 2/0.628;

z = linspace (0,40E-3,30);
```

```
calcs = length(z)*coil_turns_r*coil_turns_z;
textprogressbar('calculating outputs: ');
for disp=1:length(z)
   Ff(disp)=0;
   textprogressbar(disp/length(z)*100);
      for nr=1:coil_turns_r
         for nz=1:coil_turns_z
             for i = 1:Nm
               L=-0.5*(coil_length+mag_length)+(nz-1)/
           (coil_turns_z-1)*coil_length+(i-1)/(Nm-1)*mag_length;
               r=coil_outer+(nr-1)/(coil_turns_r-1)*
           (coil_outer-coil_rad);
               m=4*r*mag_rad/((r+mag_rad)^2+(z(disp)+L)^2);
               [K,E]=ellipke(m);
               Ff(disp)=uo*coil_i*mag_i*(z(disp)+L)*
           sqrt(m/(4*r*mag_rad))*(K-((m/2)-1)/(m-1)*E)+Ff(disp);
             end;
          end;
     end;
end;
textprogressbar('terminated');
plot(z,Ff);
```

Bibliography

[1] SATO, S., M. BALISH, and R. MURATORE (1991) "Principles of magnetoencephalography," *Journal of Clinical Neurophysiology*, **8**(2), pp. 144–156.

[2] MILLER, J., M. BIRD, S. BOLE, A. BONITO-OLIVA, Y. EYSSA, W. KENNEY, T. PAINTER, H.-J. SCHNEIDER-MUNTAU, L. SUMMERS, S. VAN SCIVER, ET AL. (1994) "An overview of the 45-T hybrid magnet system for the new National High Magnetic Field Laboratory," *IEEE Transactions on Magnetics*, **30**(4), pp. 1563–1571.

[3] SHEAHEN, T. P. (2002) "Sensitive Applications," *Introduction to High-Temperature Superconductivity*, pp. 81–96.

[4] AWAD, H. L. and I. (1992) *Epilepsy surgery*, Raven Press, New York.

[5] KWONG, J. S., B. LEITHÄUSER, J.-W. PARK, and C.-M. YU (2013) "Diagnostic value of magnetocardiography in coronary artery disease and cardiac arrhythmias: A review of clinical data," *International Journal of Cardiology*, **167**(5), pp. 1835–1842.

[6] BAULE, G. and R. MCFEE (1963) "Detection of the magnetic field of the heart," *American Heart Journal*, **66**(1), pp. 95–96.

[7] TRISTAN TECHNOLOGIES, "Biomagnetism General," .
URL http://tristantech.com/biomagnetism-genera

[8] LENZ, J. and S. EDELSTEIN (2006) "Magnetic sensors and their applications," *IEEE Sensors Journal*, **6**(3), pp. 631–649.

[9] PRANCE, R., T. CLARK, and H. PRANCE (2000) "Ultra low noise induction magnetometer for variable temperature operation," *Sensors and Actuators A: Physical*, **85**(1-3), pp. 361–364.

[10] DRUNG, D., C. ASSMANN, J. BEYER, A. KIRSTE, M. PETERS, F. RUEDE, and T. SCHURIG (2007) "Highly sensitive and easy-to-use SQUID sensors," *IEEE Transactions on Applied Superconductivity*, **17**(2), pp. 699–704.

[11] JAKLEVIC, R. C., J. LAMBE, A. H. SILVER, and J. E. MERCEREAU (1964) "Quantum Interference Effects in Josephson Tunneling," *Physical Review Letters*, **12**(7), pp. 159–160.

[12] JOSEPHSON, B. (1962) "Possible new effects in superconductive tunnelling," *Physics Letters*, **1**(7), pp. 251–253.

[13] NAVE, C. *SQUID Magnetometer*.
URL http://hyperphysics.phy-astr.gsu.edu/hbase/Solids/Squid.html

[14] TUMANSKI, S. (2013) "Modern magnetic field sensors–a review," *Organ*, **10**, p. 13.

[15] MCGUIRE, T. and R. POTTER (1975) "Anisotropic magnetoresistance in ferromagnetic 3d alloys," *IEEE Transactions on Magnetics*, **11**(4), pp. 1018–1038.

[16] VAN ELST, H. (1959) "The anisotropy in the magneto-resistance of some nickel alloys," *Physica*, **25**(1-6), pp. 708–720.

[17] GONDO, Y. and Z. FUNATOGAWA (1952) "On the Temperature Dependency of Magneto-resistance Effect of Iron Single Crystal," *Journal of the Physical Society of Japan*, **7**(1), pp. 41–43.

[18] MCGUIRE, T. (1975) "Magnetoresistance anisotropy in ferromagnetic Ni-Co alloys at low temperatures," in *AIP Conference Proceedings*, vol. 24, AIP, pp. 435–436.

[19] KUIJK, K., W. VAN GESTEL, and F. GORTER (1975) "The barber pole, a linear magnetoresistive head," *IEEE Transactions on Magnetics*, **11**(5), pp. 1215–1217.

[20] HONEYWELL (2008) *1- and 2-Axis Magnetic Sensors HMC1001/1002/1021/1022*.

[21] BAIBICH, M. N., J. M. BROTO, A. FERT, F. N. VAN DAU, F. PETROFF, P. ETIENNE, G. CREUZET, A. FRIEDERICH, and J. CHAZELAS (1988) "Giant magnetoresistance of (001) Fe/(001) Cr magnetic superlattices," *Physical Review Letters*, **61**(21), p. 2472.

[22] BINASCH, G., P. GRÜNBERG, F. SAURENBACH, and W. ZINN (1989) "Enhanced magnetoresistance in layered magnetic structures with antiferromagnetic interlayer exchange," *Physical review B*, **39**(7), p. 4828.

[23] TSYMBAL, E. Y. and D. G. PETTIFOR (2001) "Perspectives of giant magnetoresistance," *Solid State Physics*, **56**, pp. 113–237.

[24] MOTT, N. F. (1964) "Electrons in transition metals," *Advances in Physics*, **13**(51), pp. 325–422.

[25] CHANG, L., M. WANG, L. LIU, S. LUO, and P. XIAO (2014) "A brief introduction to giant magnetoresistance," *arXiv preprint arXiv:1412.7691*.

[26] BUTLER, W., X.-G. ZHANG, T. SCHULTHESS, and J. MACLAREN (2001) "Spin-dependent tunneling conductance of Fe|MgO| Fe sandwiches," *Physical Review B*, **63**(5), p. 054416.

[27] MATHON, J. and A. UMERSKI (2001) "Theory of tunneling magnetoresistance of an epitaxial Fe/MgO/Fe (001) junction," *Physical Review B*, **63**(22), p. 220403.

[28] DJAYAPRAWIRA, D. D., K. TSUNEKAWA, M. NAGAI, H. MAEHARA, S. YAMAGATA, N. WATANABE, S. YUASA, Y. SUZUKI, and K. ANDO (2005) "230% room-temperature magnetoresistance in CoFeB/ MgO/ CoFeB magnetic tunnel junctions," *Applied Physics Letters*, **86**(9), p. 092502.

[29] YUASA, S., A. FUKUSHIMA, H. KUBOTA, Y. SUZUKI, and K. ANDO (2006) "Giant tunneling magnetoresistance up to 410% at room temperature in fully epitaxial Co/ Mg O/ Co magnetic tunnel junctions with bcc Co (001) electrodes," *Applied Physics Letters*, **89**(4), p. 042505.

[30] TONDRA, M., A. JANDER, C. NORDMAN, J. ANDERSON, Z. QIAN, and D. WANG (2003) *3-axis magnetometers using spin dependent tunneling: Reduced size and power*, *Tech. rep.*, NVE CORP EDEN PRAIRIE MN.

[31] ZHU, J.-G. J. and C. PARK (2006) "Magnetic tunnel junctions," *Materials Today*, **9**(11), pp. 36–45.

[32] LAKESHORE *Lake Shore 7500/9500 Series Hall System User's Manual, Appendix A, Hall Effect Measurements*, *Tech. rep.*

[33] MATHUR, P., N. KATARIA, S. JAIN, and V. SHARMA (1975) "Electron mobility in n-InSb from 77 to 300K," *Journal of Physics C: Solid State Physics*, **9**(4), p. L89.

[34] SZE, S. M. and K. K. NG (2006) *Physics of semiconductor devices*, John wiley & sons, appendix F.

[35] CRYOTRONICS, L. *Hall Probe Selection Guide*.
URL http://www.lakeshore.com/products/Hall-Probes/Pages/ProbeGuide.aspx

[36] JANOSEK, M. (2017) "Parallel fluxgate magnetometers," in *High Sensitivity Magnetometers*, Springer, pp. 41–61.

[37] RABEAU, J., P. REICHART, G. TAMANYAN, D. JAMIESON, S. PRAWER, F. JELEZKO, T. GAEBEL, I. POPA, M. DOMHAN, and J. WRACHTRUP (2006) "Implantation of labelled single nitrogen vacancy centers in diamond using N 15," *Applied Physics Letters*, **88**(2), p. 023113.

[38] ACOSTA, V., A. JARMOLA, E. BAUCH, and D. BUDKER (2010) "Optical properties of the nitrogen-vacancy singlet levels in diamond," *Physical Review B*, **82**(20), p. 201202.

[39] ROBLEDO, L., H. BERNIEN, T. VAN DER SAR, and R. HANSON (2011) "Spin dynamics in the optical cycle of single nitrogen-vacancy centres in diamond," *New Journal of Physics*, **13**(2), p. 025013.

[40] JENSEN, K., N. LEEFER, A. JARMOLA, Y. DUMEIGE, V. M. ACOSTA, P. KEHAYIAS, B. PATTON, and D. BUDKER (2014) "Cavity-enhanced room-temperature magnetometry using absorption by nitrogen-vacancy centers in diamond," *Physical Review Letters*, **112**(16), p. 160802.

[41] TETIENNE, J., L. RONDIN, P. SPINICELLI, M. CHIPAUX, T. DEBUISSCHERT, J. ROCH, and V. JACQUES (2012) "Magnetic-field-dependent photodynamics of single NV defects in diamond: an application to qualitative all-optical magnetic imaging," *New Journal of Physics*, **14**(10), p. 103033.

[42] DANG, H., A. MALOOF, and M. ROMALIS (2010) "Ultrahigh sensitivity magnetic field and magnetization measurements with an atomic magnetometer," *Applied Physics Letters*, **97**(15), p. 151110.

[43] FRANZEN, W. and A. EMSLIE (1957) "Atomic orientation by optical pumping," *Physical Review*, **108**(6), p. 1453.

[44] SELTZER, S. J. (2008) *Developments in alkali-metal atomic magnetometry*, Ph.D. thesis, Princeton University.

[45] KOMINIS, I., T. KORNACK, J. ALLRED, and M. ROMALLS (2003) "A subfemtotesla multichannel atomic magnetometer," *Nature*, **422**(6932), p. 596.

[46] ALLRED, J., R. LYMAN, T. KORNACK, and M. ROMALIS (2002) "High-sensitivity atomic magnetometer unaffected by spin-exchange relaxation," *Physical Review Letters*, **89**(13), p. 130801.

[47] ROMALIS, M. V. and H. B. DANG (2011) "Atomic magnetometers for materials characterization," *Materials today*, **14**(6), pp. 258–262.

[48] WANG, Y., D. GRAY, D. BERRY, J. GAO, M. LI, J. LI, and D. VIEHLAND (2011) "An extremely low equivalent magnetic noise magnetoelectric sensor," *Advanced Materials*, **23**(35), pp. 4111–4114.

[49] XI, H., X. QIAN, M.-C. LU, L. MEI, S. RUPPRECHT, Q. X. YANG, and Q. M. ZHANG (2016) "A room temperature ultrasensitive magnetoelectric susceptometer for quantitative tissue iron detection," *Scientific Reports*, **6**(1), p. 29740.

[50] FANG, Z. (2011) *Ultra Sensitive Magnetic Sensors Integrating the Giant Magnetoelectric Effect With Advanced Microelectronics*, Ph.D. thesis, The Pennsylvania State University.

[51] HATIPOGLU, G. and S. TADIGADAPA (2015) "Experimental studies in magnetically induced transverse force-frequency effect in thin quartz microresonators," *Journal of Applied Physics*, **118**(3), p. 034508.

[52] ——— (2015) "Micromachined magnetoflexoelastic resonator based magnetometer," *Applied Physics Letters*, **107**(19), p. 192406.

[53] LI, M., V. T. ROUF, M. J. THOMPSON, and D. A. HORSLEY (2012) "Three-axis Lorentz-force magnetic sensor for electronic compass applications," *Journal of Microelectromechanical Systems*, **21**(4), pp. 1002–1010.

[54] HERRERA-MAY, A., P. GARCÍA-RAMÍREZ, L. AGUILERA-CORTÉS, E. FIGUERAS, J. MARTINEZ-CASTILLO, E. MANJARREZ, A. SAUCEDA, L. GARCÍA-GONZÁLEZ, and R. JUÁREZ-AGUIRRE (2011) "Mechanical design and characterization of a resonant magnetic field microsensor with linear response and high resolution," *Sensors and Actuators A: Physical*, **165**(2), pp. 399 – 409.

[55] THOMPSON, M. J. and D. A. HORSLEY (2009) "Resonant MEMS magnetometer with capacitive read-out," in *Sensors, 2009 IEEE*, IEEE, pp. 992–995.

[56] ASTROV, D. N. (1960) "The magnetoelectric effect in antiferromagnetics," *Sov. Phys. - JETP*, **11**(3), p. 708.

[57] RADO, G. T. and V. J. FOLEN (1961) "Observation of the magnetically induced magnetoelectric effect and evidence for antiferromagnetic domains," *Physical Review Letters*, **7**(8), pp. 310–311.

[58] BOOMGAARD, J. V. D., A. M. J. G. VAN RUN, and J. VAN SUCHTELEN (1976) "Magnetoelectricity in piezoelectric-magnetostrictive composites," *Ferroelectrics*, **10**(1), pp. 295–298.

[59] VAN DEN BOOMGAARD, J., D. R. TERRELL, R. A. J. BORN, and H. F. J. I. GILLER (1974) "An in situ grown eutectic magnetoelectric composite material," *Journal of Materials Science*, **9**(10), pp. 1705–1709.

[60] VAN RUN, A. M. J. G., D. R. TERRELL, and J. H. SCHOLING (1974) "An in situ grown eutectic magnetoelectric composite material," *Journal of Materials Science*, **9**(10), pp. 1710–1714.

[61] RYU, J., A. V. CARAZO, K. UCHINO, and H.-E. KIM (2001) "Magnetoelectric properties in piezoelectric and magnetostrictive laminate composites," *Japanese Journal of Applied Physics*, **40**(8R), p. 4948.

[62] RYU, J., S. PRIYA, K. UCHINO, and H.-E. KIM (2002) "Magnetoelectric Effect in Composites of Magnetostrictive and Piezoelectric Materials," *Journal of Electroceramics*, **8**(2), pp. 107–119.

[63] HOLMES, H. R., A. DEROUIN, S. WRIGHT, T. M. RIEDEMANN, T. A. LOGRASSO, R. M. RAJACHAR, and K. GHEE ONG (2014) "Biodegradation and biocompatibility of mechanically active magnetoelastic materials," *Smart Materials and Structures*, **23**(9), p. 095036.

[64] TAN, E. L., B. D. PERELES, B. HORTON, R. SHAO, M. ZOUROB, and K. G. ONG (2008) "Implantable Biosensors for Real-time Strain and Pressure Monitoring," *Sensors*, **8**(10), pp. 6396–6406.

[65] WANG, L. and F. G. YUAN (2008) "Vibration energy harvesting by magnetostrictive material," *Smart Materials and Structures*, **17**(4), p. 045009.

[66] REIS, S., M. P. SILVA, N. CASTRO, V. CORREIA, J. G. ROCHA, P. MARTINS, A. LASHERAS, J. GUTIERREZ, and S. LANCEROS-MENDEZ (2016) "Electronic optimization for an energy harvesting system based on magnetoelectric Metglas/-poly(vinylidene fluoride)/Metglas composites," *Smart Materials and Structures*, **25**(8), p. 085028.

[67] GIBBS, M. R. J., P. T. SQUIRE, D. BRUGEL, S. C. HARDY, and J. WILLSON (1987) "Magnetostrictive response of metallic glasses," *Journal of Applied Physics*, **61**(8), p. 3784.

[68] LI, M., J. GAO, Y. WANG, D. GRAY, J. LI, and D. VIEHLAND (2012) "Enhancement in magnetic field sensitivity and reduction in equivalent magnetic noise by magnetoelectric laminate stacks," *Journal of Applied Physics*, **111**(10), pp. 10–13.

[69] WUN-FOGLE, M., H. T. SAVAGE, and M. L. SPANO (1989) "Enhancement of magnetostrictive effects for sensor applications," *Journal of Materials Engineering*, **11**(1), pp. 103–107.

[70] KOBELEV, N., Y. M. SOIFER, V. SHTEINBERG, and Y. B. LEVIN (1987) ""Giant" ΔE-Effect and Magnetomechanical Damping in Amorphous Ferromagnetic Ribbons," *Physica Status Solidi (a)*, **102**(2), pp. 773–780.

[71] BROUHA, M. and J. VAN DER BORST (1979) "The effect of annealing conditions on the magneto-mechanical properties of Fe-B-Si amorphous ribbons," *Journal of Applied Physics*, **50**(B11), p. 7594.

[72] BERRY, B. S. and W. C. PRITCHET (1975) "Magnetic annealing and directional ordering of an amorphous ferromagnetic alloy," *Physical Review Letters*, **34**(16), pp. 1022–1025.

[73] MEEKS, S. W. and J. C. HILL (1983) "Piezomagnetic and elastic properties of metallic glass alloys $Fe_{67}CO_{18}B_{14}Si_1$ and $Fe_{81}B_{13.5}Si_{3.5}C_2$," *Journal of Applied Physics*, **54**(11), pp. 6584–6593.

[74] LIVINGSTON, J. D. (1982) "Magnetomechanical properties of amorphous metals," *Physica Status Solidi A*, **70**(2), pp. 591–596.

[75] BUCHOLTZ, F., K. KOO, A. DANDRIDGE, and G. SIGEL (1986) "Easy axis distribution in transversely annealed Metglas 2605 S2," *Journal of Magnetism and Magnetic Materials*, **54-57**, pp. 1607–1608.

[76] CADOGAN, J. M., S. J. CAMPBELL, J. JING, C. P. FOLEY, P. KATER, and Y. W. MAI (2014) "Annealing embrittlement of $Fe_{78}Si_9B_{13}$ (METGLAS-2605S2)," *Hyperfine Interactions*, **226**(1-3), pp. 7–14.

[77] YANG, Y., J. GAO, Z. WANG, M. LI, J. F. LI, J. DAS, and D. VIEHLAND (2011) "Effect of heat treatment on the properties of Metglas foils, and laminated magnetoelectric composites made thereof," *Materials Research Bulletin*, **46**(2), pp. 266–270.

[78] METGLAS (2003) *Magnetic Alloy 2705M*, *Tech. rep.*, Metglas, Inc., Conway, South Carolina.

[79] COCHRANE, R., R. HARRIS, and M. PLISCHKE (1974) "Role of structure in amorphous magnetic materials: Dense random packing of hard spheres of two sizes," *Journal of Non-Crystalline Solids*, **15**(2), pp. 239–249.

[80] JOULE, J. (1847) "XVII. On the effects of magnetism upon the dimensions of iron and steel bars," *Philosophical Magazine*, **30**(199), pp. 76–87.

[81] CHOPRA, H. D. and M. WUTTIG (2015) "Non-Joulian magnetostriction," *Nature*, **521**(7552), pp. 340–343.

[82] DAPINO, M. J., F. T. CALKINS, A. B. FLATAU, and D. L. HALL (1996) "Measured Terfenol-D material properties under varied applied magnetic field levels," in *Proceedings of SPIE*, pp. 2717–66.

[83] METGLAS (2011) *Amorphous Alloys for Transformer Cores*, *Tech. rep.*, Metglas, Inc., Conway, South Carolina.

[84] CLARK, A. and D. CROWDER (1985) "High temperature magnetostriction of $TbFe_2$ and $Tb_{.27}Dy_{.73}Fe_2$," *IEEE Transactions on Magnetics*, **21**(5), pp. 1945–1947.

[85] KELLOGG, R. A. (2003) *Development and modeling of iron-gallium alloys*, Ph.D. thesis, Iowa State University.

[86] DONG, S., J. ZHAI, F. BAI, J.-F. LI, and D. VIEHLAND (2005) "Push-pull mode magnetostrictive/piezoelectric laminate composite with an enhanced magnetoelectric voltage coefficient," *Applied Physics Letters*, **87**(6), p. 062502.

[87] BOZORTH, R. M., E. F. TILDEN, and A. J. WILLIAMS (1955) "Anisotropy and magnetostricion of some ferrites," *Phys. Rev.*, **99**(6), pp. 1788–1798.

[88] BICHURIN, M., V. PETROV, and G. SRINIVASAN (2003) "Theory of low-frequency magnetoelectric coupling in magnetostrictive-piezoelectric bilayers," *Physical Review B*, **68**(5), p. 054402.

[89] BHATTACHARYA, B. (2005) "Terfenol and Galfenols : Smart Magnetostrictive Metals for Intelligent Transduction," *Dir. Mag. (Indian Inst. of Technol. Kanpur)*, **7**(2), pp. 35–40.

[90] DATTA, A., D. NATHASINGH, R. J. MARTIS, P. J. FLANDERS, and C. D. GRAHAM (1984) "Saturation and engineering magnetostriction of an iron-base amorphous alloy for power applications," *Journal of Applied Physics*, **55**(6), pp. 1784–1786.

[91] SCHEINFEIN, M. R., J. UNGURIS, M. H. KELLEY, D. T. PIERCE, and R. J. CELOTTA (1990) "Scanning electron microscopy with polarization analysis (SEMPA)," *Review of Scientific Instruments*, **61**(10), p. 2501.

[92] ZHU, Y. (ed.) (2005) *Modern Techniques for Characterizing Magnetic Materials*, Springer-Verlag, New York.

[93] APC International, Mackeyville, Pennsylvania (2017) *Physical and Piezoelectric Properties of APC Materials*, rev. 3.

[94] FREEMAN, E., J. HARPER, N. GOEL, S. J. SCHIFF, and S. TADIGADAPA (2016) "Optimization of Metglas 2605SA1 and PZT-5A magnetoelectric laminates for magnetic sensing applications," in *2016 IEEE SENSORS*, pp. 1–3.

[95] KRONMÜLLER, H., M. FÄHNLE, M. DOMANN, H. GRIMM, R. GRIMM, and B. GRÖGER (1979) "Magnetic properties of amorphous ferromagnetic alloys," *Journal of Magnetism and Magnetic Materials*, **13**(1-2), pp. 53–70.

[96] PANKHURST, Q. A., J. Z. JIANG, S. BETTERIDGE, M. R. J. GIBBS, and G. A. GEHRING (1995) "Moment Canting in Amorphous Fesib Ribbons in Applied Fields - Unpolarized Mossbauer-Effect Studies," *Journal of Physics-Condensed Matter*, **7**(49), pp. 9571–9593.

[97] XU, J. and M. ATZMON (1998) "Temperature dependence of deformation-assisted crystallization in amorphous $Fe_{78}B_{13}Si_9$," *Applied Physics Letters*, **73**(13), pp. 1805–1807.

[98] HUANG, B., R. PEREZ, P. CRAWFORD, S. NUTT, and E. LAVERNIA (1995) "Mechanical Crystallization of Metglas $Fe_{78}B_{13}Si_9$ by Cryogenic High Energy Ball Milling," *MRS Proceedings*, **400**, p. 227.

[99] D. DUSSAULT, A.V. NESTE, M.L. TRUDEAU, AND R. SCHULZ (1992) "The Influence of Oxygen on the Crystallization Process of Amorphous Powders by Mechanical Deformations," in *Properties of Emerging P/M Materials* (J.M. Capus and R.M. German, ed.), Metal Powder Industries Federation, Princeton,NJ, pp. 13–21.

[100] LI, F., R. MISRA, Z. FANG, Y. WU, P. SCHIFFER, Q. ZHANG, S. A. TADIGADAPA, and S. DATTA (2013) "Magnetoelectric flexural gate transistor with nanotesla sensitivity," *Journal of Microelectromechanical Systems*, **22**(1), pp. 71–79.

[101] PEPAKAYALA, V., J. STEIN, and Y. GIANCHANDANI (2015) "Resonant magnetoelastic microstructures for wireless actuation of liquid flow on 3D surfaces and use in glaucoma drainage implants," *Microsystems & Nanoengineering*, **1**, p. 15032.

[102] FU, L., K. ZHANG, S. LI, Y. WANG, T.-S. HUANG, A. ZHANG, and Z.-Y. CHENG (2010) "In situ real-time detection of E. coli in water using antibody-coated magnetostrictive microcantilever," *Sensors and Actuators B: Chemical*, **150**(1), pp. 220–225.

[103] DEVOE, D. and A. PISANO (1997) "Modeling and optimal design of piezoelectric cantilevermicroactuators," *Microelectromechanical Systems, Journal of*, **6**(3), pp. 266–270.

[104] THOMAS, A. and M. GIBBS (1992) "Anisotropy and magnetostriction in metallic glasses," *Journal of Magnetism and Magnetic Materials*, **103**(1-2), pp. 97–110.

[105] TSUYA, N., K. I. ARAI, Y. SHIRAGA, M. YAMADA, and T. MASUMOTO (1975) "Magnetostriction of amorphous $Fe_{0.80}P_{0.13}C0_{0.07}$ ribbon," *Physica Status Solidi (a)*, **31**(2), pp. 557–561.

[106] NARITA, K., J. YAMASAKI, and H. FUKUNAGA (1979) "Saturation magnetostriction and its annealing behavior of $Fe_{100-x}B_x$ and $Co_{100-x}B_x$ amorphous alloys," *Journal of Applied Physics*, **50**(B11), p. 7591.

[107] DONG, S., J. ZHAI, J. LI, and D. VIEHLAND (2006) "Near-ideal magnetoelectricity in high-permeability magnetostrictive/piezofiber laminates with a (2-1) connectivity," *Applied Physics Letters*, **89**(25), p. 252904.

[108] SHEN, Y., J. GAO, Y. WANG, P. FINKEL, J. LI, and D. VIEHLAND (2013) "Piezomagnetic strain-dependent non-linear magnetoelectric response enhancement by flux concentration effect," *Applied Physics Letters*, **102**(17), p. 172904.

[109] TSUYA, N., K. I. ARAI, K. OHMORI, and Y. SHIRAGA (1974) "Magnetostriction measurement by three terminal capacitance method," *Japanese Journal of Applied Physics*, **13**(11), pp. 1808–1810.

[110] FIEBIG, M. (2005) "Revival of the magnetoelectric effect," *Journal of Physics D: Applied Physics*, **38**(8), p. R123.

[111] LIU, G., C.-W. NAN, N. CAI, and Y. LIN (2004) "Dependence of giant magnetoelectric effect on interfacial bonding for multiferroic laminated composites of rare-earth-iron alloys and lead–zirconate–titanate," *Journal of Applied Physics*, **95**(5), pp. 2660–2664.

[112] FILIPPOV, D., T. GALICHYAN, and V. LALETIN (2014) "Influence of an interlayer bonding on the magnetoelectric effect in the layered magnetostrictive-piezoelectric structure," *Applied Physics A*, **116**(4), pp. 2167–2171.

[113] NAN, C.-W., G. LIU, and Y. LIN (2003) "Influence of interfacial bonding on giant magnetoelectric response of multiferroic laminated composites of Tb_{1-x} Dy_xFe_2 and $PbZr_x$ $Ti_{1-x}O_3$," *Applied Physics Letters*, **83**(21), pp. 4366–4368.

[114] BROWN, C., R. KELL, R. TAYLOR, and L. THOMAS (1962) "Piezoelectric materials, a review of progress," *IRE Transactions on component parts*, **9**(4), pp. 193–211.

[115] CURIE, J. and P. CURIE (1880) "Développement, par pression, de l'électricité polaire dans les cristaux hémièdres à faces inclinées," *Comptes rendus de l'Académie des Sciences*, **91**, pp. 294–5.

[116] LIPPMANN, M. (1881) "On the principle of the conservation of electricity," *Philosophical Magazine*, **12**(73), pp. 151–154.

[117] SHAOPING, L., W. CAO, R. E. NEWNHAM, and L. E. CROSS (1993) "Electromechanical nonlinearity of ferroelectric ceramics and related non-180° domain wall motions," *Ferroelectrics*, **139**(1), pp. 25–49.

[118] MULLEN, A. J. (1969) "Temperature variation of the piezoelectric constant of quartz," *Journal of Applied Physics*, **40**(4), pp. 1693–1696.

[119] LI, Z., Z. XI, Z. XU, and X. YAO (2002) "Dielectric/ferroelectric response and phase transition of PMN 0.32PT single crystal," *Journal of Materials Science Letters*, **21**(17), pp. 1325–1327.

[120] KOBOR, D., M. TINE, A. HAJJAJI, L. LEBRUN, S. PRUVOST, and D. GUYOMAR (2011) "Comparative characterization of rhombohedral and tetragonal PZN-PT single crystals," *AIP Advances*, **1**(2), p. 022133.

[121] YUHUAN, X. (1991) *Ferroelectric materials and their applications*, Amsterdam: North-Holland.

[122] ERTURK, A. and D. J. INMAN (2009) "Appendix E: Numerical Data for PZT-5A and PZT-5H Piezoceramics," *Piezoelectric Energy Harvesting*, pp. 373–374.

[123] NIX, E. and I. WARD (1986) "The measurement of the shear piezoelectric coefficients of polyvinylidene fluoride," *Ferroelectrics*, **67**(1), pp. 137–141.

[124] SCHEWE, H. (1982) "Piezoelectricity of uniaxially oriented polyvinylidene fluoride," in *1982 Ultrasonics symposium*, IEEE, pp. 519–524.

[125] ZHANG, R., W. JIANG, B. JIANG, and W. CAO (2002) "Elastic, Dielectric and Piezoelctric Coefficients of Domain Engineered 0.70 Pb $(Mg_{1/3}Nb_{2/3})$ O_3-0.30 $PbTiO_3$ Single Crystal," in *AIP conference proceedings*, vol. 626, AIP, pp. 188–197.

[126] ZHANG, R., B. JIANG, W. CAO, and A. AMIN (2002) "Complete set of material constants of 0.93 Pb $(Zn_{1/3}Nb_{2/3})$ O_3-0.07 $PbTiO_3$ domain engineered single crystal," *Journal of Materials Science Letters*, **21**(23), pp. 1877–1879.

[127] HARSHE, G., J. DOUGHERTY, and R. NEWNHAM (1993) "Theoretical modelling of multilayer magnetoelectric composites," *International Journal of Applied Electromagnetics in Materials*, **4**(2), pp. 145–145.

[128] BICHURIN, M., V. PETROV, and G. SRINIVASAN (2002) "Theory of low-frequency magnetoelectric effects in ferromagnetic-ferroelectric layered composites," *Journal of applied physics*, **92**(12), pp. 7681–7683.

[129] EPOXY TECHNOLOGY (2015) *EPO-TEK H20E Technical Data Sheet*, *Tech. rep.*

[130] SHEN, Y., J. GAO, Y. WANG, J. LI, and D. VIEHLAND (2014) "High non-linear magnetoelectric coefficient in Metglas/PMN-PT laminate composites under zero direct current magnetic bias," *Journal of Applied Physics*, **115**(9), p. 094102.

[131] NELSON, L., C. BOWEN, R. STEVENS, M. CAIN, and M. STEWART (2003) "Modeling and measurement of piezoelectric fibers and interdigitaded electrodes for the optimization of piezofibre composites," *Smart Structures and Materials 2003*, **5053**, pp. 556–567.

[132] PISANI, D. M. (2014) *Piezoceramic Sensors/Actuators with Interdigitated Electrode Patterns*, Ph.D. thesis, University of California, Los Angeles.

[133] WILKIE, W. K., D. J. INMAN, J. W. HIGH, and R. B. WILLIAMS (2004) *Recent developments in nasa piezocomposite actuator technology*, *Tech. rep.*

[134] DONG, S., J. ZHAI, N. WANG, F. BAI, J. LI, D. VIEHLAND, and T. A. LOGRASSO (2005) "Fe-Ga/Pb($Mg_{1/3}Nb_{2/3}$)O_3-$PbTiO_3$ magnetoelectric laminate composites," *Applied Physics Letters*, **87**(22), p. 222504.

[135] ZHAI, J., Z. XING, S. DONG, J. LI, and D. VIEHLAND (2006) "Detection of pico-Tesla magnetic fields using magneto-electric sensors at room temperature," *Applied Physics Letters*, **88**(6), p. 062510.

[136] NAN, C. W., M. I. BICHURIN, S. DONG, D. VIEHLAND, and G. SRINIVASAN (2008) "Multiferroic magnetoelectric composites: Historical perspective, status, and future directions," *Journal of Applied Physics*, **103**(3).

[137] PARK, C.-S., K.-H. CHO, M. A. ARAT, J. EVEY, and S. PRIYA (2010) "High magnetic field sensitivity in Pb(Zr,Ti)O_3]-Pb($Mg_{1/3}Nb_{2/3}$)O_3 single crystal/Terfenol-D/Metglas magnetoelectric laminate composites," *Journal of Applied Physics*, **107**(9), p. 094109.

[138] ZHUANG, X., M. L. C. SING, C. CORDIER, S. SAEZ, C. DOLABDJIAN, J. DAS, J. GAO, J. LI, and D. VIEHLAND (2011) "Analysis of noise in magnetoelectric thin-layer composites used as magnetic sensors," *IEEE Sensors Journal*, **11**(10), pp. 2183–2188.

[139] GAO, J., Z. WANG, Y. SHEN, M. LI, Y. WANG, P. FINKEL, J. LI, and D. VIEHLAND (2012) "Self-powered low noise magnetic sensor," *Materials Letters*, **82**, pp. 178–180.

[140] WANG, Y., P. FINKEL, J. LI, and D. VIEHLAND (2013) "Mechanical loss and magnetoelectric response in magnetostrictive/interdigitated-electrode/piezoelectric laminated resonators," *Journal of Applied Physics*, **113**(12), pp. 1–4.

[141] PISANI, M. B., K. REN, P. KAO, and S. TADIGADAPA (2011) "Application of Micromachined y -cut-quartz bulk acoustic wave resonator for infrared sensing," *Journal of Microelectromechanical Systems*, **20**(1), pp. 288–296.

[142] KAO, P., S. DOERNER, T. SCHNEIDER, D. ALLARA, P. HAUPTMANN, and S. TADIGADAPA (2009) "A micromachined quartz resonator array for biosensing applications," *J. Microelectromechanical Syst.*, **18**(3), pp. 522–530.

[143] O'SULLIVAN, C. and G. GUILBAULT (1999) "Commercial quartz crystal microbalances - theory and applications," *Biosensors and Bioelectronics*, **14**(8-9), pp. 663–670.

[144] ROSENBAUM, J. (1988) *Bulk Acoustic Wave Theory and Devices*, Artech House.

[145] THOMPSON, M., S. M. BALLANTYNE, L.-E. CHERAN, A. C. STEVENSON, and C. R. LOWE (2003) "Electromagnetic excitation of high frequency acoustic waves and detection in the liquid phase," *Analyst*, **128**(8), pp. 1048–1055.

[146] OGI, H., H. NAGA, Y. FUKUNISHI, M. HIRAO, and M. NISHIYAMA (2009) "170-MHz electrodeless quartz crystal microbalance biosensor: Capability and limitation of higher frequency measurement," *Anal. Chem.*, **81**(19), pp. 8068–8073.

[147] OGI, H., K. MOTOSHISA, T. MATSUMOTO, K. HATANAKA, and M. HIRAO (2006) "Isolated electrodeless high-frequency quartz crystal microbalance for immunosensors," *Anal. Chem.*, **78**(19), pp. 6903–6909.

[148] ZHOU, X., J. ZHANG, T. JIANG, X. WANG, and Z. ZHU (2007) "Humidity detection by nanostructured ZnO: A wireless quartz crystal microbalance investigation," *Sensors Actuators, A Phys.*, **135**(1), pp. 209–214.

[149] KING, W. H. (1964) "Piezoelectric Sorption Detector." *Analytical Chemistry*, **36**(9), pp. 1735–1739.

[150] VOLDMAN, J. (2007) "Lecture 8: Lumped-element Modeling with Equivalent Circuits," in *Design and Fabrication of Microelectromechanical Devices—MIT Course No. 6.777J / 2.372J*, MIT OpenCourseWare, Cambridge MA.

[151] VAN BEEK, J. T. M. and R. PUERS (2012) "A review of MEMS oscillators for frequency reference and timing applications," *Journal of Micromechanics and Microengineering*, **22**(1), p. 013001.

[152] BOTTOM, V. E. (1947) "Note on the anomalous thermal effect in quartz oscillator plates." *American Mineralogist*, **32**(9-10), pp. 590–591.

[153] FILLER, R. (1988) "The acceleration sensitivity of quartz crystal oscillators: a review," *IEEE Transactions on Ultrasonics, Ferroelectrics and Frequency Control*, **35**(3), pp. 297–305.

[154] CLAYTON, L. and E. EERNISSE (1998) "Quartz thickness-shear mode pressure sensor design for enhanced sensitivity," *IEEE Transactions on Ultrasonics, Ferroelectrics and Frequency Control*, **45**(5), pp. 1196–1203.

[155] EERNISSE, E., T. LUKASZEK, and A. BALLATO (1978) "Variational calculation of force-frequency constants of doubly rotated quartz resonators," *IEEE Transactions on Sonics and Ultrasonics*, **25**(3), pp. 132–137.

[156] LEE, P. C. Y., Y. S. WANG, and X. MARKENSCOFF (1976) "Nonlinear effects of initial bending on the vibrations of crystal plates," *Journal of Acoustical Society of America*, **59**(1), pp. 90–96.

[157] ZHEYAO WANG, YONGGUI DONG, HUIZHONG ZHU, and GUANPING FENG (2004) "Effect of transverse force on the performance of quartz resonator force sensors," *IEEE Transactions on Ultrasonics, Ferroelectrics and Frequency Control*, **51**(4), pp. 470–476.

[158] MARDIGUIAN, M., D. L. SWEENEY, and R. SWANBERG (1992) *Controlling radiated emissions by design*, Springer.

[159] WANG, C.-T., C.-Y. WANG, J.-H. YU, I.-T. KUO, C.-W. TSENG, H.-C. JAU, Y.-J. CHEN, and T.-H. LIN (2016) "Highly sensitive optical temperature sensor based on a SiN micro-ring resonator with liquid crystal cladding," *Optics Express*, **24**(2), p. 1002.

[160] HENZE, R., T. SEIFERT, J. WARD, and O. BENSON (2011) "Tuning whispering gallery modes using internal aerostatic pressure," *Optics Letters*, **36**(23), pp. 4536–4538.

[161] VOLLMER, F. and L. YANG (2012) "Review Label-free detection with high-Q microcavities: a review of biosensing mechanisms for integrated devices," *Nanophotonics*, **1**(3-4).

[162] CHEN, Y., Q. HAN, T. LIU, X. LAN, and H. XIAO (2013) "Optical fiber magnetic field sensor based on single-mode-multimode-single-mode structure and magnetic fluid," *Optics Letters*, **38**(20), p. 3999.

[163] ZU, P., C. C. CHAN, W. S. LEW, Y. JIN, Y. ZHANG, H. F. LIEW, L. H. CHEN, W. C. WONG, and X. DONG (2012) "Magneto-optical fiber sensor based on magnetic fluid," *Optics Letters*, **37**(3), p. 398.

[164] LUO, L., S. PU, J. TANG, X. ZENG, and M. LAHOUBI (2015) "Highly sensitive magnetic field sensor based on microfiber coupler with magnetic fluid," *Applied Physics Letters*, **106**(19), p. 193507.

[165] EL AMILI, A., M. C. M. M. SOUZA, F. VALLINI, N. C. FRATESCHI, and Y. FAINMAN (2016) "Magnetically controllable silicon microring with ferrofluid cladding," *Optics Letters*, **41**(23), p. 5576.

[166] FORSTNER, S., S. PRAMS, J. KNITTEL, E. D. VAN OOIJEN, J. D. SWAIM, G. I. HARRIS, A. SZORKOVSZKY, W. P. BOWEN, and H. RUBINSZTEIN-DUNLOP (2012) "Cavity Optomechanical Magnetometer," *Physical Review Letters*, **108**(12), p. 120801.

[167] RAYLEIGH, J. W. S. B. (1896) *The theory of sound*, vol. 2, Macmillan.

[168] ORAEVSKY, A. N. (2002) "Whispering-gallery waves," *Quantum Electronics*, **32**(5), pp. 377–400.

[169] SHIRI, A. and A. SHOULAIE (2009) "A new methodology for magnetic force calculations between planar spiral coils," *Progress In Electromagnetics Research*, **95**, pp. 39–57.

[170] ROBERTSON, W., B. CAZZOLATO, and A. ZANDER (2012) "Axial force between a thick coil and a cylindrical permanent magnet: optimizing the geometry of an electromagnetic actuator," *IEEE Transactions on Magnetics*, **48**(9), pp. 2479–2487.

[171] JANSSEN, J., J. PAULIDES, E. LOMONOVA, F. BÖLÖNI, A. TOUNZI, and F. PIRIOU (2009) "Analytical calculation of interaction force between orthogonally magnetized permanent magnets," *Sensor Letters*, **7**(3), pp. 442–445.

[172] EKLUND, E. J. and A. M. SHKEL (2007) "Glass blowing on a wafer level," *Journal of Microelectromechanical Systems*, **16**(2), pp. 232–239.

[173] PRIKHODKO, I. P., S. A. ZOTOV, A. A. TRUSOV, and A. M. SHKEL (2011) "Microscale glass-blown three-dimensional spherical shell resonators," *Journal of Microelectromechanical Systems*, **20**(3), pp. 691–701.

[174] Newport Corporation, Irvine, CA (2008) *Model 1936-R/2936-R Series Manual*, part No. 90039770 rev A.

[175] REERMANN, J., P. DURDAUT, S. SALZER, T. DEMMING, A. PIORRA, E. QUANDT, N. FREY, M. HÃŰFT, and G. SCHMIDT (2017) "Evaluation of Magnetoelectric Sensor Systems for Cardiological Applications," *Measurement*, pp. –.

[176] SENKAL, D., M. AHAMED, A. TRUSOV, and A. SHKEL (2013) "High temperature micro-glassblowing process demonstrated on fused quartz and ULE TSG," *Sensors and Actuators A: Physical*, **201**, pp. 525–531.

Vita

Eugene Freeman

Education

December 2013	Master of Science in Electrical Engineering The Pennsylvania State University, University Park, PA
May 2011	Bachelors of Science in Microelectronic Engineering Rochester Institute of Technology, Rochester, NY

Honors and Awards

University Graduate Fellowship
Watkins Fell Electrical Eng Scholarship
Luther B. and Patricia A. Brown Fellowship